THÈSE

En vue de l'obtention du

DOCTORAT DE L'UNIVERSITÉ DE TOULOUSE

Délivré par :
Institut National Polytechnique de Toulouse (INP Toulouse)

Discipline ou spécialité :

Signal, Image, Acoustique et Optimisation (SIAO)

Présentée et soutenue par :
Reza Shirvany

le : 30 octobre 2012

Titre :

Estimation of the Degree of Polarization in Polarimetric SAR Imagery: Principles and Applications

---

Ecole doctorale :
Mathématiques Informatique Télécommunications (MITT)

Unité de recherche :
Institut de Recherche en Informatique de Toulouse (IRIT)

Rapporteurs :

Prof. Gregoire Mercier, Telecom Bretagne
Prof. Yannick Berthoumieu, IMS Bordeaux

Directeur(s) de th¯se :

Prof. Jean-Yves Tourneret, INPT-ENSEEIHT, directeur de thèse
Prof. Marie Chabert, INPT-ENSEEIHT, co-directeur de thèse

Membres du jury :

Prof. Christine Fernandez-Maloigne, Université de Poitiers, présidente
Prof. Gregoire Mercier, Telecom Bretagne, rapporteur
Prof. Yannick Berthoumieu, IMS Bordeaux, rapporteur
Prof. Jean-Yves Tourneret, INPT-ENSEEIHT, directeur de thèse
Prof. Marie Chabert, INPT-ENSEEIHT, co-directeur de thèse

Institut National Polytechnique de Toulouse
University of Toulouse

ESTIMATION OF THE DEGREE OF POLARIZATION IN POLARIMETRIC SAR IMAGERY: PRINCIPLES & APPLICATIONS

REZA SHIRVANY

Dissertation submitted to the University of Toulouse
for the degree of
Doctor of Philosophy

Jury
Prof. Christine Fernandez-Maloigne; Université de Poitiers; *president*
Prof. Gregoire Mercier; Telecom Bretagne; *rapporteur*
Prof. Yannick Berthoumieu; IMS Bordeaux; *rapporteur*
Prof. Jean-Yves Tourneret; INPT-ENSEEIHT; *advisor*
Prof. Marie Chabert; INPT-ENSEEIHT; *co-advisor*

– 2012 –

{reza.shirvany@ieee.org}

To My Parents

ABSTRACT

Polarimetric Synthetic Aperture Radar (SAR) systems have become highly fruitful thanks to their wide area coverage and day and night all-weather capabilities. Several polarimetric SARs have been flown over the last few decades with a variety of polarimetric SAR imaging modes; traditional ones are linear single- and dual-pol modes. More sophisticated ones are full-pol modes. Other alternative modes, such as hybrid and compact dual-pol, have also been recently proposed for future SAR missions.

The discussion is vivid across the remote sensing society about both the utility of such alternative modes, and also the trade-off between dual and full polarimetry. This thesis contributes to that discussion by analyzing and comparing different polarimetric SAR modes in a variety of geoscience applications, with a particular focus on maritime monitoring and surveillance. For our comparisons, we make use of a fundamental, physically related discriminator called the Degree of Polarization (DoP). This scalar parameter has been recognized as one of the most important parameters characterizing a partially polarized electromagnetic wave. Based on a detailed statistical analysis of polarimetric SAR images, we propose efficient estimators of the DoP for both coherent and in-coherent SAR systems. We extend the DoP concept to different hybrid and compact SAR modes and compare the achieved performance with different full-pol methods.

We perform a detailed study of vessel detection and oil-spill recognition, based on linear and hybrid/compact dual-pol DoP, using recent data from the Deepwater Horizon oil-spill, acquired by the National Aeronautics and Space Administration (NASA)/Jet Propulsion Laboratory (JPL) Uninhabited Aerial Vehicle Synthetic Aperture Radar (UAVSAR). Extensive experiments are also performed over various terrain types, such as urban, vegetation, and ocean, using the data acquired by the Canadian RADARSAT-2 and the NASA/JPL Airborne SAR (AirSAR) system.

RÉSUMÉ

Les radars à synthèse d ouverture (RSO) polarimétriques sont devenus incontournables dans le domaine de la télédétection, grâce à leur zone de couverture étendue, ainsi que leur capacité à acquérir des données dans n importe quelles conditions atmosphériques de jour comme de nuit. Au cours des trois dernières décennies, plusieurs RSO polarimétriques ont été utilisés portant une variété de modes d imagerie, tels que la polarisation unique, la polarisation double et également des modes dits pleinement polarimétriques. Grâce aux recherches récentes, d autres modes alternatifs, tels que la polarisation hybride et compacte, ont été proposés pour les futures missions RSOs.

Toutefois, un débat anime la communauté de la télédétection quant à l utilité des modes alternatifs et quant au compromis entre la polarimétrie double et la polarimétrie totale. Cette thèse contribue à ce débat en analysant et comparant ces différents modes d imagerie RSO dans une variété d applications, avec un accent particulier sur la surveillance maritime (la détection des navires et de marées noires). Pour nos comparaisons, nous considérons un paramètre fondamental, appelé le degré de polarisation (DoP). Ce paramètre scalaire a été reconnu comme l un des paramètres les plus pertinents pour caractériser les ondes électromagnétiques partiellement polarisées. A l aide d une analyse statistique détaillée sur les images polarimétriques RSO, nous proposons des estimateurs efficaces du DoP pour les systèmes d imagerie cohérente et incohérente. Ainsi, nous étendons la notion de DoP aux différents modes d imagerie polarimétrique hybride et compacte. Cette étude comparative réalisée dans différents contextes d application dégage des propriétés permettant de guider le choix parmi les différents modes polarimétriques.

Les expériences sont effectuées sur les données polarimétriques provenant du satellite Canadian RADARSAT-2 et le RSO aéroporté Américain AirSAR, couvrant divers types de terrains tels que l urbain, la végétation et l océan. Par ailleurs nous réalisons une étude détaillée sur les potentiels du DoP pour la détection et la reconnaissance des marées noires basée sur les acquisitions récentes d UAVSAR, couvrant la catastrophe de Deepwater Horizon dans le golfe du Mexique.

ACKNOWLEDGMENTS

La reconnaissance est la mémoire du cœur.

Gratitude is the memory of the heart.

—Jean-Baptiste Massieu, 1743–1818

I would like to express my gratitude to the many people who supported and helped me during my Ph.D. studies, making this time a period I will always cherish.

My special thanks go to my advisor and co-adviser, Jean-Yves Tourneret and Marie Chabert, who provided me with an exciting working environment, many opportunities to develop new ideas, and liberty in research, discussion and expression. I would like to thank Florent Chatelain, Nicolas Dobigeon, and Michele Galletti for productive comments, emails, and discussions. Special thanks also to the members of the jury who accepted this task with enthusiasm.

I am, of course, indebted to professors, colleagues, and members of the University of Toulouse. I especially thank Corinne Mailhes, Marie-Laure Boucheret, Nathalie Thomas, Martial Coulon, Jérôme Severini, and the future doctors, Cécile Bazot and Sokchenda Sreng. I am also thankful to Majid Ahmadpanah, and Michel Doisy for their support and presence. A special thought goes to Henri Bauer with whom I shared the passion for photography and philosophized about life.

At this point, I would like to thank my lovely parents, family, and friends for their patience, support, and everlasting fun. This was very important to me. A special thought goes to Yazdan for his helpful advices. Thanks to those, mostly far away, yet very present; Stephen, Kian, Sophia, and Liesa.

I acknowledge the financial support of the French Ministry of Higher Education and Research, which made this work possible. I also acknowledge the following organizations; NASA/Jet Propulsion Laboratory (JPL), NASA/Goddard Space Flight Center (GSFC), Alaska Satellite Facility (ASF), National Oceanic and Atmospheric Administration (NOAA), European Space Agency (ESA), and MacDonald, Dettwiler and Associates Ltd. (MDA).

CONTENTS

LIST OF TABLES

ACRONYMS

AirSAR Airborne SAR

ALOS Advanced Land Observing Satellite

ASAR Advanced Synthetic Aperture Radar

ASF Alaska Satellite Facility

ASI Italian Space Agency

ATI Along-Track Interferometric

BGD Bivariate Gamma Distribution

BMBF German Ministry of Education and Science

BP British Petroleum

BSA Back Scattering Alignment

CL Circular-Linear

CP Compact Polarimetric

CPD Co-Polarized Phase Difference

CSA Canadian Space Agency

DARA German Space Agency

DCP Dual Circular Polarimetry

DLR German Aerospace Center

DoD Degree of Depolarization

DoP Degree of Polarization

EADS European Aeronautic Defense and Space Company

ENL Equivalent Number of Looks

EPA US Environmental Protection Agency

ESA European Space Agency

GRD Ground Range Multi-Look Detected

GSFC Goddard Space Flight Center

JAROS Japan Resources Observation System Organization

JAXA Japan Aerospace Exploration Agency

JPL Jet Propulsion Laboratory

MDA MacDonald, Dettwiler and Associates Ltd.

MGD Multivariate Gamma Distribution

ML Maximum Likelihood

MODIS Moderate-Resolution Imaging Spectroradiometer

MoM Method of Moments

MRI Magnetic Resonance Imaging

NASA National Aeronautics and Space Administration

NESZ Noise Equivalent Sigma Zero

NOAA National Oceanic and Atmospheric Administration

NRCS Normalized Radar Cross Section

OCT Optical Coherence Tomography

PALSAR Phased Array type L-band SAR

PDF Probability Density Function

PolSAR Polarimetric SAR

PS-OCT Polarization Sensitive Optical Coherence Tomography

RCM RADARSAT-2 Constellation Mission

SAR Synthetic Aperture Radar

SIR Space-borne Imaging Radar

UAVSAR Uninhabited Aerial Vehicle Synthetic Aperture Radar

XPD Cross-Polarized Phase Difference

XTI Cross-Track Interferometric

INTRODUCTION

. . . it appears that all light may characterized
as to its state of polarization.

— Norbert Wiener, 1930 [1]

POLARIMETRIC imagery is a well established tool providing important complementary information to traditional imaging systems in a variety of fields. Polarimetric imagery has been widely studied and employed in different applications such as astronomy [2], meteorological investigations [3, 4], wetland monitoring [5], estimation of forest parameters [6], oil spill detection [7], computer vision [8], and medicine [9].

Radar polarimetry has gained a wholly new importance in the last few years, notably with the advent of new space-borne Synthetic Aperture Radars (SARs) such as the Japanese ALOS-PALSAR, the Canadian RADARSAT-2, and the German TerraSAR-X satellite. Polarimetric SAR (PolSAR) systems have opened the doors to many innovative applications. There exists a variety of PolSAR imaging modes; traditional ones are linear single- and dual-pol modes. More sophisticated ones are full-polarimetric modes. For the last five decades, canonical horizontal (H) and vertical (V) polarizations have been standardly used in PolSAR transmission and reception units. It was only in recent years that non-canonical modes, such as hybrid and compact, were proposed for PolSAR. Although the concept of non-canonical polarizations have an extensive heritage in radar astronomy, Souyris et al. [10, 11] were the first to propose the Compact Polarimetric (CP) $\pi/4$ mode for Earth observation applications.

In $\pi/4$ mode, the transmit polarization is the superposition of H and V polarizations and the received returns are recorded in both H and V polarizations (45°H, 45°V). In another study, Stacy and Preiss [12] proposed the Dual Circular Polarimetry (DCP) mode based on a right (or left) circular polarization transmit, and right and left circular polarization receives ([RR, RL] or [LR, LL]). In a recent study, Raney [13] promoted a hybrid (circular linear) mode of operation (CL-pol), with a right (or left) circular polarization on transmission and two linear polarizations on reception ([RH, RV] or [LH, LV]).

Hybrid and compact dual-pol systems provide a wider swath width and greater area coverage compared to full-pol systems. This, of course, is at the expense of not measuring all the available polarimetric information from a scene. Although hybrid and compact modes have the potential to capture more information than the classical dual-pol SARs, they, by design, lack the complete characterization of target scattering and optimum extraction of parameters. Hence, a major axis of research in SAR polarimetry is the assessment of the relative performance of different operational modes. The discussion is vivid across the remote sensing society about both the utility of emerging hybrid/compact modes, and also the trade-off between dual and full polarimetry. The discussion is particularly active on two distinct levels; the applications, and the system design. This thesis contributes to that discussion by analyzing and comparing different PolSAR modes in a variety of geoscience applications, with a particular focus on maritime monitoring and surveillance.

The research conducted to assess the performance of compact/hybrid SAR polarimetry can be classified into two distinct approaches. The first aims at *pseudo*-reconstruction of the full polarimetric information from the compact/hybrid measurements, so that the existing full-pol algorithms can be (indirectly) applied to compact/hybrid data. The pseudo-reconstruction approach [10] is based on simplifying assumptions on the symmetry properties of geophysical media. As a result, this approach cannot cope with point scatterers. Souyris et al. [10] have shown that the pseudo full-pol data perform nearly as well as genuine full-pol data in crop classification. Through analysis of the emerging polarimetric modes Nord et al. [14] have recently proposed an improved version of the original pseudo-reconstruction algorithm. The efficiency of these pseudo-reconstruction algorithms in different geoscience applications is subject of active research. Cloude [15], for example, has recently shown that current pseudo-reconstruction algorithms are unable to sufficiently describe all combinations of surface and volume scatterings, even in the well posed reflection symmetry case. Other studies have addressed the comparison of different PolSAR modes from the frequency point of view. Freeman et al. [16] and Dubois-Fernandez et al. [17] have highlighted the advantages of circular transmission at lower frequency, mainly with concern to the Faraday rotation. They argued that the best choice for the transmit polarization in the presence of ionospheric effects (low frequency) is circular.

The second approach to assess the performance of compact/hybrid SAR polarimetry consists in exploiting directly the compact/hybrid polarimetric information, and developing adapted algorithms, instead of reconstructing the pseudo full-pol information. Promoting this line of thought, Raney [13] has considered the Stokes framework for the analysis of hybrid (CL-pol) data with an emphasis on the advantages

of hybrid architecture with regard to relative errors, crosstalk, and phase and amplitude calibration. In another study, Cloude [18] has proposed a dual-pol version of the entropy/alpha decomposition for directly analyzing the dual-pol SAR data. Our analysis in this thesis belongs to this line of research.

Interesting discussions have also been carried out by Touzi [19], Pottier [20], and Truong-Loï et al. [21], highlighting different system aspects of the compact, hybrid, and linear dual- and full-pol SAR modes. Thanks to all these investigations, today it is widely accepted that compact/hybrid polarimetry is not a substitute of full-polarimetry, but a beneficial approach compared to classical dual-pol modes in a number of applications (e. g., land, ocean, and ice). Indeed, a better identification of such applications, as well as further comparative study of ocean (oil-spill and vessel detection) and ice (sea ice, glaciers, etc.) monitoring have been actively requested [22]. This is of major importance considering that future SAR missions are designed to carry compact/hybrid dual-pol SAR systems on-board; some examples are the Canadian RCM [23], the American DESDynI [24], the Argentinian SAOCOM [25], the Japanese ALOS-2 [26], and the Indian RISAT-1.

The aim of this work is to investigate in detail the information content of the complex and intensity data provided by different hybrid/compact and linear dual-pol SAR modes. We study the statistical properties of dual-pol SAR data, and derive Maximum Likelihood (ML) and Method of Moments (MoM) estimators of the Degree of Polarization (DoP) in coherent and incoherent dual-pol SAR systems. This scalar parameter has been considered as the most important parameter characterizing a partially polarized electromagnetic wave. The estimation of the DoP can help to determine the nature of the objects that backscatter the wave. It also provides an effective tool for assessing the performance of emerging hybrid/compact dual-pol modes with regard to classical dual- and full-pol modes. Experiments are performed on both synthetic and real data, acquired by RADARSAT-2, AirSAR, and UAVSAR systems, covering various terrain types such as urban, vegetation, and ocean. Among different applications, we notably focus on the maritime monitoring (joint ship and oil-spill detection) using the Deepwater Horizon oil-spill PolSAR data. The outline of the present dissertation, along with a list of publications are provided in what follows.

CHAPTER REVIEW

Chapter 1. A brief overview of different airborne and space-borne polarimetric SAR systems is presented. We describe the basic theory of electromagnetic wave scattering and polarization characteristics. We also review some important physical and math-

ematical definitions and multivariate probability distributions used throughout this manuscript.

Chapter 2. There exists a variety of polarimetric SAR imaging modes. Classical ones are linear dual- and full-pol modes, emerging ones are hybrid and compact modes. These polarimetric SAR modes and their specifications are presented in this chapter. Establishing a comprehensive PolSAR database is an important first step, and a challenging process, for our analysis and comparison. In this chapter, we also introduce the data and study sites used throughout this dissertation. This database has been composed based on *publicly available* data from a variety of organizations, in particular, National Aeronautics and Space Administration (NASA)/Jet Propulsion Laboratory (JPL), Goddard Space Flight Center (GSFC), Alaska Satellite Facility (ASF), National Oceanic and Atmospheric Administration (NOAA), European Space Agency (ESA), and MacDonald, Dettwiler and Associates Ltd. (MDA).

Chapter 3. We study the statistical properties of PolSAR data and show that the joint distribution of the multi-look SAR intensity images, composed from the Stokes parameters, is a Multivariate Gamma Distribution (MGD). Based on the characteristics of the MGDs, we derive ML and MoM estimators of the DoP for coherent and incoherent dual-pol SAR systems. In order to assess the performance of the proposed estimators, we derive the corresponding Cramer-Rao bound and asymptotic variances. Based on the latter, we theoretically show the efficiency of the ML estimators, in contrast to MoM estimators, and conclude that the ML estimators are the optimal estimators of the DoP. Moreover, we study the statistical characteristics of linear, hybrid, and circular full-pol intensity images, and prove that their joint distribution is an MGD parametrized by the elements of the polarimetric covariance matrix. We also show that for particular cases of linear, hybrid, compact, and circular dual-pol SARs, these distribution reduce to Bivariate Gamma Distributions (BGDs).

Chapter 4. We discuss in detail the detection of ships, oil-rigs, and oil spills based on the DoP in coherent dual-pol SAR systems. We perform the assessment of the relative performance of different hybrid, compact and linear dual-pol SAR modes. Experiments are performed on RADARSAT-2 C-band polarimetric data, over San Francisco Bay, and L-band NASA/JPL UAVSAR data, covering the Deepwater Horizon oil spill in the Gulf of Mexico. We show that the DoP estimation provides valuable real-time information for ship detection and oil spill recognition, under different polarizations and incidence angles. Among different dual-pol modes, we show that hybrid/compact and (HH, VV)

dual-pol modes deliver better ship and oil-spill detection results compared to classical linear dual-pol modes, i. e., (HH, HV) and (VH,VV). Moreover, we compare the dual-pol oil-spill detection results with the recent full-pol results from NASA/JPL UAVSAR researchers [27], covering the Deepwater Horizon oil-spill in the Gulf of Mexico. We also compare dual-pol ship detection results with full-pol results reported in recent publications of Marino et al. [28, 29]. Our results show that the detection performance based on the estimation of the DoP in hybrid and compact dual-pol modes are closely comparable to the recent results achieved using genuine full-poll data.

Chapter 5. Incoherent dual-pol SAR systems (such as Sentinel-1, ENVISAT ASAR and Airborne SAR (AirSAR) CYCLOPS) can deliver only two intensity images from a scene. On the other hand, the estimation of the DoP using only two intensity images is a challenging task. In this chapter, we address this task and analyze the performance of both ML and MoM estimators using synthetic and real data sets, over various terrain types such as urban, vegetation, and ocean. Experiments are performed on RADARSAT-2 C-band polarimetric data, over San Francisco Bay and Vancouver, BC, as well as L-band NASA/JPL AirSAR data, over San Francisco Bay and Flevoland, The Netherlands. We discuss the theoretical and experimental results and show the efficiency of ML estimators. We also perform the assessment of the relative information captured by the intensity data from different hybrid, compact and linear dual-pol SAR modes. Our results suggest that classical dual-pol modes, i. e., (HH, HV) and (VH,VV), performed better than emerging hybrid and compact dual-pol modes in terms of the estimation of the DoP based on only two intensity images. We provide a detailed analysis and draw conclusions.

Conclusion. Final chapter summarizes the general findings of the present work, and outlines directions for further research, and potential applications outside the geoscience field.

PUBLICATIONS

International Journal Papers

1. R. Shirvany, M. Chabert, and J.-Y. Tourneret, "Estimation of the degree of polarization for hybrid/compact and linear dual-pol SAR intensity images: principles and applications," *IEEE Transactions on Geoscience and Remote Sensing, accepted for publication,* 2012.

2. R. Shirvany, M. Chabert, and J.-Y. Tourneret, "Ship and oil-spill detection using the degree of polarization in linear and hybrid/compact dual-pol SAR," *IEEE Journal of Selected Topics in Applied Earth Observations and Remote Sensing*, vol. 5, no. 3, pp. 885–892, June 2012.

International Conference Papers

1. R. Shirvany, M. Chabert, and J.-Y. Tourneret, "Comparison of ship detection performance based on the degree of polarization in hybrid/compact and linear dual-pol SAR imagery,"*in Proceedings of the 2011 IEEE International Geoscience and Remote Sensing Symposium (IGARSS 11),* Vancouver, BC, Canada, Jul. 2011, pp. 3550–3553.

2. R. Shirvany, M. Chabert, and J.-Y. Tourneret, "Estimation of the degree of polarization in compact polarimetry,"*in Proceedings of the 2010 IEEE International Geoscience and Remote Sensing Symposium (IGARSS 10),* Honolulu, Hawaii, USA, Jul. 2010, pp. 722–725.

3. R. Shirvany, M. Chabert, and J.-Y. Tourneret, "Estimation of the degree of polarization in dual-polarized SAR imagery," *in Proceedings of the 2010 IEEE International Conference on Image Processing (ICIP 10),* Hong Kong, Sep. 2010, pp. 1401–1404.

4. R. Shirvany, M. Chabert, F. Chatelain, and J.-Y. Tourneret, "Maximum likelihood estimation of the polarization degree from two multi-look intensity images," *in Proceedings of the Thirty-Fifth IEEE International Conference on Acoustics, Speech, and Signal Processing (ICASSP 10),* Dallas, Texas, USA, Mar. 2010, pp. 1198–1201.

1 OVERVIEW

It probably helps that my background
is in the sciences and I can speak
the scientists language.

—David Chalmers

Polarimetric SAR systems have opened the doors to many innovative and new applications. Several polarimetric SARs have been built and flown over the last few decades. The aim of this chapter is to present a brief background information on polarimetric SAR systems and the related basic concepts. Section 1.1 presents a selection of important airborne and space-borne SAR systems. The basics of polarized electromagnetic waves, and polarimetric radar scatterings are then discussed in § 1.2. Section 1.3 addresses the unavoidable natural phenomenon inherent in SAR images called the speckle. We finally review some important mathematical definitions and theoretical probability distributions used throughout this thesis in § 1.4.

1.1 AIRBORNE AND SPACE-BORNE POLARIMETRIC SAR SYSTEMS

Pioneers such as Sinclair, Kennaugh, and Huynen made significant contributions in early polarimetric radar imaging research in the 1940 s. Soon the value of polarimetry was demonstrated in a variety of applications through the early works of Ulaby, Fung (geophysical parameter estimation), Valenzuela, Plant, and Alpers (ocean wave remote sensing). The polarimetric radar imaging particularly gained a considerable importance in 1988, when the NASA/JPL built and flew the AirSAR platform, which had the unique capability to provide full-polarimetric data at three frequencies (P-, L-, C-bands) on a single pass. AirSAR was the primary full-pol SAR system for almost 20 years. A brief description of a selection of important airborne and space-borne SAR systems is provided in what follows.

1.1.1 *Airborne Polarimetric SARs*

AirSAR (NASA/JPL, 1988–2004): The Airborne SAR (AirSAR) was a high-resolution, side-looking, full-polarimetric, multi-frequency SAR system, capable of simultaneously imaging in P-(0.45 GHz), L-(1.26 GHz) and C-(5.31 GHz) bands. It could also collect two types of L- and C-band interferometric data: Cross-Track Interferometric (XTI) data, sensitive to topography, and Along-Track Interferometric (ATI) data, used to measure ocean surface currents. AirSAR was designed and built by NASA/JPL. It flew in 1988 for the first time, and in 2004 for its last mission, serving as a NASA radar technology testbed for demonstrating new radar technology. Detailed technical specifications can be found in [30, 31]. An enhancement of the standard AirSAR quick-look processor was the AirSAR CYCLOPS, designed to provide amplitude imagery over large range and azimuth swaths [32].

UAVSAR (NASA/JPL, 2007–present): The Uninhabited Aerial Vehicle Synthetic Aperture Radar (UAVSAR) is a reconfigurable, high-resolution, full-polarimetric L-band (1.26 GHz, 24 cm wavelength) airborne system, operational since 2009, with a range bandwidth of 80 MHz (2 m range resolution), and a range swath greater than 16 km. UAVSAR is designed and built by NASA/JPL, as a successor to AirSAR, with a transmitted power greater than 2 kW, and a noise equivalent better than -45 dB for most of the swath. Detailed technical specifications can be found in [33, 34].

1.1.2 *Space-Borne Polarimetric SARs*

SIR-C/X-SAR (NASA/DARA/ASI, 1994): The Space-borne Imaging Radar (SIR)-C/X-SAR was the first full-polarimetric space-borne SAR. It was a joint project of the NASA, the German Space Agency (DARA) and the Italian Space Agency (ASI). It flew twice aboard the NASA space shuttle in 1994. The SIR-C/X-SAR antenna structure consisted of three individual antennas, one operating at L-band (23.5 cm wavelength), one at C-band (5.8 cm wavelength) and the third at X-band (3 cm wavelength). The L- and C-band antennas were constructed from separate panels providing the first quad-pol image data from space. Detailed technical specifications can be found in [35, 36].

ENVISAT ASAR (ESA, 2002–2012): ENVISAT was the ESA s largest civilian Earth observation mission. It was launched in 2002 with 10 instruments aboard, capable of providing measurements of the atmosphere, ocean, land, and ice. One of the instruments was the Advanced Synthetic Aperture Radar (ASAR), operating at C-band (5.331 GHz), with sophisticated capabilities in terms of

coverage, range of incidence angles, polarization, and modes of operation. The ENVISAT ASAR was not a full-polarimetric instrument; in its alternating polarization mode, dual-pol data, i. e., HH-HV, VH-VV, or HH-VV, were provided with spatial resolution of approximately 30 m. Detailed technical specifications can be found in [37].

ALOS-PALSAR (JAXA/JAROS, 2006–present): The Advanced Land Observing Satellite (ALOS) is a Japanese Earth-observing satellite, launched in 2006, with three remote-sensing instruments. The Phased Array type L-band SAR (PALSAR) is its polarimetric instrument providing both full-pol data (with a resolution of 24–89 m) and dual-pol data (at a resolution of down to 14 m). The development of PALSAR was a joint project between the Japan Aerospace Exploration Agency (JAXA) and the Japan Resources Observation System Organization (JAROS). Detailed technical specifications can be found in [38].

RADARSAT-2 (CSA/MDA, 2007–present): RADARSAT-2 is a Canadian C-band (5.405 GHz) SAR satellite, and a major data source for commercial applications and remote sensing science, providing valuable information for different application areas, including coastal and marine surveillance, agriculture, forestry, oceanography, and ice monitoring. RADARSAT-2 is a unique collaboration between the government—the Canadian Space Agency (CSA), and the industry—MacDonald, Dettwiler and Associates Ltd. (MDA). It supports right- and left-look imaging, and provides both full-pol and dual-pol data. Detailed technical specifications can be found in [39, 40].

TerraSAR-X (BMBF/DLR/Astrium GmbH, 2007–present): TerraSAR-X is a German radar satellite realized in a public-private partnership between the German Ministry of Education and Science (BMBF), the German Aerospace Center (DLR), and the European Aeronautic Defense and Space Company (EADS) Astrium GmbH. The satellite design is based on technology and knowledge achieved from the successful SAR missions such as SIR-C/X-SAR. The SAR sensor at X-band operates in different operation modes and resolutions. Launched in 2007, TerraSAR-X provides single- and dual-pol data in operation modes. On an experimental basis, full-pol mode and along-track interferometry are also possible. Detailed technical specifications can be found in [41].

Sentinel-1 (ESA, 2013): Sentinel-1 is a future radar imaging satellite from ESA for land and ocean services. Its C-band single- and dual-pol SAR is the core element of the mission, operational in four different observation modes enabling Sentinel-1 to respond to a wide range of varying requirements. A launch date around 2013 is foreseen. Sentinel-1 will provide incoherent (intensity) data at high spatial resolution, large coverage, and reliable repetition rates. Detailed technical specifications can be found in [42].

RCM (CSA/MDA, 2016): The RADARSAT-2 Constellation Mission (RCM), expected in 2016, is a CSA/MDA multi-satellite follow up to the RADARSAT-2 program with the objective of ensuring C-band data continuity, enhanced operational use of SAR data and improved system reliability over the next decade. The RCM is being designed for three main uses: maritime surveillance (ice, wind, oil pollution and ship monitoring); disaster management (mitigation, warning, response and recovery); and ecosystem monitoring (forestry, agriculture, wetlands and coastal change monitoring). In addition to RADARSAT-2 polarimetric modes, RCM will provide new compact polarimetric data, achieved by a single transmit of circular polarization and simultaneous coherent linear receptions. Detailed technical specifications can be found in [23].

Now that we have overviewed a number of airborne and spaceborne polarimetric SAR systems, we address, in the next section, the basics of polarized electromagnetic waves and polarimetric radar scatterings; in particular, we introduce the definitions of the Jones vector, the polarimetric scattering and covariance matrices, the Stokes vector, and the Degree of Polarization (DoP).

1.2 POLARIZATION CHARACTERISTICS

Jones Vector: Considering a right-handed system $(\hat{u}_{\mathrm{H}}, \hat{u}_{\mathrm{V}}, \hat{u})$, an electromagnetic, monochromatic plane wave propagating along $\hat{u}$ is expressed as

$$\vec{E}(u,t) = \vec{E}e^{i(\omega t - \nu u)} \tag{1.1}$$

where ω is the angular frequency, ν is the wavenumber, $\vec{E} = E_{\mathrm{H}}\hat{u}_{\mathrm{H}} + E_{\mathrm{V}}\hat{u}_{\mathrm{V}}$ is a complex two dimensional vector, and $(\hat{u}_{\mathrm{H}}, \hat{u}_{\mathrm{V}})$ forms a basis with two orthogonal unit vectors. The polarization state of an electromagnetic wave is determined from the amplitudes of E_{H} and E_{V}, and the relative phase between them.

We note that, $\vec{E}$ represented in vector form, and denoted as $\boldsymbol{E} = (E_{\mathrm{H}}, E_{\mathrm{V}})^T$, is called the Jones vector [43].

Polarimetric Covariance Matrix: In order to deal with a partially polarized wave, either the covariance matrix of $\boldsymbol{E}$ or the Stokes vector can be used. The covariance matrix of $\boldsymbol{E}$ is defined as [1, 44]

$$\boldsymbol{\Gamma} = \mathsf{E}\left[\boldsymbol{E}\boldsymbol{E}^{\dagger}\right] \tag{1.2}$$

$$= \begin{pmatrix} \mathsf{E}\left[|E_{\mathrm{H}}|^2\right] & \mathsf{E}\left[E_{\mathrm{H}}{E_{\mathrm{V}}}^*\right] \\ \mathsf{E}\left[E_{\mathrm{V}}{E_{\mathrm{H}}}^*\right] & \mathsf{E}\left[|E_{\mathrm{V}}|^2\right] \end{pmatrix} \tag{1.3}$$

where $\mathsf{E}[\cdot]$ is the expectation operator, † the conjugate transpose, * the complex conjugate, and $|\cdot|$ denotes the magnitude of the complex field. The covariance matrix $\boldsymbol{\Gamma}$ is a non-negative Hermitian matrix whose diagonal terms are the intensity components (in the H and V directions), and the cross terms are complex correlations between the Jones components. Without loss of generality, the above covariance matrix can be parametrized by $\boldsymbol{a} = (a_1, a_2, a_3, a_4)^T$ as

$$\boldsymbol{\Gamma} = \mathsf{E}\left[\boldsymbol{E}\boldsymbol{E}^{\dagger}\right] \triangleq \begin{pmatrix} a_1 & a_3 + ia_4 \\ a_3 - ia_4 & a_2 \end{pmatrix}. \tag{1.4}$$

The covariance matrix has great statistical properties and is a convenient representation for polarimetric data in many applications. Multilook polarimetric SAR processing (see § 1.3) can be simply performed by averaging several independent 1-look covariance matrices. The multilook (empirical) covariance matrix, denoted as $\overline{\boldsymbol{\Gamma}}$, is given by

$$\overline{\boldsymbol{\Gamma}} = \left\langle \boldsymbol{E}\boldsymbol{E}^{\dagger} \right\rangle = \begin{pmatrix} \left\langle |E_{\mathrm{H}}|^2 \right\rangle & \left\langle E_{\mathrm{H}}{E_{\mathrm{V}}}^* \right\rangle \\ \left\langle E_{\mathrm{V}}{E_{\mathrm{H}}}^* \right\rangle & \left\langle |E_{\mathrm{V}}|^2 \right\rangle \end{pmatrix} \tag{1.5}$$

where $\langle \cdot \rangle$ denotes the ensemble averaging. The polarization state of an electromagnetic wave can also be completely described through the observable power terms of the Stokes vector.

Stokes Vector: In his remarkable paper of 1852, Stokes [45] introduced four measurable quantities, known as the Stokes parameters, for describing the properties of polarized light. Let us consider the Pauli group of matrices expressed as

$$\boldsymbol{\sigma}_0 = \begin{pmatrix} 1 & 0 \\ 0 & 1 \end{pmatrix} \boldsymbol{\sigma}_1 = \begin{pmatrix} 1 & 0 \\ 0 & -1 \end{pmatrix} \tag{1.6}$$

$$\boldsymbol{\sigma}_2 = \begin{pmatrix} 0 & 1 \\ 1 & 0 \end{pmatrix} \boldsymbol{\sigma}_3 = \begin{pmatrix} 0 & -i \\ i & 0 \end{pmatrix}. \tag{1.7}$$

Therefore, the multi-look covariance matrix $\overline{\mathbf{\Gamma}}$ can be decomposed as [46, 47]

$$\begin{aligned}\overline{\mathbf{\Gamma}} = \left\langle \boldsymbol{E}\boldsymbol{E}^{\dagger} \right\rangle &= \begin{pmatrix} \langle |E_{\mathrm{H}}|^2 \rangle & \langle E_{\mathrm{H}} {E_{\mathrm{V}}}^* \rangle \\ \langle E_{\mathrm{V}} {E_{\mathrm{H}}}^* \rangle & \langle |E_{\mathrm{V}}|^2 \rangle \end{pmatrix} \\ &= \frac{1}{2}\left(g_0\sigma_0 + g_1\sigma_1 + g_2\sigma_2 + g_3\sigma_3\right) \\ &= \frac{1}{2}\begin{pmatrix} g_0 + g_1 & g_2 - ig_3 \\ g_2 + ig_3 & g_0 - g_1 \end{pmatrix}\end{aligned} \tag{1.8}$$

where the parameters $\{g_0, g_1, g_2, g_3\}$ are called the Stokes parameters, and the vector

$$\mathbf{g} = \begin{pmatrix} g_0 \\ g_1 \\ g_2 \\ g_3 \end{pmatrix} = \begin{pmatrix} \left\langle |E_{\mathrm{H}}|^2 + |E_{\mathrm{V}}|^2 \right\rangle \\ \left\langle |E_{\mathrm{H}}|^2 - |E_{\mathrm{V}}|^2 \right\rangle \\ 2\Re\left\langle E_{\mathrm{H}} E_{\mathrm{V}}^* \right\rangle \\ -2\Im\left\langle E_{\mathrm{H}} E_{\mathrm{V}}^* \right\rangle \end{pmatrix} \tag{1.9}$$

is called the Stokes vector. In these expressions, E is the complex electric field received in the subscripted polarization, $\langle \cdot \rangle$ denotes ensemble averaging (multilooking in the SAR context), and $\Re$ and $\Im$ denote the real and imaginary part of the complex field respectively.

As it can be observed, the Jones vector and consequently the polarimetric covariance matrix are determined by two complex quantities which can only be obtained through the use of a coherent radar system (measuring both amplitude and phase). The availability of such coherent systems is relatively recent. In the past, only non-coherent systems, measuring the power terms of an incoming wave, were available. Consequently, it was necessary to characterize the polarization of a wave only by power measurements (real quantities) through the Stokes vector. Several useful quantitative measures follow from the Stokes formalism for SAR data. These measures include the DoP, the degree of linear polarization, the degree of circular polarization, circular polarization ratio, and linear polarization ratio.

Degree of Polarization: This scalar parameter has been considered as the most important parameter characterizing a partially polarized electromagnetic wave [44, 48]. The DoP in terms of the covariance matrix elements is expressed as [44]

$$\mathcal{P} = \left(1 - 4\frac{|\mathbf{\Gamma}|}{(\mathrm{tr}\mathbf{\Gamma})^2}\right)^{\frac{1}{2}} \tag{1.10}$$

$$= \left(1 - \frac{4\left[a_1 a_2 - (a_3^2 + a_4^2)\right]}{(a_1 + a_2)^2}\right)^{\frac{1}{2}} \tag{1.11}$$

where $|\mathbf{\Gamma}|$ and $\mathrm{tr}\mathbf{\Gamma}$ are the determinant and trace of $\mathbf{\Gamma}$ respectively. The wave is totally depolarized for $\mathcal{P} = 0$, totally polarized for $\mathcal{P} = 1$,

and partially polarized when $\mathcal{P} \in]0,1[$. Since (1.10) is invariant under unitary transformations (such as rotation), the DoP does not depend on the particular orthogonal pair of polarimetric channels chosen to measure the backscattered wave [49]. In other words, the DoP is invariant of the (receiver) polarization basis. Estimation of the DoP from expression (1.10) can be conducted by estimating the four parameters of the covariance matrix, i. e., a_i, $i = 1, \ldots, 4$.

The DoP is equivalently defined in terms of the Stokes parameters as

$$\mathcal{P} = \frac{\sqrt{g_1^2 + g_2^2 + g_3^2}}{g_0}. \tag{1.12}$$

Mathematically, on the Poincaré sphere, the DoP represents the distance of a normalized Stokes vector s last three components from the origin. The surface of the unit Poincaré sphere corresponds to $\mathcal{P} = 1$, and represents all totally polarized states [50].

Degree of Depolarization: Once polarized wave interacts with a random medium, the polarization state of the backscattered wave may change. Hence, depolarization is associated with a reduction in the polarization of incident states. The Degree of Depolarization (DoD) is defined as

$$\overline{\mathcal{P}} = 1 - \mathcal{P}\,. \tag{1.13}$$

A depolarizing interaction causes the totally polarized Stokes states on the surface of the Poincaré sphere to emerge with $\mathcal{P} < 1$ ($\overline{\mathcal{P}} > 0$). The sister parameters of the DoP and DoD are defined as follows.

Degree of Polarization Uniformity: Denoted as $\mathcal{P}_U$, it is defined as

$$\mathcal{P}_U = \left(g_1^2 + g_2^2 + g_3^2\right)^{\frac{1}{2}}. \tag{1.14}$$

Degree of Linear Polarization: Denoted as $\mathcal{P}_L$, it is defined as

$$\mathcal{P}_L = \frac{\left(g_1^2 + g_2^2\right)^{\frac{1}{2}}}{g_0}. \tag{1.15}$$

Degree of Circular Polarization: Denoted as $\mathcal{P}_C$, it is defined as

$$\mathcal{P}_C = \frac{g_3}{g_0}. \tag{1.16}$$

Circular Polarization Ratio: Denoted as μ_C, it is defined as

$$\mu_C = \frac{g_0 - g_3}{g_0 + g_3}. \tag{1.17}$$

Linear Polarization Ratio: Denoted as μ_L, it is defined as

$$\mu_L = \frac{g_0 - g_1}{g_0 + g_1} \tag{1.18}$$

Modi ed Stokes Vector: We consider a modified Stokes vector $\widetilde{\mathbf{g}}$ as

$$\widetilde{\mathbf{g}} = \begin{pmatrix} \widetilde{g}_0 \\ \widetilde{g}_1 \\ \widetilde{g}_2 \\ \widetilde{g}_3 \end{pmatrix} = \frac{1}{2} \begin{pmatrix} g_0 + g_1 \\ g_0 - g_1 \\ g_0 + g_2 \\ g_0 + g_3 \end{pmatrix}. \tag{1.19}$$

In this dissertation, we show that the modified Stokes vector $\widetilde{\mathbf{g}}$ is of great mathematical interest,[1] and employ it to derive simple estimators of the DoP (Chapter 3). Throughout this manuscript, we refer to the four elements of $\widetilde{\mathbf{g}}$ as *four intensity images*. We also consider that for each intensity image, q looks are taken.

Sinclair Matrix: Full polarimetric radar systems measure the complex-valued elements of the so-called Sinclair matrix [51] (also known as scattering matrix). The Sinclair matrix $\boldsymbol{S}$ relates the electric vector $\boldsymbol{E}^{r}$ of the received (or backscattered) field to the transmitted (or incident) illumination $\boldsymbol{E}^{t}$ by

$$\boldsymbol{E}^{r} = \boldsymbol{S}\boldsymbol{E}^{t} \qquad \boldsymbol{S} = \begin{pmatrix} S_{HH} & S_{HV} \\ S_{VH} & S_{VV} \end{pmatrix}. \tag{1.20}$$

Scattering Vector: In the bistatic scattering case, the scattering vector corresponding to the Sinclair matrix is defined as [52]

$$\boldsymbol{k}_{FP} = \begin{pmatrix} S_{HH} \\ S_{HV} \\ S_{VH} \\ S_{VV} \end{pmatrix}. \tag{1.21}$$

The related covariance matrix is expressed as

$$\begin{aligned} \boldsymbol{C}_{FP} &= \left\langle \boldsymbol{k}_{FP} \boldsymbol{k}_{FP}^{\dagger} \right\rangle \\ &= \left\langle \begin{pmatrix} |S_{HH}|^2 & S_{HH}S_{HV}^* & S_{HH}S_{VH}^* & S_{HH}S_{VV}^* \\ S_{HV}S_{HH}^* & |S_{HV}|^2 & S_{HV}S_{VH}^* & S_{HV}S_{VV}^* \\ S_{VH}S_{HH}^* & S_{VH}S_{HV}^* & |S_{VH}|^2 & S_{VH}S_{VV}^* \\ S_{VV}S_{HH}^* & S_{VV}S_{HV}^* & S_{VV}S_{VH}^* & |S_{VV}|^2 \end{pmatrix} \right\rangle. \end{aligned} \tag{1.22}$$

Pauli RGB: Pauli RGB images are commonly used for visual presentation of PolSAR data. A Pauli RGB image is created from a full-pol data set as

$$Red = |S_{HH} - S_{VV}| \tag{1.23}$$

$$Green = |S_{HV} + S_{VH}| \tag{1.24}$$

$$Blue = |S_{HH} + S_{VV}|. \tag{1.25}$$

[1] in addition to its physical relevance in optical polarimetric imagery, detailed in [50].

Scattering Reciprocity: In a monostatic* configuration, the reciprocity property holds for most targets. Under the scattering reciprocity, and in the backscatter alignment convention, we have $S_{HV} = S_{VH}$ [53–55]. Therefore, the corresponding scattering vector is expressed as

$$\boldsymbol{k}_{FP}^{sr} = \begin{pmatrix} S_{HH} \\ \sqrt{2}S_{HV} \\ S_{VV} \end{pmatrix} \tag{1.26}$$

*A monostatic radar uses a common antenna for both transmission and reception.

where the factor $\sqrt{2}$ ensures the total power invariance.

Barakat Full-Pol DoP: The Barakat DoP is one of the well-known generalizations of the DoP. For a full polarimetric SAR, and under the scattering reciprocity, the Barakat DoP $\mathcal{P}_3$, and DoD $\overline{\mathcal{P}}_3$ are expressed as

$$\mathcal{P}_3 = \left[1 - 27\frac{|\boldsymbol{\Gamma}_3|}{(\mathrm{tr}\boldsymbol{\Gamma}_3)^3}\right]^{\frac{1}{2}} \tag{1.27}$$

$$\overline{\mathcal{P}}_3 = 1 - \mathcal{P}_3 \tag{1.28}$$

where the subscript 3 indicates the three-dimensional formalism and $\boldsymbol{\Gamma}_3$ is the 3×3 covariance matrix.

Images observed by SAR systems are degraded by speckle noise due to coherent interference of waves reflected from many elementary scatterers. Next section provides a brief description of the speckle noise.

1.3 SPECKLE NOISE

Speckle is inherent in SAR images. It is a natural phenomenon which acts like a noise source, but unlike system noise, cannot be avoided. Speckle noise is a predominantly multiplicative noise which generates a grainy structure in the image and reduces the precision of the measurements [52, 56]. It is caused by coherent processing of backscattered signals from multiple distributed targets [57], and can cause difficulties for image interpretation [58, 59]. Speckle noise is refered to as the *fully developed speckle*, under the following conditions: a large number of scatterers is present in a resolution cell of a homogeneous medium; the range distance is much larger than many radar wavelengths; the surface is much rougher on the scale of the radar wavelength. The fully developed speckle is characterized by a Rayleigh distribution [60].

Speckle noise in SAR images can be reduced by multilook processing (non-coherent) or spatial filtering (post image-formation methods). While multi-look processing is usually done during data acquisition stage, speckle reduction by spatial filtering is performed on the image after it is acquired. Through multilook processing, a speckle-reduced image is obtained by averaging multiple independent measurements [61, 62]. The majority of SAR systems perform the multilook

processing on-board. The number of looks, i. e., the number of independent samples included in the average, plays an important role in this process.

Speckle filtering is also an important step for consistent estimation of scattering mechanisms of distributed targets. However, such filtering can potentially eliminate actual image information as well; in particular the high-frequency information. Among the widely used (adaptive and non-adaptive) filters are Median, Gamma, Lee [63], refined Lee [64], Kuan [65], and Frost [66] filters. Detailed description of the PolSAR speckle filtering principles are provided in [52, 67] and references therein.

For PolSAR data, the statistical characteristic of the covariance matrix is well described by the complex Wishart distribution, based on which the probability density functions of relative phase and intensities can be derived. In what follows we focus on some important probability distributions (Gaussian, Wishart, Gamma) used throughout this manuscript.

1.4 THEORETICAL PROBABILITY DISTRIBUTIONS

1.4.1 *Multivariate Complex Gaussian Distribution*

A p-variate *complex Gaussian random variable* $\boldsymbol{\xi} = \left(Z_1, \ldots, Z_p\right)^T$, $Z_j = X_j + iY_j$, is a p-tuple of complex Gaussian random variables such that the vector of real and imaginary parts $\left(X_1, Y_1, \ldots, X_p, Y_p\right)^T$ has a $2p$-variate Gaussian distribution. When the Gaussian random variables X_j and Y_j are assumed to have zero mean, the distribution of $\boldsymbol{\xi}$ is fully specified by its $p \times p$ Hermitian positive definite complex covariance matrix $\boldsymbol{\Sigma}_{\boldsymbol{\xi}}$. The Probability Density Function (PDF) of a zero mean p-variate complex Gaussian distribution is given by [68]

$$p_{\mathrm{G}}\left(\boldsymbol{\xi}\right) = \frac{1}{\pi^p \left|\boldsymbol{\Sigma}_{\boldsymbol{\xi}}\right|} \exp\left(-\boldsymbol{\xi}^{\dagger} \boldsymbol{\Sigma}_{\boldsymbol{\xi}}^{-1} \boldsymbol{\xi}\right) \tag{1.29}$$

where $\boldsymbol{\Sigma}_{\boldsymbol{\xi}}$ is the covariance matrix and $|\cdot|$ represents the determinant. If $\boldsymbol{\xi}_1, \boldsymbol{\xi}_2, \ldots, \boldsymbol{\xi}_q$ is a sample of q independent complex-valued vectors from such a distribution, then the sample Hermitian covariance matrix

$$\hat{\boldsymbol{\Sigma}}_{\boldsymbol{\xi}} = \frac{1}{q} \sum_{j=1}^{q} \boldsymbol{\xi}_j \boldsymbol{\xi}_j^{\dagger} \tag{1.30}$$

is the maximum likelihood estimator of $\boldsymbol{\Sigma}_{\boldsymbol{\xi}}$. The estimator $\hat{\boldsymbol{\Sigma}}_{\boldsymbol{\xi}}$ is a sufficient statistic for the Hermitian covariance matrix $\boldsymbol{\Sigma}_{\boldsymbol{\xi}}$ [68].

1.4.2 *Multivariate Complex Wishart Distribution*

Let us consider $\boldsymbol{\xi}$ as a zero-mean p-variate complex Gaussian random vector. The joint distribution of the elements of the matrix

$\boldsymbol{A}_\xi = q\hat{\boldsymbol{\Sigma}}_\xi$ is called a *complex Wishart distribution* whose PDF is expressed as [68, th. 5.1]

$$p_{\mathrm{W}}\left(\boldsymbol{A}_\xi\right) = \frac{\left|\boldsymbol{A}_\xi\right|^{q-p}}{B\left(\boldsymbol{\Sigma}_\xi\right)} \exp\left[-\mathrm{tr}\left(\boldsymbol{\Sigma}_\xi^{-1}\boldsymbol{A}_\xi\right)\right] \tag{1.31}$$

where $B\left(\boldsymbol{\Sigma}_\xi\right) = \pi^{\frac{1}{2}p(p-1)}\Gamma\left(q\right)\cdots\Gamma\left(q-p+1\right)\left|\boldsymbol{\Sigma}_\xi\right|^q$. The Laplace transform of such a distribution is expressed as

$$\begin{aligned} L_{\boldsymbol{A}_\xi}(\boldsymbol{\Theta}) &= \mathsf{E}\left\{\exp\left[-\mathrm{tr}\left(\boldsymbol{\Theta}^T\boldsymbol{A}_\xi\right)\right]\right\} \\ &= \left|\mathbb{I}_p + \boldsymbol{\Sigma}_\xi\boldsymbol{\Theta}\right|^{-q} \end{aligned} \tag{1.32}$$

where $|\cdot|$ represents the determinant, $\mathbb{I}_p$ is a $p \times p$ identity matrix, and $\boldsymbol{\Theta}$ is a $p \times p$ complex Hermitian matrix such that $L_{\boldsymbol{A}_\xi}(\boldsymbol{\Theta}) < \infty$.

1.4.3 *Multivariate Gamma Distribution*

Multivariate Gamma Distribution (MGD) has several non-equivalent definitions in the literature. Here, we consider the definitions provided by Bernardoff [69]. Let $d \in \mathbb{N}$, the probability distribution $\boldsymbol{\mu}$ on $\mathbb{R}_+^d$, denoted by $\mathrm{Ga}(q, P)$, is an MGD defined by its Laplace transform as [69]

$$L_{\boldsymbol{\mu}}(\boldsymbol{z}) = \left[P(\boldsymbol{z})\right]^{-q} \tag{1.33}$$

where d is the dimension of the Gamma distribution, the shape parameter is $q > 0$, and the scale parameter $P(\boldsymbol{z})$ is an affine polynomial (i. e., $\forall j : \partial^2 P/\partial z_j^2 = 0$) with a constant term equal to 1. However, not all affine polynomials give rise to a valid Laplace transform, and thus, we focus on a particular case of MGD with a quadratic affine polynomial

$$P(\boldsymbol{z}) = 1 + \sum_{i=1}^{d} p_i z_i + \sum_{1\le i<j\le d} p_{ij} z_i z_j. \tag{1.34}$$

This family of polynomials, and the necessary and sufficient conditions under which they give rise to a valid PDF, have been thoroughly studied in the publications of Bernardoff [69], and Letac and Wesolowski [70]. In particular case of $d = 2$, a BGD is obtained with $P(\boldsymbol{z}) = 1 + p_1 z_1 + p_2 z_2 + p_{12} z_1 z_2$ where $p_1, p_2 > 0$ and $0 < p_{12} \le p_1 p_2$. The PDF of a random vector $\boldsymbol{x} = (x_1, x_2)^T$ following such a BGD is given by [71]

$$p_{\mathrm{BGD}}(\boldsymbol{x}) = \exp\left(-\frac{p_2 x_1 + p_1 x_2}{p_{12}}\right) \frac{x_1^{q-1} x_2^{q-1}}{p_{12}^q \Gamma(q)} f_q\left(c x_1 x_2\right) \mathbb{I}_{\mathbb{R}_+^2}\left(\boldsymbol{x}\right) \tag{1.35}$$

where $c = \left(p_1 p_2 - p_{12}\right)/p_{12}^2$, $\mathbb{I}_{\mathbb{R}_+^2}\left(\boldsymbol{x}\right)$ is the indicator function on $\mathbb{R}^+ \times \mathbb{R}^+$, and $f_q(z) = \sum_{j=0}^{\infty} z^j/\Gamma(q+j)j!$ is related to confluent hypergeometric, and modified Bessel functions [72, p. 374]. The moments

of a BGD can be obtained by using the Taylor series expansion of the given Laplace transform. Hence, the mean m_i, variance σ_i^2, $i = 1, 2$, covariance $\mathrm{Cov}(x_1, x_2)$, and correlation coefficient $\mathrm{Cor}(x_1, x_2)$ are expressed as

$$m_i = \mathsf{E}[x_i] = qp_i \tag{1.36}$$

$$\sigma_i^2 = \mathsf{E}\left[(x_i - m_i)^2\right] = qp_i^2 \tag{1.37}$$

$$\mathrm{Cov}(x_1, x_2) = \mathsf{E}[x_1 x_2] - \mathsf{E}[x_1]\,\mathsf{E}[x_2] = q(p_1 p_2 - p_{12}) \tag{1.38}$$

$$\mathrm{Cor}(x_1, x_2) = \frac{\mathrm{Cov}(x_1, x_2)}{\sigma_1 \sigma_2} = \frac{p_1 p_2 - p_{12}}{p_1 p_2}. \tag{1.39}$$

More generally, the moments of a BGD for any $(m, n) \in \mathbb{N}^2$ are given by

$$\mathsf{E}[x_1^m x_2^n] = m_1^m m_2^n \frac{(q)_m}{q^m} \frac{(q)_n}{q^n} \sum_{k=0}^{\min(m,n)} \frac{(-m)_k (-n)_k}{(q)_k} \frac{\rho^k}{k!} \tag{1.40}$$

where ρ is the correlation coefficient and $(a)_l$ is the Pochhammer symbol defined as [72, p. 256]

$$(a)_0 = 1 \tag{1.41}$$

$$(a)_{l+1} = (a + l)(a)_l, \qquad \forall l \in \mathbb{N}. \tag{1.42}$$

Different SAR imaging modes have been proposed and designed in recent years. Next Chapter introduces the classical and emerging polarimetric SAR imaging modes.

2

POLARIMETRIC SAR IMAGING MODES & STUDY SITES

The bottle neck of the downloading data rate generally advocates in favor of resolution rather than polarimetry.

— J.-C. Souyris et al, 2005 [10]

Linear polarization has been the unquestioned norm ... for more than ve decades.

— R.K. Raney and A. Freeman, 2009 [73]

There exists a variety of polarimetric SAR imaging modes; traditional ones are linear single- and dual-pol modes. More sophisticated ones are (linear/hybrid) full-polarimetric modes. Other alternative modes, such as hybrid and compact dual-pol, are also recently proposed for future SAR missions. The discussion is vivid across the whole remote sensing society about both the utility of such alternative modes, and also the trade-off between dual and full polarimetry. The discussion is particularly active on two distinct levels; the applications, and the system design. This thesis contributes to that discussion by analyzing and comparing different modes of operation in a variety of applications. To that end, we first briefly present these polarimetric SAR modes in § 2.1 and § 2.2. On the other hand, establishing a comprehensive PolSAR database is an important first step, and a challenging process, for our analysis and comparison. In § 2.3, we introduce the data and study sites used throughout this thesis. This database has been composed based on *publicly available* data from a variety of organizations, in particular, NASA/JPL, NASA/GSFC, ASF, NOAA, ESA, and MDA.

2.1 CLASSICAL IMAGING MODES

For the last five decades, horizontal (H) and vertical (V) polarizations have been used in both transmission and reception units, yielding a scattering matrix in the canonical H and V basis. These polarizations have formed the classical polarimetric modes, i. e., single-pol, linear dual-pol, and full-pol modes.

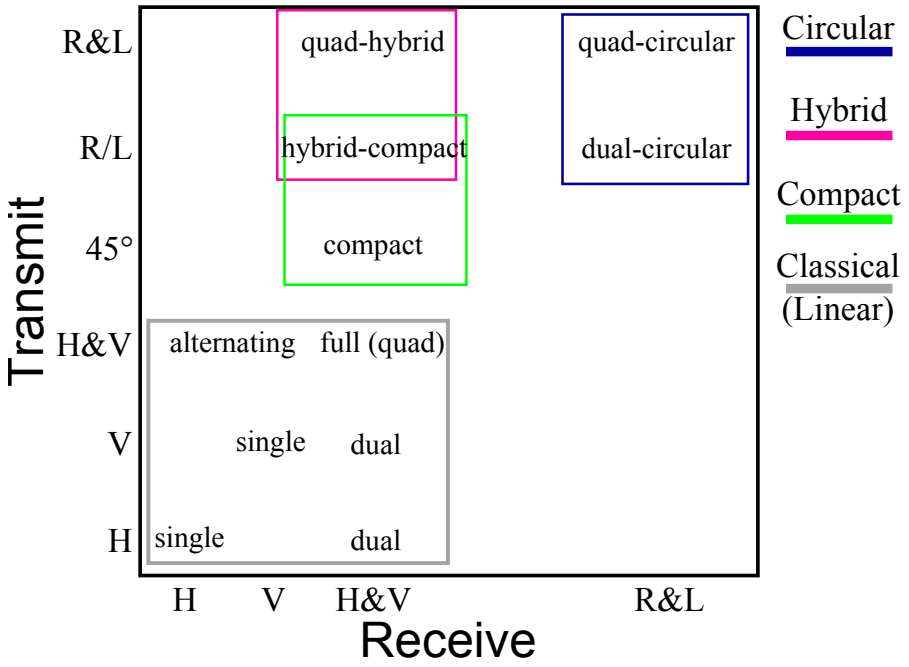

FIG. 2.1. Emerging and classical polarimetric SAR imaging modes

Single-Pol: Single-pol SAR systems were designed using a single linear polarization; transmitting and receiving horizontally or vertically polarized radiation. The NASA SIR-A (1981), and SIR-B (1984) were among the first single-pol (HH) SAR systems. Other single-pol (VV) space-borne SARs were the European ERS-1 (1991), and ERS-2 (1995).

Dual-Pol: In conventional dual-pol SAR modes, two linear polarizations are considered, providing (HH, HV) or (VH, VV) data. Some SARs are also capable of providing alternating (HH, VV) data (e. g., ENVISAT ASAR). This mode is unique since it directly measures the HH-VV correlation, which is commonly used to separate surface scattering from dihedral scattering. In this manuscript we refer to these three modes of operation as *classical linear* dual-pol modes. These modes play a major role in operational SAR remote sensing, since the majority of the operational polarimetric SAR data are collected in these dual-pol modes. Their scattering vectors are expressed as

$$\begin{aligned} \boldsymbol{k}_{\mathrm{DP1}} &= \left(S_{\mathrm{HH}}, S_{\mathrm{HV}}\right)^T \\ \boldsymbol{k}_{\mathrm{DP2}} &= \left(S_{\mathrm{VH}}, S_{\mathrm{VV}}\right)^T \\ \boldsymbol{k}_{\mathrm{DP3}} &= \left(S_{\mathrm{HH}}, S_{\mathrm{VV}}\right)^T . \end{aligned} \tag{2.1}$$

Full-Pol: Full polarimetric[1] systems alternately transmit two orthogonal polarizations and record both received polarizations (HH, HV, VH, VV). The full-pol scattering vector and covariance matrix

[1] In this manuscript, the terms *full-pol* and *quad-pol* are used as synonyms. However, in some publications [73] these terms are distinguished based on the scattering reciprocity, i. e., $S_{\mathrm{HV}} = S_{\mathrm{VH}}$ (quad-pol) and $S_{\mathrm{HV}} \neq S_{\mathrm{VH}}$ (full-pol).

are given by (1.21) and (1.22), respectively. The advantages of full polarimetry with respect to classical single and (linear) dual polarimetry are well-recognized in the remote sensing society [52, 74]. Full-pol systems provide the complete scattering matrix which allows the extraction of substantial information from a scene compared to other modes. However, full-pol systems are disadvantaged by a lower radar swath coverage, and higher antenna transmitter power requirements. Also, from an operational point of view, very little full-pol data are available; many of existing SAR systems provide full-pol data only on an experimental basis. As a result, hybrid and compact dual-pol systems have been widely investigated in recent years as a possible trade-off (sometimes substitute) in polarimetric SAR imagery.

2.2 HYBRID & COMPACT POLARIMETRY

In recent years, there have been emerging new SAR modes based on the transmission of polarization states other than the canonical H and V polarizations. Souyris et al. [10] introduced the $\pi/4$ CP mode, where the transmitted polarization is the superposition of linear horizontal and vertical polarizations and the received returns are recorded in both horizontal and vertical polarizations (45°H, 45°V). In another study, Stacy and Preiss [12] proposed the DCP mode based on a right (or left) circular polarization transmit, and right and left circular polarization receives ([RR, RL] or [LR, LL]). In a recent study, Raney [13] promoted a hybrid (circular linear) mode of operation (CL-pol), with a right (or left) circular polarization on transmission and two linear polarizations on reception ([RH, RV] or [LH, LV]). Figure 2.1 provides the outline of the emerging and classical polarimetric SAR imaging modes. Compared to full-pol systems, hybrid and compact dual-pol systems provide a wider swath width, and hence a greater area coverage. Their scattering vectors can be derived from the full-pol scattering vector given by (1.21). As an example, CL-pol mode is further detailed; in CL-pol mode a right-circular illumination is achieved by $\boldsymbol{E}^t = 1/\sqrt{2}(1,-i)^T$. From (1.20), the received field is given by $\boldsymbol{E}^r = 1/\sqrt{2}\,(S_{\mathrm{HH}} - iS_{\mathrm{HV}}, -iS_{\mathrm{VV}} + S_{\mathrm{HV}})^T$. Hence, considering $E_{\mathrm{H}} = (1,0)\boldsymbol{E}^r$ and $E_{\mathrm{V}} = (0,1)\boldsymbol{E}^r$, the CL-pol scattering vector is expressed as [13]

$$\begin{aligned}\boldsymbol{k}_{\text{CL-pol}} &= (E_{\mathrm{H}}, E_{\mathrm{V}})^T \\ &= \frac{1}{\sqrt{2}}\,(S_{\mathrm{HH}} - iS_{\mathrm{HV}}, -iS_{\mathrm{VV}} + S_{\mathrm{VH}})^T\,. \end{aligned} \tag{2.2}$$

The scattering vectors for the $\pi/4$ [10], and DCP [12] (with right circular transmit) are derived in the same fashion

$$\boldsymbol{k}_{\pi/4} = \frac{1}{\sqrt{2}} \left(S_{\mathrm{HH}} + S_{\mathrm{HV}}, S_{\mathrm{VV}} + S_{\mathrm{VH}}\right)^T \tag{2.3}$$

$$\boldsymbol{k}_{\mathrm{DCP}} = \frac{1}{2} \left(S_{\mathrm{HH}} - S_{\mathrm{VV}} + i\left[S_{\mathrm{HV}} + S_{\mathrm{VH}}\right], i\left[S_{\mathrm{HH}} + S_{\mathrm{VV}}\right] + S_{\mathrm{HV}} - S_{\mathrm{VH}}\right)^T . \tag{2.4}$$

Under the scattering reciprocity and in the backscatter alignment convention, we have $S_{\mathrm{HV}} = S_{\mathrm{VH}}$ [54], and thus, the above dual-pol scattering vectors are simplified accordingly. The related covariance matrices can be expressed as

$$\begin{aligned} \boldsymbol{C}_{\text{CL-pol}} &= \left\langle \boldsymbol{k}_{\text{CL-pol}} \boldsymbol{k}_{\text{CL-pol}}{}^{\dagger} \right\rangle \\ &= \frac{1}{2} \left\langle \begin{pmatrix} |S_{\mathrm{HH}}|^2 & iS_{\mathrm{HH}}S_{\mathrm{VV}}^* \\ -iS_{\mathrm{VV}}S_{\mathrm{HH}}^* & |S_{\mathrm{VV}}|^2 \end{pmatrix} \right\rangle \\ &\quad + \frac{1}{2} \left\langle \begin{pmatrix} |S_{\mathrm{HV}}|^2 & -i|S_{\mathrm{HV}}|^2 \\ i|S_{\mathrm{HV}}|^2 & |S_{\mathrm{HV}}|^2 \end{pmatrix} \right\rangle \\ &\quad + \frac{1}{2} \left\langle \begin{pmatrix} -2\Im(S_{\mathrm{HH}}S_{\mathrm{HV}}^*) & S_{\mathrm{HH}}S_{\mathrm{HV}}^* + S_{\mathrm{VV}}^*S_{\mathrm{HV}} \\ S_{\mathrm{HH}}^*S_{\mathrm{HV}} + S_{\mathrm{VV}}S_{\mathrm{HV}}^* & 2\Im(S_{\mathrm{VV}}S_{\mathrm{HV}}^*) \end{pmatrix} \right\rangle \end{aligned} \tag{2.5}$$

$$\begin{aligned} \boldsymbol{C}_{\pi/4} &= \left\langle \boldsymbol{k}_{\pi/4} \boldsymbol{k}_{\pi/4}{}^{\dagger} \right\rangle \\ &= \frac{1}{2} \left\langle \begin{pmatrix} |S_{\mathrm{HH}}|^2 & S_{\mathrm{HH}}S_{\mathrm{VV}}^* \\ S_{\mathrm{VV}}S_{\mathrm{HH}}^* & |S_{\mathrm{VV}}|^2 \end{pmatrix} \right\rangle \\ &\quad + \frac{1}{2} \left\langle \begin{pmatrix} |S_{\mathrm{HV}}|^2 & |S_{\mathrm{HV}}|^2 \\ |S_{\mathrm{HV}}|^2 & |S_{\mathrm{HV}}|^2 \end{pmatrix} \right\rangle \\ &\quad + \frac{1}{2} \left\langle \begin{pmatrix} 2\Re(S_{\mathrm{HH}}S_{\mathrm{HV}}^*) & S_{\mathrm{HH}}S_{\mathrm{HV}}^* + S_{\mathrm{VV}}^*S_{\mathrm{HV}} \\ S_{\mathrm{HH}}^*S_{\mathrm{HV}} + S_{\mathrm{VV}}S_{\mathrm{HV}}^* & 2\Re(S_{\mathrm{VV}}S_{\mathrm{HV}}^*) \end{pmatrix} \right\rangle \end{aligned} \tag{2.6}$$

$$\begin{aligned} \boldsymbol{C}_{\mathrm{DCP}} &= \left\langle \boldsymbol{k}_{\mathrm{DCP}} \boldsymbol{k}_{\mathrm{DCP}}{}^{\dagger} \right\rangle \\ &= \frac{1}{4} \left\langle \begin{pmatrix} |S_{\mathrm{HH}} - S_{\mathrm{VV}}|^2 & -i(S_{\mathrm{HH}} - S_{\mathrm{VV}})(S_{\mathrm{HH}} + S_{\mathrm{VV}})^* \\ i(S_{\mathrm{HH}} + S_{\mathrm{VV}})(S_{\mathrm{HH}} - S_{\mathrm{VV}})^* & |S_{\mathrm{HH}} + S_{\mathrm{VV}}|^2 \end{pmatrix} \right\rangle \\ &\quad + \frac{1}{4} \left\langle \begin{pmatrix} 4|S_{\mathrm{HV}}|^2 & 0 \\ 0 & 0 \end{pmatrix} \right\rangle \\ &\quad + \frac{1}{4} \left\langle \begin{pmatrix} 4\Im([S_{\mathrm{HH}} - S_{\mathrm{VV}}]S_{\mathrm{HV}}^*) & 2(S_{\mathrm{HH}} + S_{\mathrm{VV}})^*S_{\mathrm{HV}} \\ 2(S_{\mathrm{HH}} + S_{\mathrm{VV}})S_{\mathrm{HV}}^* & 0 \end{pmatrix} \right\rangle . \end{aligned} \tag{2.7}$$

Each of these 2×2 covariance matrices is derived as a sum of three terms; the first term contains only S_{HH} and S_{VV}, the second term

contains only S_{HV}, and the last term contains the linear co-pol/cross-pol correlations. Therefore, the above equations formulate the process of simulating the hybrid, compact, and circular dual-pol data from linear full-pol data represented by (1.22). Now that we have established a common ground, we can fully embrace the problem of interest. In what follows, we introduce the data and study sites used throughout this dissertation.

2.3 DATA AND STUDY SITES

Our database is composed of a variety of PolSAR images from different organizations, such as NASA/JPL, NASA/GSFC, ASF, NOAA, ESA, and MDA.

RADARSAT-2 is a Canadian C-band SAR satellite with dual- and quad-pol, right- and left-look imaging modes, launched in 2007.

RADARSAT-2, San Francisco: Among different data sets, the recent RADARSAT-2 full polarimetric data collected over San Francisco, CA, USA (37°45′0″N, 122°17′0″W) provides a valuable test case for our analysis. The Google Earth and Pauli RGB images of this data set are shown in Fig. 2.2. This data set consists of different terrain types such as urban, vegetation, and water regions, as outlined in Fig. 2.2(d). Moreover, San Francisco Bay provides us with interesting marine structures such as large and small ships, docks, and buoys, as outlined in Fig. 2.2(c) and (e). Buoys are distinctively shaped floating devices with many meteorological and navigational purposes. There exist precise nautical charts, usually used as an aid in navigation, which report the exact position of the buoys via different systems. In this study, we use such nautical charts from NOAA as ground truths for the position of the buoys. Figure 2.3 shows the NOAA nautical chart and the Pauli RGB image of a test region in San Francisco Bay with 12 buoys of interest (red boxes). Some of the buoys are bright enough to be readily visible on the Pauli RGB image.

Pauli RGB images are created from full polarimetric data as:
$|S_{HH} - S_{VV}|$ *Red*
$|S_{HV} + S_{VH}|$ *Green*
$|S_{HH} + S_{VV}|$ *Blue*

RADARSAT-2, Vancouver: Our second RADARSAT-2 data set is acquired over Vancouver, BC, Canada (49°15′0″N, 123°6′0″W). The Google Earth and Pauli RGB images of this data set are shown in Fig. 2.4. Three different regions of interest, i. e., urban, vegetation, and water, are outlined with red boxes in Fig. 2.4(b). These RADARSAT-2 C-band data sets are acquired in April 2008; San Francisco data set is in fine quad-pol FQ9 mode with an incident angle of about 29 degrees. Vancouver data set is in fine quad-pol FQ2 mode with an incident angle of about 21 degrees. Detailed characteristics of various RADARSAT-2 products can be found in [75].

AirSAR, San Francisco: Full polarimetric NASA/JPL AirSAR data sets from San Francisco and Flevoland (NL) are two classic data sets commonly used in PolSAR studies. Figure 2.5 shows the Google Earth and Pauli RGB images of the AirSAR San Francisco data which covers the same regions as the RADARSAT-2 data set of Fig. 2.2(d). This L-band

AirSAR data set is acquired in Aug. 1989, with an incident angle of about 20 degrees.

AirSAR, Flevoland: Figure 2.6 shows the Google Earth and Pauli RGB images of the Flevoland region (52°20′0″N, 5°23′0″E). This data set covers a large agricultural area of horizontally flat topography and homogeneous soils, some man-made structures, and a small water area. A region of interest, covering 8 high-voltage electrical transmission towers, is outlined in Fig. 2.6. These high-voltage transmission towers are manually identified on the Google Earth image, in Fig. 2.6(d), using red boxes. The important dihedral contribution from high-voltage transmission towers is observed from the pink color in the Pauli image. Some of these towers are bright enough to be identified on the Pauli RGB image whereas others are hidden in the agricultural environment.

AirSAR was a NASA/JPL side-looking full polarimetric P-, L- and C-band airborne SAR, operational from 1988 to 2004.

UAVSAR, Deepwater Horizon oil spill: In the study of oil spills, we use recent data sets from NASA/JPL UAVSAR, covering the Deepwater Horizon oil spill. The Deepwater Horizon oil spill occurred on April 20, 2010 in the Gulf of Mexico (28°44′11.8″N, 88°21′57.6″W). It is by far the worst oil spill in US history, with over 200 million gallons of leaked oil along the coastal areas of Louisiana, Mississippi, Alabama, and Florida. The spill has affected thousands of square kilometers and caused extensive damage to marine and wildlife habitats. Figure 2.7 shows a visible image of the spill area, acquired by Moderate-Resolution Imaging Spectroradiometer (MODIS) sensor on board the NASA Terra satellite. In this figure, the black cross shows the location of the Deepwater Horizon oil rig, the oil spill appears in gray color, and the UAVSAR acquisition flight paths are shown as blue and red boxes. The green (dashed) box shows the spill areas (marked as A and B) used throughout this study. The Pauli RGB images of the oil spill regions A and B are shown in Fig. 2.8. Oil spill appears as a dark patch, and the pink cross, marks an overlap point between the two scenes. The UAVSAR data sets are acquired on June 23, 2010, in quad-pol mode with incidence angle ranging from 25 to 65 degrees. In the context of offshore oil/gas platform detection, Gulf of Mexico is an interesting study case with nearly 4,000 active oil and gas platforms. Offshore oil/gas rigs are massive metal structures, usually in the form of a square, supported by vertical cylinders at the corners. Figure 2.9 shows two examples of oil/gas rigs present in the Gulf of Mexico. We use UAVSAR data of Mississippi River Delta, LA (29°0′43.5″N, 89°15′33.1″W), along with corresponding NOAA nautical charts in the study of oil/gas platform detection. The nautical chart and Pauli RGB image of this data set are shown in Fig. 2.10.

UAVSAR is a NASA/JPL full polarimetric L-band airborne SAR, operational since 2009.

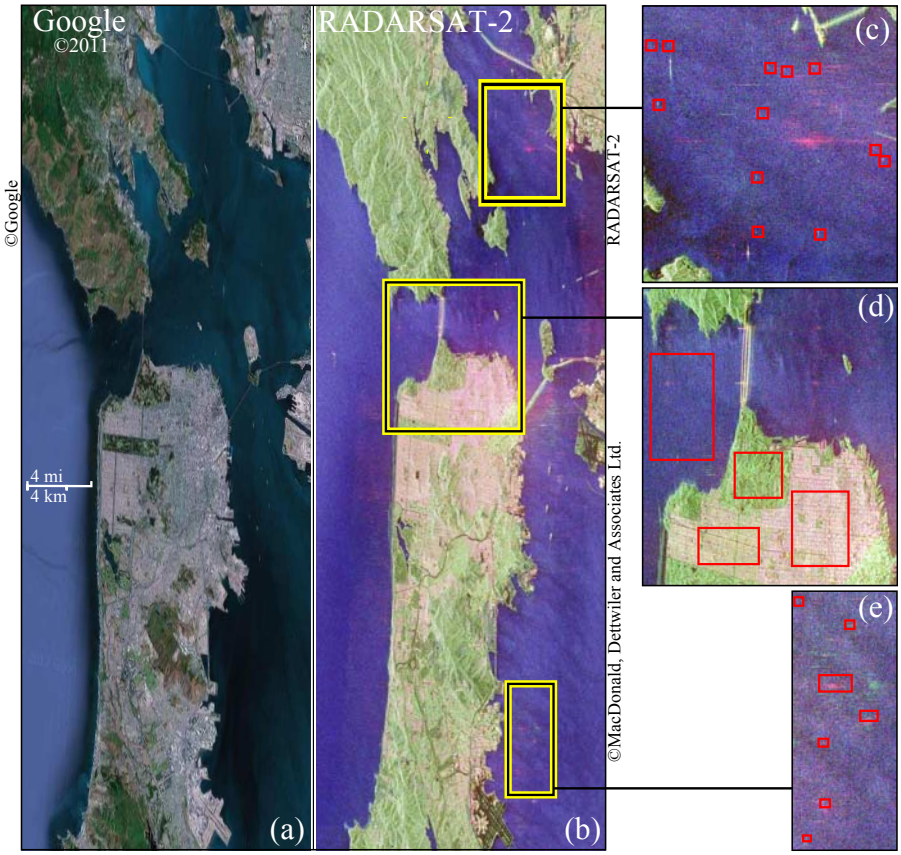

FIG. 2.2. San Francisco, CA, USA. (a) Google Earth image of the area. (b) Pauli RGB image of the RADARSAT-2 full polarimetric data set. (c) Zoom of an area used for buoy detection with 12 buoys of interest (red boxes). See Fig. 2.3, for more details. (d) Zoom of an area with four regions of interest (red boxes) showing from left to right, ocean, urban 1, park, and urban 2 regions. (e) Zoom of an area used for ship detection where the targets are outlined in red boxes. The original image in (b) has a size of 2820×14416 pixels.

Buoys are distinctively shaped oating devices, mainly used for meteorological and navigational purposes.

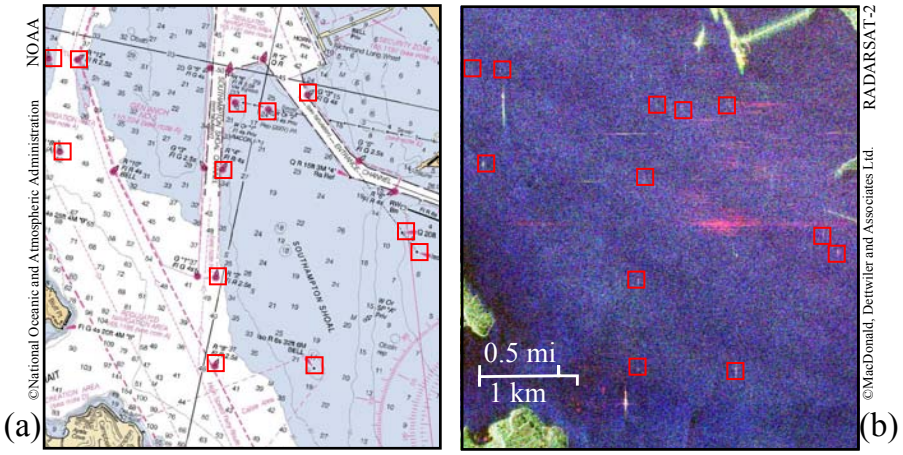

FIG. 2.3. San Francisco Bay, CA, USA. (a) NOAA nautical chart, used as a reference, showing the exact position of the buoys of interest (red boxes). (b) Pauli RGB image from RADARSAT-2 full polarimetric data.

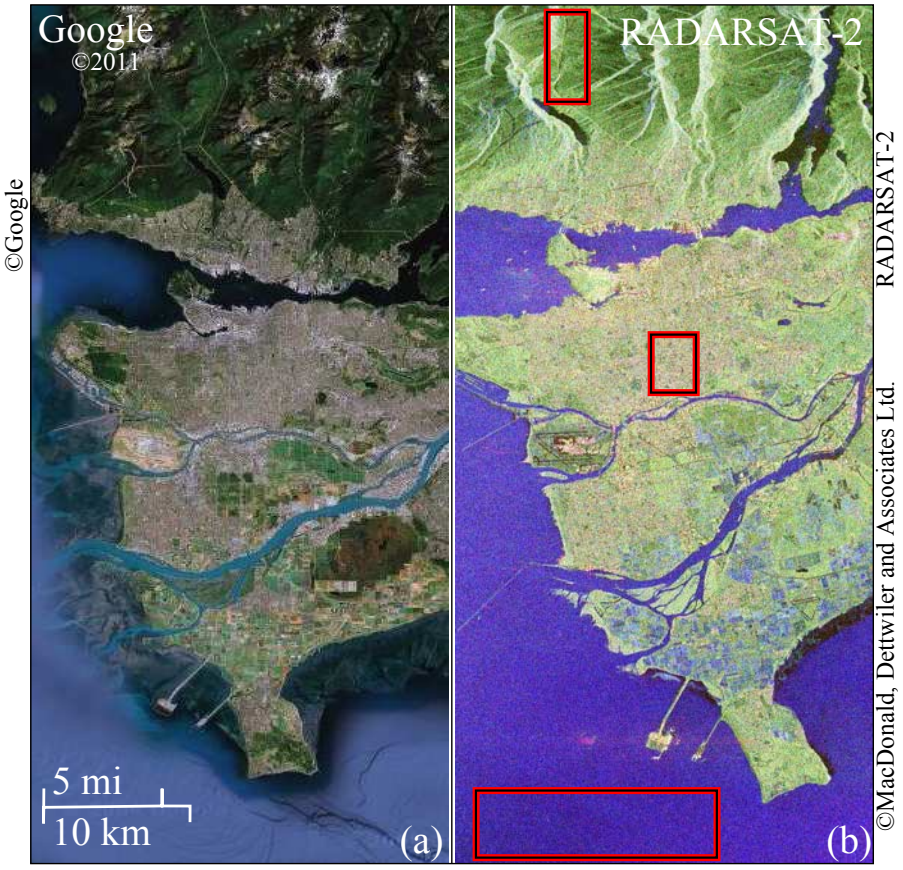

FIG. 2.4. Vancouver, BC, Canada. (a) Google Earth image of the area. (b) Pauli RGB image of the RADARSAT-2 full polarimetric data set. The outlined areas in (b) are (from top to bottom) vegetation, urban, and sea regions. The original image has a size of 1985 × 11393 pixels.

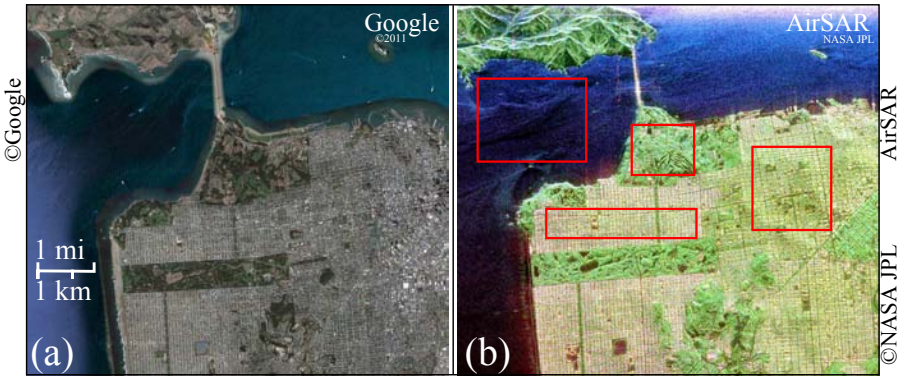

FIG. 2.5. San Francisco, CA, USA. (a) Google Earth image of the area. (b) Pauli RGB image of the NASA/JPL AirSAR full polarimetric data set. Four regions of interest are outlined with red boxes, showing from left to right, ocean, urban 1, park, and urban 2 regions. The original image in (b) has a size of 1024 × 900 pixels.

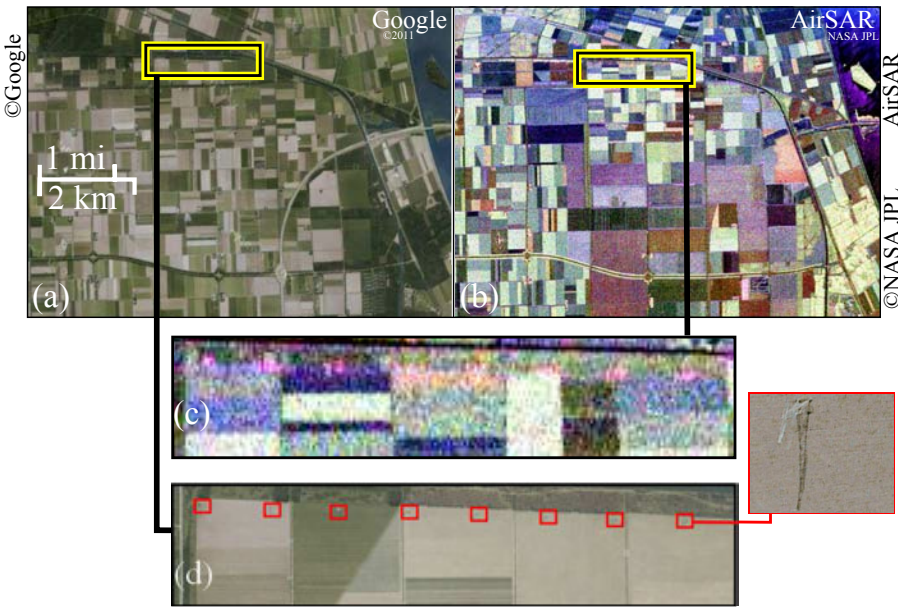

FIG. 2.6. Flevoland, The Netherlands. (a) Google Earth image of the area. (b) Pauli RGB image of the NASA/JPL AirSAR full polarimetric data set. A region of interest is outlined with a yellow box. (c-d) Zoom of the region of interest in which 8 high-voltage transmission towers are present. The original image in (b) has a size of 1024 × 750 pixels.

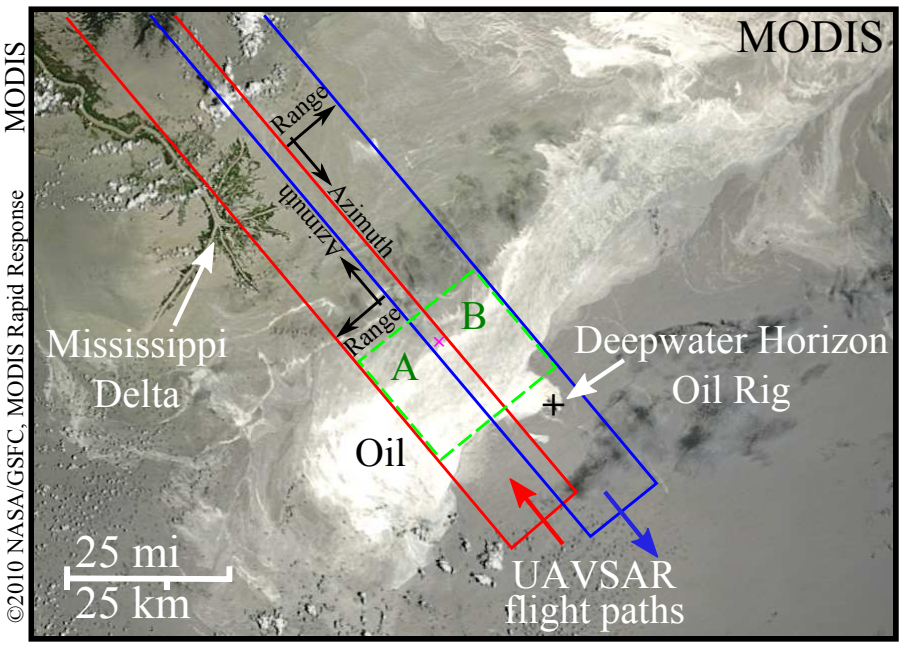

FIG. 2.7. NASA MODIS visible image of the Deepwater Horizon oil spill in northern Gulf of Mexico, USA. The outlined areas in blue and red show the acquisition flight paths of the UAVSAR polarimetric system. The green (dashed) box shows the study area used for oil spill detection. See Fig. 2.8 for more details.

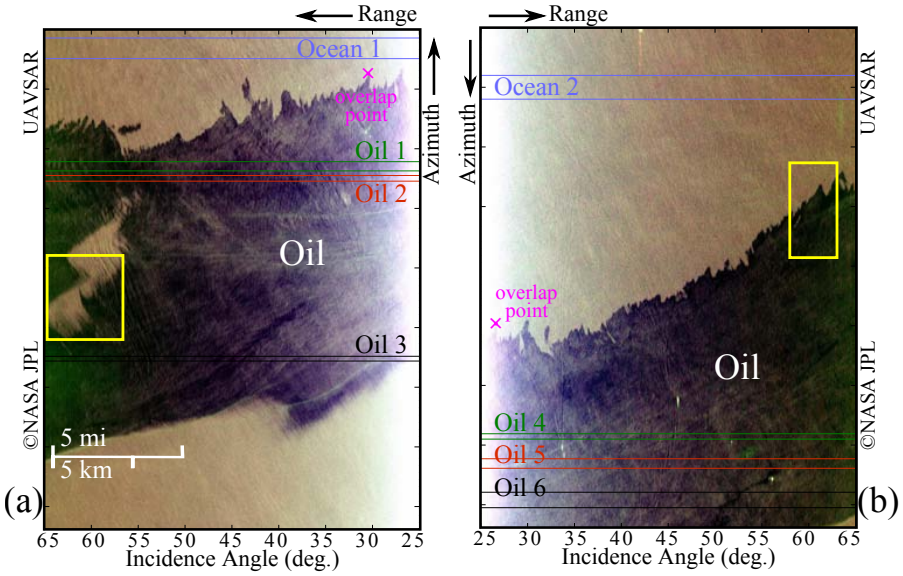

FIG. 2.8. NASA/JPL UAVSAR full polarimetric data sets A and B (outlined in Fig. 2.7), from the Deepwater Horizon oil spill in northern Gulf of Mexico, USA. (a) Pauli RGB image of the data set A. The original image has a size of 3155×4371 pixels. (b) Pauli RGB image of the data set B. The original image has a size of 3151×4201 pixels. The oil appears as a dark patch within the ocean clutter. Strong specular scattering is dominant around an incidence angle of 25°. The outlined regions of oil (oil 1–6) and ocean (ocean 1–2) are used in the study of the oil spill detection. The pink cross, marks an overlap point between (a) and (b).

FIG. 2.9. Examples of typical offshore oil/gas platforms in the Gulf of Mexico, USA.

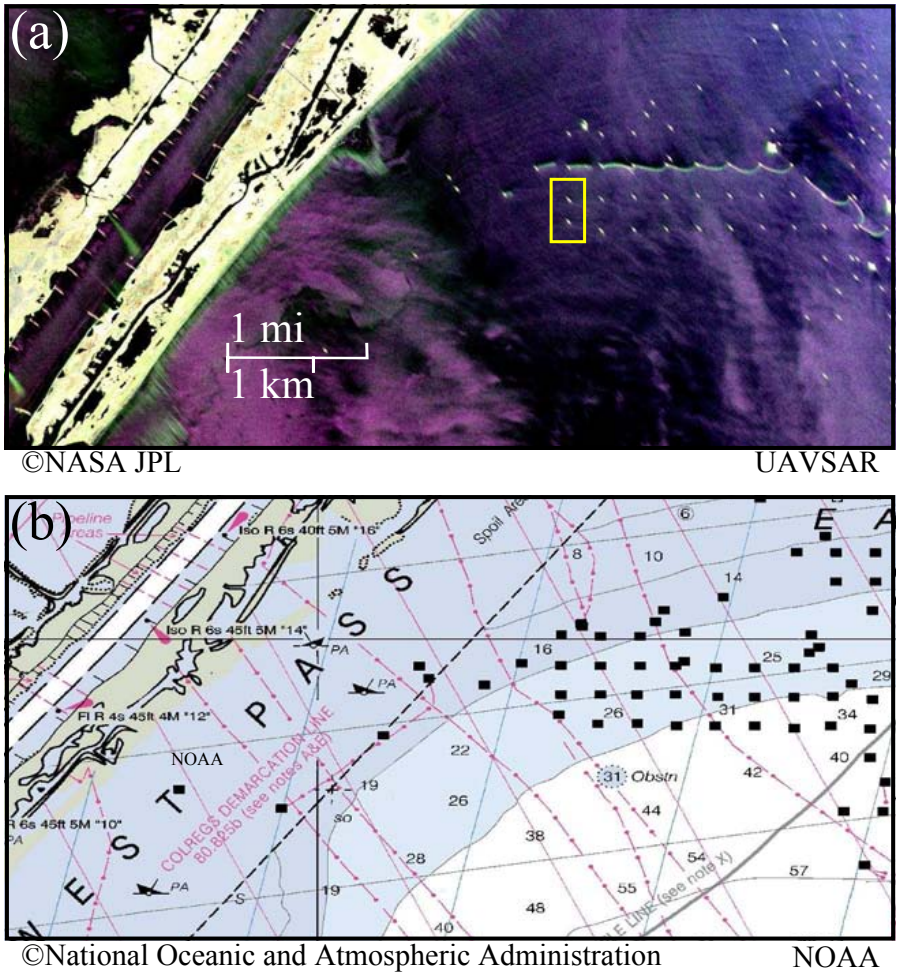

FIG. 2.10. Mississippi River Delta, LA, USA. (a) Pauli RGB image of a region of interest, used for oil-rig detection, from NASA/JPL UAVSAR full polarimetric data set. (b) NOAA nautical chart, used as a reference, showing the exact position of the oil platforms (black boxes). The original image in (a) has a size of 1600 × 800 pixels.

3

STATISTICAL ANALYSIS, THEORETICAL MODELING, AND DOP ESTIMATION IN DUAL-POL SAR

This is a one line proof . . .
if we start suf ciently far to the left.

— Math Lecturer
[Cambridge University]

The Degree of Polarization (DoP) has been considered as the most important parameter characterizing a partially polarized electromagnetic wave [1, 13, 44, 48]. The estimation of the DoP can help to determine the nature of the objects that backscatter the wave. It also provides an effective tool for assessing the performance of emerging hybrid/compact dual-pol modes with regard to classical dual- and full-pol modes. In this chapter, we study the statistical properties of dual-pol SAR data, and derive the joint distributions of the multi-look SAR intensity images (§ 3.1 & § 3.2). Based on these distributions, ML and MoM estimators of the DoP are derived in § 3.3, for both coherent and incoherent dual-pol SAR systems. The generalization of the DoP for hybrid, compact and linear dual-pol SAR modes is introduced in § 3.4.

3.1 STATISTICAL ANALYSIS OF MULTILOOK POLARIMETRIC SAR IMAGERY

The estimation of the DoP from expression (1.10) can be conducted by estimating the parameters of the covariance matrix, i. e., a_i, $i = 1, \ldots, 4$. These parameters are directly related to the statistics of the multilook intensity images from the modified Stokes vector $\widetilde{\mathbf{g}}$ given in (1.19). In what follows, we study the statistical properties of $\widetilde{\mathbf{g}}$, and derive the joint distribution of the multilook SAR intensity images $\widetilde{\mathrm{g}}_i$, $i = 0, \ldots, 3$.

It is well known that, under the usual assumption of fully developed speckle, the Jones vector $\boldsymbol{E}$ is distributed according to a complex circular Gaussian distribution [56] whose PDF is

$$p_{\mathrm{G}}(\boldsymbol{E}) = \frac{1}{\pi^2 |\boldsymbol{\Gamma}|} \exp\left(-\boldsymbol{E}^{\dagger}\boldsymbol{\Gamma}^{-1}\boldsymbol{E}\right). \tag{3.1}$$

Considering q independent (1-look) samples $\boldsymbol{E}_j, j = 1, \ldots, q$ from such a distribution, the q-look Hermitian covariance matrix $\overline{\boldsymbol{\Gamma}}$ is given by

$$\overline{\boldsymbol{\Gamma}} = \frac{1}{q}\sum_{j=1}^{q} \boldsymbol{E}_j \boldsymbol{E}_j^{\dagger}. \tag{3.2}$$

Let $\mathbf{A}_{\boldsymbol{E}} = q\overline{\boldsymbol{\Gamma}}$. Based on § 1.4.2, the matrix $\mathbf{A}_{\boldsymbol{E}}$ is distributed according to a Wishart distribution whose Laplace transform is

$$L_{\mathbf{A}_{\boldsymbol{E}}}(\boldsymbol{\Theta}) = \mathsf{E}\left[\exp\left(-\mathrm{tr}\left[\boldsymbol{\Theta}^T \mathbf{A}_{\boldsymbol{E}}\right]\right)\right] \tag{3.3}$$

$$= |\mathbb{I}_2 + \boldsymbol{\Gamma}\boldsymbol{\Theta}|^{-q} \tag{3.4}$$

where $\mathbb{I}_2$ is the 2×2 identity matrix, $\boldsymbol{\Theta}$ is a 2×2 complex Hermitian matrix, and $|\cdot|$ represents the determinant. The random Hermitian matrix $\mathbf{A}_{\boldsymbol{E}}$ is expressed in terms of the q-look Stokes parameters as

$$\begin{aligned} \mathbf{A}_{\boldsymbol{E}} &= \sum_{j=1}^{q} \begin{pmatrix} |E_{\mathrm{H}j}|^2 & E_{\mathrm{H}j}{E_{\mathrm{V}j}}^* \\ E_{\mathrm{V}j}{E_{\mathrm{H}j}}^* & |E_{\mathrm{V}j}|^2 \end{pmatrix} \\ &= \frac{q}{2} \begin{pmatrix} g_0 + g_1 & g_2 - ig_3 \\ g_2 + ig_3 & g_0 - g_1 \end{pmatrix}. \end{aligned} \tag{3.5}$$

By definition, the Laplace transform of the PDF of $\widetilde{\mathbf{g}}$ is given by

$$\begin{aligned} L_{\widetilde{\mathbf{g}}}(\boldsymbol{\theta}) &= \mathsf{E}\left[\exp\left(-\boldsymbol{\theta}^T \widetilde{\mathbf{g}}\right)\right] \\ \boldsymbol{\theta} &= (\theta_1, \theta_2, \theta_3, \theta_4)^T. \end{aligned} \tag{3.6}$$

Therefore, using (3.6) & (1.19) on one side, and (3.3) & (3.5) on the other side, one can obtain

$$\begin{aligned} L_{\widetilde{\mathbf{g}}}(\boldsymbol{\theta}) &= \mathsf{E}\left[\exp\left(-\mathrm{tr}\left[\boldsymbol{\Theta}^T \mathbf{A}_{\boldsymbol{E}}\right]\right)\right] \\ &= L_{\mathbf{A}_{\boldsymbol{E}}}(\boldsymbol{\Theta}) \end{aligned} \tag{3.7}$$

$$\boldsymbol{\Theta} = \begin{pmatrix} \Theta_1 & \Theta_3 + i\Theta_4 \\ \Theta_3 - i\Theta_4 & \Theta_2 \end{pmatrix} \tag{3.8}$$

$$\begin{aligned} \Theta_1 &= \frac{2\theta_1 + \theta_3 + \theta_4}{2q}, \quad \Theta_3 = \frac{\theta_3}{2q} \\ \Theta_2 &= \frac{2\theta_2 + \theta_3 + \theta_4}{2q}, \quad \Theta_4 = \frac{\theta_4}{2q} \end{aligned}$$

Finally, using (3.4) and (3.7), and after calculating the determinant, we obtain the Laplace transform of the PDF of the modified Stokes vector $\widetilde{\mathbf{g}}$ as

$$L_{\widetilde{\mathbf{g}}}(\boldsymbol{\theta}) = \frac{1}{\widetilde{P}(\boldsymbol{\theta})^q} \tag{3.9}$$

$$\widetilde{P}(\boldsymbol{\theta}) = 1 + \boldsymbol{\alpha}^T\boldsymbol{\theta} + \beta\left[2\theta_1\theta_2 + \theta_3\theta_4 + (\theta_1+\theta_2)(\theta_3+\theta_4)\right] \tag{3.10}$$

$$\boldsymbol{\alpha} = \frac{1}{q}\left(a_1, a_2, \frac{a_1+a_2}{2} + a_3, \frac{a_1+a_2}{2} + a_4\right)^T \tag{3.11}$$

$$\beta = \frac{1}{2q^2}\left(a_1a_2 - a_3^2 - a_4^2\right). \tag{3.12}$$

We see that $\widetilde{P}(\boldsymbol{\theta})$ is a quadratic affine polynomial, and thus, the distribution of the q-look intensity vector $\widetilde{\mathbf{g}}$ is an MGD with $d = 4$ (see § 1.4.3 for the related discussion). We note that, $d \in \mathbb{N}$ is the dimension of the gamma distribution, that is, the number of available intensity images. The parameter q is both the number of looks and the shape parameter of the gamma distribution. The above results are valid for any $q > 0$, thus q can be chosen as either the number of looks (with values in the set of positive integers $\mathbb{N}$) or the Equivalent Number of Looks (ENL) [52, 76] (with values in the set of real positive numbers $\mathbb{R}^+$). It is worth noting that while the introduced modified Stokes vector $\widetilde{\mathbf{g}}$ follows an MGD, the Stokes vector $\mathbf{g}$ is not distributed according to an MGD. Following a similar approach, we obtain a $\boldsymbol{\Theta}$ for the Stokes vector $\mathbf{g}$, expressed as

$$\boldsymbol{\Theta} = \frac{1}{q}\begin{pmatrix} \theta_1+\theta_2 & \theta_3 + i\theta_4 \\ \theta_3 - i\theta_4 & \theta_1 - \theta_2 \end{pmatrix} \tag{3.13}$$

which gives us the following polynomial

$$\begin{aligned} P(\boldsymbol{\theta}) &= 1 + \boldsymbol{\alpha}^T\boldsymbol{\theta} + \beta\left[-\theta_1^2 + \theta_2^2 + \theta_3^2 + \theta_4^2\right] \\ \boldsymbol{\alpha} &= \frac{1}{q}\left(a_1 + a_2, a_1 - a_2, 2a_3, 2a_4\right)^T \\ \beta &= \frac{1}{q^2}\left(a_3^2 + a_4^2 - a_1a_2\right). \end{aligned} \tag{3.14}$$

We clearly see that $P(\boldsymbol{\theta})$ is not an affine polynomial (since it does not satisfy $\partial^2 P/\partial\theta_j^2 = 0$), and thus, the Stokes vector $\mathbf{g}$ is not distributed according to an MGD. Therefore, considering the modified Stokes vector $\widetilde{\mathbf{g}}$, along with the properties of MGDs, can simplify the analysis and the process of deriving different parameter estimators. [1]

[1] The distribution of the Stokes vector is, however, related to the distribution of $\widetilde{\mathbf{g}}$ by a change of variables.

3.2 MARGINAL DISTRIBUTION OF TWO MULTI-LOOK INTENSITY IMAGES

In the particular case of two multi-look intensity images ($d = 2$), the distribution of $\widetilde{\mathbf{g}}_b = (\widetilde{\mathrm{g}}_0, \widetilde{\mathrm{g}}_1)^T$ is a BGD whose PDF is expressed as

$$p_{\mathrm{BGD}}(\widetilde{\mathbf{g}}_b) = \exp\left(-\frac{a_2\widetilde{\mathrm{g}}_0 + a_1\widetilde{\mathrm{g}}_1}{2q\beta}\right)\frac{\widetilde{\mathrm{g}}_0^{q-1}\widetilde{\mathrm{g}}_1^{q-1}}{(2\beta)^q\Gamma(q)} \times f_q\left(c\widetilde{\mathrm{g}}_0\widetilde{\mathrm{g}}_1\right)\mathbb{I}_{\mathbb{R}_+^2}\left(\widetilde{\mathbf{g}}_b\right) \tag{3.15}$$

where $\beta = (a_1a_2 - r)/2q^2$, $c = q^2r/\left(a_1a_2 - r\right)^2$, $r = a_3^2 + a_4^2$, $\mathbb{I}_{\mathbb{R}_+^2}\left(\widetilde{\mathbf{g}}_b\right)$ is the indicator function on $\mathbb{R}^+ \times \mathbb{R}^+$, and $f_q(z) = \sum_{j=0}^{\infty} z^j/\Gamma(q+j)j!$ is related to confluent hypergeometric and modified Bessel functions [72, p. 374]. We see that this distribution is parametrized by a_1, a_2, and r. Hence, we can derive the ML estimators of these three parameters. Moreover, based on the first- and second-order moments of such a distribution (given in § 1.4.3), the moment estimators of a_1, a_2, and r can also be derived.

The above distributions, derived for $q \in \mathbb{R}^+$ and $d \in \{1,2,3,4\}$, generalize those of Touzi and Lopes [77, eq. 16] derived for $q = 1$ and $d = 2$, Lee et al. [78, eq. 30] derived for $q \in \mathbb{N}$ and $d = 2$, and Chatelain et al. [79] derived for $q = 1$ and $d \in \{1,2,3,4\}$. Using the above results, we can derive the estimators of the DoP based on any number of available images $d \in \{2,3,4\}$. For the purpose of this study, we consider two particular cases of $d = 4$, related to the coherent (complex) dual-pol SAR data, and $d = 2$ related to incoherent (intensity) dual-pol SAR imagery.

3.3 DOP ESTIMATION

3.3.1 *Coherent Dual-Pol SAR*

3.3.1.1 *Maximum Likelihood Estimators*

Recent SAR systems can coherently measure dual-pol complex signals reflected from a scene. The acquired dual-pol complex SAR images can directly or indirectly lead to the covariance matrix, the Stokes vector, and the four intensity images of the modified Stokes vector. Using the properties of MGDs, the ML estimator of $\mathsf{E}\left[\widetilde{\mathbf{g}}\right]$ is $1/n\sum_{j=1}^{n}\widetilde{\mathbf{g}}\left[j\right]$, and thus, the ML estimator of $\boldsymbol{a} = (a_1, a_2, a_3, a_4)^T$ is given by

$$\widehat{\boldsymbol{a}}_{\mathrm{ML}} = \boldsymbol{M}\left(\frac{1}{n}\sum_{j=1}^{n}\widetilde{\mathbf{g}}\,[j]\right) \tag{3.16}$$

$$\boldsymbol{M} = \begin{pmatrix} 1 & 0 & 0 & 0 \\ 0 & 1 & 0 & 0 \\ -\frac{1}{2} & -\frac{1}{2} & 1 & 0 \\ -\frac{1}{2} & -\frac{1}{2} & 0 & 1 \end{pmatrix}$$

where n is the number of pixels used for the estimation. In practice, $\widehat{a}_{l_{\mathrm{ML}}}, l = 1, \ldots, 4$ is calculated for each pixel of the multi-look intensity image by using a sliding square window (centered on the considered pixel) and computing the empirical mean over the n pixels contained in the window. The ML estimator of $\boldsymbol{a}$ is an unbiased and efficient estimator. Based on the functional invariance principle [80], the estimators in (3.16) are then plugged into (1.10), yielding the DoP ML estimator for multilook coherent dual-pol SAR imagery

$$\widehat{\mathcal{P}}_{\mathrm{ML}} = \left[1 - \frac{4\left(\widehat{a}_{1_{\mathrm{ML}}}\widehat{a}_{2_{\mathrm{ML}}} - [\widehat{a}^2_{3_{\mathrm{ML}}} + \widehat{a}^2_{4_{\mathrm{ML}}}]\right)}{(\widehat{a}_{1_{\mathrm{ML}}} + \widehat{a}_{2_{\mathrm{ML}}})^2}\right]^{\frac{1}{2}}. \tag{3.17}$$

The above ML estimator of the DoP is the optimal (unbiased, convergent, and efficient) estimator of the DoP. Interestingly, it is also the classical DoP estimator [50]. We highlight that the estimation of the DoP using (3.17) involves significantly low computational complexity compared with other well-known PolSAR discriminators. It is performed through the averaging of PolSAR images, for which efficient algorithms have already been implemented on board of PolSAR systems. The latter suggests that the DoP, readily adaptable for on-board implementation, can be an interesting candidate for operational real-time PolSAR applications. We further detail this idea in Chapter 4.

3.3.1.2 *Cramer-Rao Bound*

The ML estimators are known to be asymptotically unbiased and asymptotically efficient under mild regularity conditions. The asymptotic variance of the estimator (3.17) is its Cramer-Rao bound. Let us consider the function $g : \boldsymbol{a} \longmapsto g(\boldsymbol{a}) = \mathcal{P}$. Hence, the asymptotic variance of $\widehat{\mathcal{P}}_{\mathrm{ML}}$ can be derived as follows

$$\underset{\text{asym}}{\mathrm{Var}}\left(\widehat{\mathcal{P}}_{\mathrm{ML}}\right) = \boldsymbol{G}^T \mathrm{Cov}\left(\widehat{\boldsymbol{a}}_{\mathrm{ML}}\right)\boldsymbol{G} \tag{3.18}$$

where $\mathrm{Cov}\left(\widehat{\boldsymbol{a}}_{\mathrm{ML}}\right)$ is the covariance matrix of $\widehat{\boldsymbol{a}}_{\mathrm{ML}}$, and $\boldsymbol{G}$ is the gradient of the function g, given by

$$\boldsymbol{G} = G_0 \left[\frac{a_1 a_2 - a_2^2 - 2a_3^2 - 2a_4^2}{(a_1 + a_2)^2}, \frac{a_1 a_2 - a_1^2 - 2a_3^2 - 2a_4^2}{(a_1 + a_2)^2}, \frac{2a_3}{a_1 + a_2}, \frac{2a_4}{a_1 + a_2} \right]^T \tag{3.19}$$

$$G_0 = \frac{2}{\left[(a_1 - a_2)^2 + 4a_3^2 + 4a_4^2\right]^{\frac{1}{2}}}.$$

Therefore, to calculate $\underset{\text{asym}}{\mathrm{Var}}\left(\widehat{\mathcal{P}}_{\mathrm{ML}}\right)$, we need to determine $\mathrm{Cov}\left(\widehat{\boldsymbol{a}}_{\mathrm{ML}}\right)$. The covariance matrix of $\widehat{\boldsymbol{a}}_{\mathrm{ML}}$ can be derived using (3.16)

$$\mathrm{Cov}\left(\widehat{\boldsymbol{a}}_{\mathrm{ML}}\right) = \frac{1}{n} \boldsymbol{M} \mathrm{Cov}\left(\widetilde{\mathbf{g}}\right) \boldsymbol{M}^T. \tag{3.20}$$

The covariance matrix of $\widetilde{\mathbf{g}}$ can be derived using the second order moments of a BGD, given in § 1.4.3. After some calculations, one can find that

$$\mathrm{Cov}\left(\widehat{\boldsymbol{a}}_{\mathrm{ML}}\right) = \frac{1}{nq} \begin{pmatrix} a_1^2 & a_3^2 + a_4^2 & a_1 a_3 & a_1 a_4 \\ a_3^2 + a_4^2 & a_2^2 & a_2 a_3 & a_2 a_4 \\ a_1 a_3 & a_2 a_3 & [a_1 a_2 + a_3^2 - a_4^2]/2 & a_3 a_4 \\ a_1 a_4 & a_2 a_4 & a_3 a_4 & [a_1 a_2 - a_3^2 + a_4^2]/2 \end{pmatrix}.$$

Plugging the above covariance matrix in (3.18), we finally obtain the Cramer-Rao bound as

$$\underset{\text{asym}}{\mathrm{Var}}\left(\widehat{\mathcal{P}}_{\mathrm{ML}}\right) = \boldsymbol{G}^T \mathrm{Cov}\left(\widehat{\boldsymbol{a}}_{\mathrm{ML}}\right) \boldsymbol{G} = \frac{(1 - \mathcal{P}^2)^2}{2nq} \tag{3.21}$$

where q is the number of looks and n is the number of samples in the estimation window. The above expression gives the Cramer-Rao bound for the classical estimator of the DoP. Interestingly, we see that the asymptotic performance of this estimator depends directly on the value of the DoP; the higher the polarization value, the better the performance. Moreover, we clearly see the effect of the parameters n and q on the performance improvement; the higher the number of looks (or samples in the estimation window), the better the performance. These are confirmed through our experimental results detailed in Chapter 5. We highlight that for the particular case of $q = 1$, and after some calculations (see [80, eq. 3.16]), one can show that (3.21) is in agreement with the results obtained by Chatelain et al. [79] for the estimation of $\mathcal{P}^2$. Under mild regularity conditions, the ML estimator is asymptotically normally distributed. Therefore, the asymptotic distribution of $\widehat{\mathcal{P}}_{\mathrm{ML}}$ is expressed as

$$\widehat{\mathcal{P}}_{\mathrm{ML}} \underset{\text{asym}}{\sim} \mathcal{N}\left(\mathcal{P}, \frac{[1 - \mathcal{P}^2]^2}{2nq}\right). \tag{3.22}$$

3.3.2 *Incoherent Dual-Pol SAR*

Incoherent dual-pol SAR systems only measure a pair of detected amplitudes, useful to create two multilook intensity images from a scene. However, four intensity images (or the complex covariance matrix) are necessary in the classical estimation of the DoP. Hence, the estimation of the DoP based on only two intensity images is a challenging task. Fortunately, the properties of MGDs can open the way for estimating the DoP based on two intensity images.

3.3.2.1 *Maximum Likelihood Estimators*

The ML method can be applied in the bivariate case ($d = 2$) since a closed-form expression of the density is available as shown in (3.15). This density is parametrized by $\boldsymbol{\vartheta} = (a_1, a_2, r)$. The ML estimators of a_1, a_2, and r can be calculated by differentiating the log-likelihood function. Let us consider n independent vectors $\widetilde{\mathbf{g}}_b[1], \ldots, \widetilde{\mathbf{g}}_b[n]$ from such a distribution. The joint density function for all the observations is expressed as $p(\widetilde{\mathbf{g}}_{1:n}) = \prod_{j=1}^{n} p_{\text{BGD}}(\widetilde{\mathbf{g}}_b[j])$. Therefore, the corresponding log-likelihood function can be derived as

$$\begin{aligned}\ln \mathcal{L}(\widetilde{\mathbf{g}}_{1:n}; \boldsymbol{\vartheta}) &= \sum_{j=1}^{n} \ln p_{\text{BGD}}(\widetilde{\mathbf{g}}_b[j]; \boldsymbol{\vartheta}) \\ &= -nq\ln(2\beta) \\ &\quad - \frac{na_2\langle\widetilde{\mathrm{g}}_0\rangle + na_1\langle\widetilde{\mathrm{g}}_1\rangle}{2q\beta} \\ &\quad + \sum_{j=1}^{n} \ln f_q\left(c\widetilde{\mathrm{g}}_0[j]\,\widetilde{\mathrm{g}}_1[j]\right) \\ &\quad + \sum_{j=1}^{n} \ln \frac{\widetilde{\mathrm{g}}_0^{q-1}[j]\,\widetilde{\mathrm{g}}_1^{q-1}[j]}{\Gamma(q)}.\end{aligned} \tag{3.23}$$

Removing the terms which do not depend on $\boldsymbol{\vartheta}$, and setting $\beta = (a_1a_2 - r)/2q^2$, we obtain a simplified log-likelihood function as

$$\begin{aligned}\ell &= -nq\ln(a_1a_2 - r) \\ &\quad - \sum_{i=1}^{2} \frac{nq\langle\widetilde{\mathrm{g}}_i\rangle}{a_i(1 - r/a_1a_2)} \\ &\quad + \sum_{j=1}^{n} \ln f_q\left(c\widetilde{\mathrm{g}}_0[j]\,\widetilde{\mathrm{g}}_1[j]\right)\end{aligned} \tag{3.24}$$

where $c = q^2 r / (a_1a_2 - r)^2$, and $\langle\widetilde{\mathrm{g}}_i\rangle = 1/n \sum_{j=1}^{n} \widetilde{\mathrm{g}}_i[j]$ is the sample mean of $\widetilde{\mathrm{g}}_i$ for $i = 0, 1$. By differentiating the log-likelihood function ℓ

with respect to a_1, a_2, and r, and setting $f_q'(z) = f_{q+1}(z)$, the following set of equations is obtained

$$0 = \frac{nq\,\langle \widetilde{\mathrm{g}}_0 \rangle}{1 - r/a_1 a_2} - nqa_1 - \frac{rq^2 a_1}{(1 - r/a_1 a_2)^2}\Delta \tag{3.25}$$

$$0 = \frac{nq\,\langle \widetilde{\mathrm{g}}_1 \rangle}{1 - r/a_1 a_2} - nqa_2 - \frac{rq^2 a_2}{(1 - r/a_1 a_2)^2}\Delta \tag{3.26}$$

$$\begin{aligned} 0 = &\frac{nq\,\langle \widetilde{\mathrm{g}}_0 \rangle}{(1 - r/a_1 a_2)a_1} + \frac{nq\,\langle \widetilde{\mathrm{g}}_1 \rangle}{(1 - r/a_1 a_2)a_2} \\ &- nq - \frac{(1 + r/a_1 a_2)q^2}{(1 - r/a_1 a_2)^2}\Delta \end{aligned} \tag{3.27}$$

$$\Delta = \frac{1}{a_1 a_2}\sum_{j=1}^{n} \widetilde{\mathrm{g}}_0\,[j]\,\widetilde{\mathrm{g}}_1\,[j]\,\frac{f_{q+1}\left(c\widetilde{\mathrm{g}}_0\,[j]\,\widetilde{\mathrm{g}}_1\,[j]\right)}{f_q\left(c\widetilde{\mathrm{g}}_0\,[j]\,\widetilde{\mathrm{g}}_1\,[j]\right)}$$

Using these equations and after some calculations, the ML estimators of a_1 and a_2 are obtained as

$$\begin{aligned} \widehat{a}_{1_{\mathrm{ML}}} &= \frac{1}{n}\sum_{j=1}^{n} \widetilde{\mathrm{g}}_0\,[j] \\ \widehat{a}_{2_{\mathrm{ML}}} &= \frac{1}{n}\sum_{j=1}^{n} \widetilde{\mathrm{g}}_1\,[j] \end{aligned} \tag{3.28}$$

The ML estimator of r is more complex. Using the above equations, and replacing a_1 & a_2 with their ML estimators, one can show that the ML estimator of r, denoted as $\widehat{r}_{\mathrm{ML}}$, satisfies the following nonlinear relation

$$\widehat{a}_{1_{\mathrm{ML}}}\widehat{a}_{2_{\mathrm{ML}}} - \widehat{r}_{\mathrm{ML}} - \frac{q}{n}\sum_{j=1}^{n} \widetilde{\mathrm{g}}_0\,[j]\,\widetilde{\mathrm{g}}_1\,[j]\,\frac{f_{q+1}\left(\widehat{c}\,\widetilde{\mathrm{g}}_0\,[j]\,\widetilde{\mathrm{g}}_1\,[j]\right)}{f_q\left(\widehat{c}\,\widetilde{\mathrm{g}}_0\,[j]\,\widetilde{\mathrm{g}}_1\,[j]\right)} = 0 \tag{3.29}$$

$$\widehat{c} = \frac{q^2\widehat{r}_{\mathrm{ML}}}{\left(\widehat{a}_{1_{\mathrm{ML}}}\widehat{a}_{2_{\mathrm{ML}}} - \widehat{r}_{\mathrm{ML}}\right)^2}.$$

The practical determination of $\widehat{r}_{\mathrm{ML}}$ is achieved by using a Newton-Raphson procedure under the constraint $\widehat{r}_{\mathrm{ML}} \in [0, \widehat{a}_{1_{\mathrm{ML}}}\widehat{a}_{2_{\mathrm{ML}}}]$.[1] It is important to highlight that (3.29) also ensures that the ML estimators of a_1 and a_2 decouple from one another and r. Following the functional invariance principle [80], the ML estimators of a_1, a_2, and r are then plugged into (1.10), yielding the DoP ML estimator based on two multi-look intensity images

$$\widehat{\mathcal{P}}_{\mathrm{ML}} = \left[1 - \frac{4\left(\widehat{a}_{1_{\mathrm{ML}}}\widehat{a}_{2_{\mathrm{ML}}} - \widehat{r}_{\mathrm{ML}}\right)}{\left(\widehat{a}_{1_{\mathrm{ML}}} + \widehat{a}_{2_{\mathrm{ML}}}\right)^2}\right]^{\frac{1}{2}}. \tag{3.30}$$

We note that these results generalize those of Chatelain et al. [79], derived for $q = 1$ in an optical polarimetric imagery context, to multi-look dual-pol SAR imaging systems.

[1] The parameter $\rho = (p_1 p_2 - p_{12})/p_1 p_2 \triangleq r/a_1 a_2$ is the correlation coefficient for a BGD, and thus, it is upper bounded by 1. Moreover, we have $r = a_3^2 + a_4^2$, which makes r to be positive, and thus, we have $r \in [0, a_1 a_2]$.

3.3.2.2 *Cramer-Rao Bound*

The asymptotic variance of the estimator (3.30) is its Cramer-Rao bound. Let us consider the function $\mathcal{g} : \boldsymbol{\vartheta} \longmapsto \mathcal{g}(\boldsymbol{\vartheta}) = \mathcal{P}$. The asymptotic variance of $\widehat{\mathcal{P}}_{\mathrm{ML}}$ from (3.30) can be derived as following

$$\underset{\text{asym}}{\mathrm{Var}}\left(\widehat{\mathcal{P}}_{\mathrm{ML}}\right) = \boldsymbol{G}^T \boldsymbol{F}^{-1} \boldsymbol{G} \tag{3.31}$$

where $\boldsymbol{F}^{-1}$ is the inverse Fisher information matrix for the parameter $\boldsymbol{\vartheta}$, and $\boldsymbol{G}$ is the gradient of the function $\mathcal{g}$ given by

$$\begin{aligned} \boldsymbol{G} &= G_0 \left[\frac{a_1 a_2 - a_2^2 - 2r}{(a_1 + a_2)^2}, \frac{a_1 a_2 - a_1^2 - 2r}{(a_1 + a_2)^2}, \frac{1}{a_1 + a_2} \right]^T \\ G_0 &= \frac{2}{\left[(a_1 - a_2)^2 + 4r\right]^{\frac{1}{2}}} \,. \end{aligned} \tag{3.32}$$

The Fisher information matrix of the parameter $\boldsymbol{\vartheta}$ is defined as

$$\boldsymbol{F}(\boldsymbol{\vartheta}) = -\mathsf{E}\left[\frac{\partial^2 \ln \mathcal{L}(\widetilde{\mathbf{g}}_b; \boldsymbol{\vartheta})}{\partial \boldsymbol{\vartheta} \partial \boldsymbol{\vartheta}^T} \right]. \tag{3.33}$$

This expression gives rise to complex expectation terms, due to the presence of $\ln f_q$ in the log-likelihood function. A well-known approach to approximate such expectations is based on Monte Carlo experiments. Following this approach, the elements of the Fisher information matrix can be approximated as

$$[\boldsymbol{F}(\boldsymbol{\vartheta})]_{ij} \approx -\frac{1}{N} \sum_{k=1}^{N} \frac{\partial^2 \ln \mathcal{L}(\boldsymbol{x}_k)}{\partial \vartheta_i \partial \vartheta_j}. \tag{3.34}$$

where $\boldsymbol{x}_k$ is distributed according to a BGD, and N is the number of Monte Carlo realizations. Under mild regularity conditions, the ML estimator is asymptotically normal. Therefore, the asymptotic distribution of $\widehat{\mathcal{P}}_{\mathrm{ML}}$ from (3.30) is expressed as

$$\widehat{\mathcal{P}}_{\mathrm{ML}} \underset{\text{asym}}{\sim} \mathcal{N}\left(\mathcal{P}, \boldsymbol{G}^T \boldsymbol{F}^{-1} \boldsymbol{G}\right). \tag{3.35}$$

3.3.2.3 *Moment-Based Estimators*

The first- and second-order moments of a BGD are given in § 1.4.3. Considering (3.15) along with these moments, one can find the first and second order moments of $(\widetilde{\mathrm{g}}_0, \widetilde{\mathrm{g}}_1)^T$ as

$$m_1 = \mathsf{E}\left[\widetilde{\mathrm{g}}_0\right] = a_1 \tag{3.36}$$

$$m_2 = \mathsf{E}\left[\widetilde{\mathrm{g}}_1\right] = a_2 \tag{3.37}$$

$$m_{12} = \mathsf{E}\left[\widetilde{\mathrm{g}}_0 \widetilde{\mathrm{g}}_1\right] = \frac{r}{q} + a_1 a_2. \tag{3.38}$$

Hence, moment estimators of a_1, a_2, and r can be obtained as follows

$$\widehat{a}_{1_{\text{MoM}}} = \widehat{m}_1 = \frac{1}{n}\sum_{j=1}^{n} \widetilde{\mathrm{g}}_0\,[j] \tag{3.39}$$

$$\widehat{a}_{2_{\text{MoM}}} = \widehat{m}_2 = \frac{1}{n}\sum_{j=1}^{n} \widetilde{\mathrm{g}}_1\,[j] \tag{3.40}$$

$$\begin{aligned}\widehat{r}_{\text{MoM}} &= q\,(\widehat{m}_{12} - \widehat{m}_1\widehat{m}_2) \\ &= \frac{q}{n}\sum_{j=1}^{n} \widetilde{\mathrm{g}}_0\,[j]\,\widetilde{\mathrm{g}}_1\,[j] - q\widehat{a}_{1_{\text{MoM}}}\widehat{a}_{2_{\text{MoM}}}.\end{aligned} \tag{3.41}$$

These estimators are then plugged into (1.10), yielding the estimator of the DoP based on the moments, denoted as $\widehat{\mathcal{P}}_{\text{MoM}}$. We see that the moment estimators of a_1 and a_2 are the same as their ML estimators given in (3.28). However, the ML estimator of r, derived from (3.29), incorporates a *weighted* second-order moment compared with the MoM estimator $\widehat{r}_{\text{MoM}}$.

3.3.2.4 *Asymptotic Variance*

Considering $\boldsymbol{\vartheta} = (a_1, a_2, r)$ and the function $g : \boldsymbol{\vartheta} \longmapsto g(\boldsymbol{\vartheta}) = \mathcal{P}$, the asymptotic variance of $\widehat{\mathcal{P}}_{\text{MoM}}$ can be achieved by

$$\underset{\text{asym}}{\text{Var}}\left(\widehat{\mathcal{P}}_{\text{MoM}}\right) = \boldsymbol{G}^T \underset{\text{asym}}{\text{Var}}\left(\widehat{\boldsymbol{\vartheta}}_{\text{MoM}}\right) \boldsymbol{G} \tag{3.42}$$

where $\boldsymbol{G}$ is the gradient of the function g given by (3.32), and $\underset{\text{asym}}{\text{Var}}\left(\widehat{\boldsymbol{\vartheta}}_{\text{MoM}}\right)$ is obtained using (1.40) as

$$\underset{\text{asym}}{\text{Var}}\left(\widehat{\boldsymbol{\vartheta}}_{\text{MoM}}\right) = \frac{1}{nq}\begin{pmatrix} a_1^2 & r & 2a_1 r \\ r & a_2^2 & 2a_2 r \\ 2a_1 r & 2a_2 r & a_1^2 a_2^2 + 4a_1 a_2 r + 3r^2 \end{pmatrix}. \tag{3.43}$$

After some calculations, we obtain the asymptotic variance of $\widehat{\mathcal{P}}_{\text{MoM}}$ as

$$\begin{aligned}\underset{\text{asym}}{\text{Var}}\left(\widehat{\mathcal{P}}_{\text{MoM}}\right) =& \boldsymbol{G}^T \underset{\text{asym}}{\text{Var}}\left(\widehat{\boldsymbol{\vartheta}}_{\text{MoM}}\right) \boldsymbol{G} \\ =& \frac{(1-\mathcal{P}^2)^2(1/2+\mathcal{P}^2)}{2nq\,\mathcal{P}^2} \\ &+ \frac{16a_1a_2r}{nq(a_1+a_2)^4\,\mathcal{P}^2}\end{aligned} \tag{3.44}$$

where q is the number of looks and n is the number of samples in the estimation window. It is worth noting that this asymptotic variance of $\widehat{\mathcal{P}}_{\text{MoM}}$ does not solely depend on the DoP [in contrast to that of the coherent estimator; see (3.21)], but it also directly depends on all the intermediate parameters, i. e., a_1, a_2, and r. Moreover, this asymptotic variance is always greater than that of the coherent case given by (3.21).

These results generalize those of Roche et al. [81], derived for $q = 1$, using a different method in an optical polarimetric imagery context, to multi-look dual-pol SAR imaging systems. The performance of both ML and MoM DoP estimators are studied in detail in Chapter 5, using linear, hybrid and compact dual-pol SAR data, over various terrain types such as urban, vegetation, and ocean.

3.4 A GENERALIZED DEFINITION OF THE DOP

Concentrating on different dual-pol radar systems, we introduce a generalized definition of the DoP in hybrid, compact, and alternating dual-pol modes. Let us consider a dual-pol scattering vector $\boldsymbol{k}_i$ with a generic transmit polarization i. The dual-pol[1] 2×2 covariance matrix $\boldsymbol{J}_i$ is straightforwardly defined from the scattering vector $\boldsymbol{k}_i$ as

$$\boldsymbol{J}_i = \left\langle \boldsymbol{k}_i \boldsymbol{k}_i^{\dagger} \right\rangle . \tag{3.45}$$

where $\boldsymbol{k}_i \in \left\{ \boldsymbol{k}_{\text{DP1}}, \boldsymbol{k}_{\text{DP2}}, \boldsymbol{k}_{\text{DP3}}, \boldsymbol{k}_{\text{CL-pol}}, \boldsymbol{k}_{\pi/4}, \boldsymbol{k}_{\text{DCP}} \right\}$. The Stokes vector for a generic transmit polarization i, and linear receive polarizations, is given by

$$\mathbf{g}_i = \begin{pmatrix} \left\langle |E_{i\text{H}}|^2 + |E_{i\text{V}}|^2 \right\rangle \\ \left\langle |E_{i\text{H}}|^2 - |E_{i\text{V}}|^2 \right\rangle \\ 2\Re \left\langle E_{i\text{H}} E_{i\text{V}}^* \right\rangle \\ -2\Im \left\langle E_{i\text{H}} E_{i\text{V}}^* \right\rangle \end{pmatrix} . \tag{3.46}$$

The transmit polarization i for a traditional dual-pol radar is either H or V, for the hybrid (CL-pol) mode is either left- or right-circular (L and R), and for the $\pi/4$ compact mode is H+V oriented at 45 degrees. Considering the above definitions, we are naturally led to introduce a generalized definition of the DoP $\mathcal{P}_i$ and DoD $\overline{\mathcal{P}}_i$ in linear, hybrid and compact dual-pol SAR as

$$\overline{\mathcal{P}}_i = 1 - \mathcal{P}_i \tag{3.47}$$

$$\mathcal{P}_i = \frac{\sqrt{\mathrm{g}_{i1}^2 + \mathrm{g}_{i2}^2 + \mathrm{g}_{i3}^2}}{\mathrm{g}_{i0}} \tag{3.48}$$

$$= \left(1 - 4 \frac{|\boldsymbol{J}_i|}{(\mathrm{tr}\boldsymbol{J}_i)^2} \right)^{\frac{1}{2}} \tag{3.49}$$

where $|\boldsymbol{J}_i|$ and $\mathrm{tr}\boldsymbol{J}_i$ are the determinant and trace of $\boldsymbol{J}_i$ respectively. In the rest of the present manuscript, the term *dual-pol DoP/DoD* refers to the above definitions. In Chapter 5, we study in detail the performance of the DoP in different dual-pol SAR modes for maritime monitoring applications such as vessel detection and oil-spill recognition.

[1] In the rest of the present manuscript, unless specifically stated, the general term *dual-pol* refers to both classical (linear), and emerging (hybrid/compact) dual-pol SAR modes.

3.5 STATISTICAL ANALYSIS OF LINEAR, HYBRID, AND CIRCULAR FULL-POL INTENSITY IMAGES

As mentioned in § 1.2, the linear full-pol complex scattering vector is represented by

$$\boldsymbol{k}_{\mathrm{FP}} = \begin{pmatrix} S_{\mathrm{HH}} \\ S_{\mathrm{HV}} \\ S_{\mathrm{VH}} \\ S_{\mathrm{VV}} \end{pmatrix}. \tag{3.50}$$

Let us denote the complex scattering vectors $\boldsymbol{k}_{\mathrm{FP}}^{\mathrm{Hy}}$ and $\boldsymbol{k}_{\mathrm{FP}}^{\mathrm{Cr}}$ for hybrid and circular full-pol systems as $\boldsymbol{k}_{\mathrm{FP}}^{\mathrm{Hy}} = (S_{\mathrm{RH}}, S_{\mathrm{RV}}, S_{\mathrm{LH}}, S_{\mathrm{LV}})^T$ and $\boldsymbol{k}_{\mathrm{FP}}^{\mathrm{Cr}} = (S_{\mathrm{RR}}, S_{\mathrm{RL}}, S_{\mathrm{LR}}, S_{\mathrm{LL}})^T$, respectively. Coherent collection of the linear full-pol data, mathematically allows synthesis of any combination of transmit and receive polarizations. Hence, the hybrid and circular full-pol scattering vectors can be expressed in terms of the linear components as

$$\boldsymbol{k}_{\mathrm{FP}}^{\mathrm{Hy}} = \begin{pmatrix} S_{\mathrm{RH}} \\ S_{\mathrm{RV}} \\ S_{\mathrm{LH}} \\ S_{\mathrm{LV}} \end{pmatrix} = \frac{1}{\sqrt{2}} \begin{pmatrix} S_{\mathrm{HH}} - iS_{\mathrm{HV}} \\ -iS_{\mathrm{VV}} + S_{\mathrm{VH}} \\ S_{\mathrm{HH}} + iS_{\mathrm{HV}} \\ iS_{\mathrm{VV}} + S_{\mathrm{VH}} \end{pmatrix} \tag{3.51}$$

$$\boldsymbol{k}_{\mathrm{FP}}^{\mathrm{Cr}} = \begin{pmatrix} S_{\mathrm{RR}} \\ S_{\mathrm{RL}} \\ S_{\mathrm{LR}} \\ S_{\mathrm{LL}} \end{pmatrix} = \frac{1}{2} \begin{pmatrix} S_{\mathrm{HH}} - S_{\mathrm{VV}} + i\left[S_{\mathrm{HV}} + S_{\mathrm{VH}}\right] \\ i\left[S_{\mathrm{HH}} + S_{\mathrm{VV}}\right] + S_{\mathrm{HV}} - S_{\mathrm{VH}} \\ i\left[S_{\mathrm{VV}} + S_{\mathrm{HH}}\right] + S_{\mathrm{VH}} - S_{\mathrm{HV}} \\ S_{\mathrm{VV}} - S_{\mathrm{HH}} + i\left[S_{\mathrm{VH}} + S_{\mathrm{HV}}\right] \end{pmatrix} \tag{3.52}$$

For a reciprocal target matrix, in the monostatic backscattering case, the scattering reciprocity constrains the Sinclair scattering matrix to be symmetrical [54]. Therefore, we have $S_{\mathrm{HV}} = S_{\mathrm{VH}}$, and thus

$$\boldsymbol{k}_{\mathrm{FP}}^{\mathrm{sr}} = \begin{pmatrix} S_{\mathrm{HH}} \\ \sqrt{2}S_{\mathrm{HV/VH}} \\ S_{\mathrm{VV}} \end{pmatrix} \tag{3.53}$$

$$\boldsymbol{k}_{\mathrm{FP}}^{\mathrm{Cr\text{-}sr}} = \begin{pmatrix} S_{\mathrm{RR}} \\ \sqrt{2}S_{\mathrm{RL/LR}} \\ S_{\mathrm{LL}} \end{pmatrix} \tag{3.54}$$

where the factor $\sqrt{2}$ ensures the total power invariance.

It is well-known that the elements of the classical (linear) full-pol complex scattering vector follow a complex Gaussian distribution.

Based on (3.51) and (3.52), the elements of the hybrid and circular scattering vectors are linear combinations of the classical full-pol components. Therefore, it is straightforward[1] to consider that the hybrid and circular scattering vectors also follow a multivariate complex Gaussian distribution. For the purpose of generality, we adopt a convenient notation to represent all the above full-pol scattering vectors as following

$$\boldsymbol{k}_4 = \begin{pmatrix} S_1 \\ S_2 \\ S_3 \\ S_4 \end{pmatrix} \tag{3.55}$$

where $S_1, \ldots, S_4$ denote any linear combinations of S_{HH}, S_{HV}, S_{VH}, and S_{VV}. Therefore, $\boldsymbol{k}_4$ for particular cases of linear, hybrid, and circular reduces to $\boldsymbol{k}_{\mathrm{FP}}$, $\boldsymbol{k}_{\mathrm{FP}}^{\mathrm{Hy}}$, and $\boldsymbol{k}_{\mathrm{FP}}^{\mathrm{Cr}}$, respectively. Under the usual assumption of fully developed speckle, $\boldsymbol{k}_4$ is distributed according to a complex circular Gaussian distribution whose PDF is

$$p_{\mathrm{G}}\left(\boldsymbol{k}_4\right) = \frac{1}{\pi^4 \left|\boldsymbol{C}_{4\times4}\right|} \exp\left(-\boldsymbol{k}_4{}^{\dagger} \boldsymbol{C}_{4\times4}^{-1} \boldsymbol{k}_4\right) \tag{3.56}$$

where $\boldsymbol{C}_{4\times4} = \mathbb{E}\left[\boldsymbol{k}_4 \boldsymbol{k}_4{}^{\dagger}\right]$ is the 4×4 Hermitian complex covariance matrix, the superscript † denotes the complex conjugate transpose, and $\left|\boldsymbol{C}_{4\times4}\right|$ is the determinant of $\boldsymbol{C}_{4\times4}$. Following the same line of proof as in § 3.1, we find that the joint distribution of the delivered multilook intensity images, i. e., $\boldsymbol{\mathcal{S}} = \left(\langle|S_1|^2\rangle, \langle|S_2|^2\rangle, \langle|S_3|^2\rangle, \langle|S_4|^2\rangle\right)^T$ is an MGD as follows

$$L_{\boldsymbol{\mathcal{S}}}(\boldsymbol{\theta}) = \frac{1}{P(\boldsymbol{\theta})^q} \tag{3.57}$$

$$\begin{aligned} P(\boldsymbol{\theta}) = 1 &+ \sum_{i=1}^{4} p_i \theta_i \\ &+ \sum_{1\le i<j\le 4} p_{ij} \theta_i \theta_j \\ &+ \sum_{1\le i<j<k\le 4} p_{ijk} \theta_i \theta_j \theta_k \\ &+ \sum_{1\le i<j<k<l\le 4} p_{ijkl} \theta_i \theta_j \theta_k \theta_l \end{aligned} \tag{3.58}$$

with

$$\begin{aligned} p_i &= C_{ii} \\ p_{ij} &= \left|\boldsymbol{C}_{ij}\right| \\ p_{ijk} &= \left|\boldsymbol{C}_{ijk}\right| \\ p_{ijkl} &= \left|\boldsymbol{C}_{ijkl}\right| \end{aligned}$$

[1] The family of normal distributions is closed under linear transformations.

where C_{ii} denotes the diagonal elements of the covariance matrix $\boldsymbol{C}_{4\times4}$, $|\cdot|$ represents the determinant, and

$$\boldsymbol{C}_{ij} = \begin{pmatrix} C_{ii} & C_{ij} \\ C_{ji} & C_{jj} \end{pmatrix}$$
$$\boldsymbol{C}_{ijk} = \begin{pmatrix} C_{ii} & C_{ij} & C_{ik} \\ C_{ji} & C_{jj} & C_{jk} \\ C_{ki} & C_{kj} & C_{kk} \end{pmatrix}$$
$$\boldsymbol{C}_{ijkl} = \boldsymbol{C}_{4\times4}.$$

Interestingly, we see that the joint distribution of multilook intensity images from linear, hybrid, and circular full-pol SAR modes are MGDs, parametrized by the elements of the corresponding 4×4 covariance matrix. This conclusion opens the doors for extending the statistical methods, which were initially derived for linear full-pol data, to hybrid and circular full-pol data. On the other hand, it makes clear that in the case of dual-pol data, since the information content of the dual-pol covariance matrices are not equivalent, different dual-pol modes can lead to different results. We further study the dual-pol distributions in what follows.

3.6 Marginal distributions of linear, hybrid, and circular dual-pol intensity images

Particular cases of the derived full-pol joint distribution, for three and two polarimetric SAR intensity images, are of great importance. The dimension of three corresponds to a reciprocal medium [see (3.53) and (3.54)]. The dimension of two can correspond to linear, hybrid, compact, and circular dual-pol modes [see (2.1– 2.4)]. Based on the characteristics of MGDs, the marginal distributions for three and two multilook intensity images are also MGDs. Thus, one can set the corresponding θ_i in (3.57) to zero, in order to obtain the related polynomials leading to the marginal PDFs.

For the purpose of this study, we concentrate on the dual-pol (two dimensional) case. Without loss of generality, let us consider the following pair of intensity images

$$(\mathcal{S}_i, \mathcal{S}_j)_{1\leq i\neq j\leq 4} \in \left\{ \langle |S_1|^2 \rangle, \langle |S_2|^2 \rangle, \langle |S_3|^2 \rangle, \langle |S_4|^2 \rangle \right\}. \tag{3.59}$$

In order to derive the corresponding dual-pol PDFs, we set $\theta_{k\neq i,j}$ and $\theta_{l\neq i,j}$ to zero in (3.57) and obtain the following polynomial

$$P(\boldsymbol{\theta}) = 1 + p_i\theta_i + p_j\theta_j + p_{ij}\theta_i\theta_j \tag{3.60}$$

with $p_i = C_{ii}$, $p_j = C_{jj}$, and $p_{ij} = C_{ii}C_{jj} - C_{ji}C_{ij}$. Therefore, based on § 1.4.3, the distribution of the multilook intensity vector $\underline{\boldsymbol{\mathcal{S}}} = (\mathcal{S}_i, \mathcal{S}_j)^T$ is a BGD with the following PDF

$$p_{\text{BGD}}(\underline{\boldsymbol{\mathcal{S}}}) = \exp\left(-\frac{p_j\mathcal{S}_i + p_i\mathcal{S}_j}{p_{ij}}\right)\frac{\mathcal{S}_i^{q-1}\mathcal{S}_j^{q-1}}{p_{ij}^q\Gamma(q)} f_q\left(c\mathcal{S}_i\mathcal{S}_j\right)\mathbb{I}_{\mathbb{R}_+^2}\left(\underline{\boldsymbol{\mathcal{S}}}\right) \quad (3.61)$$

where $c = \left(p_ip_j - p_{ij}\right)/p_{ij}^2$ and $f_q(z) = \sum_{j=0}^{\infty} z^j/\Gamma(q+j)j!$ is related to confluent hypergeometric, and modified Bessel functions [72, p. 374]. Therefore, the distribution of any pair of multilook intensity images from linear, hybrid, and circular full-pol modes [see (3.50), (3.51), and (3.52)] is a BGD, parametrized by the corresponding elements of the 2×2 covariance matrix through (p_i, p_j, p_{ij}).

At this point, let us consider a dual-pol scattering vector $\underline{\boldsymbol{k}}$ as

$$\underline{\boldsymbol{k}} = \begin{pmatrix} k_1 \\ k_2 \end{pmatrix} \quad (3.62)$$

$$\underline{\boldsymbol{k}} \in \left\{\boldsymbol{k}_{\text{DP1}}, \boldsymbol{k}_{\text{DP2}}, \boldsymbol{k}_{\text{DP3}}, \boldsymbol{k}_{\text{CL-pol}}, \boldsymbol{k}_{\pi/4}, \boldsymbol{k}_{\text{DCP}}\right\}. \quad (3.63)$$

By setting $\underline{\boldsymbol{\mathcal{S}}} = \left(\langle|k_1|^2\rangle, \langle|k_2|^2\rangle\right)^T$, and following a similar approach, we can conclude that the PDF of a pair of multilook intensity images delivered in linear, hybrid, compact, and circular dual-pol modes is a BGD given by (3.61), parametrized by the elements of the corresponding dual-pol covariance matrix.

The distributions obtained in this chapter are of great interest in a variety of dual- and full-pol SAR detection and classification applications. In particular, a closed form PDF was derived for dual-pol modes, based on which different statistical methods, such as ML estimations, can be developed. In the next chapter, we concentrate on the detection and classification tasks in the context of maritime monitoring and surveillance.

4

COHERENT DUAL-POL DOP: MARITIME MONITORING & SURVEILLANCE

About 100,000 birds may have died in the Erika spill disaster near the coast of Brittany

—Bretagne vivante
Jan. 2000

MARITIME monitoring and surveillance is of great environmental and economical importance; it directly contributes to improve public safety and environmental protection. In particular, effective detection and monitoring of oil spills, ships, and oil-rigs are major concerns in this context. Oil spills are highly damaging to the environment and pose serious threats to the ecology, marine wildlife, and the human food chain. Oil pollution comes partly from frequent illegal ship discharges, and partly from large ship and oil-rig accidents. Some famous examples of major oil spills are the Amoco Cadiz spill (in 1978, coast of Brittany, France, with ~68.7 million gallons of leaked oil), the Ixtoc I well disaster (in 1979, Gulf of Mexico, Mexico, with ~140 million gallons of leaked oil), and more recently the Prestige tanker spill (in 2002, northwest coast of Spain), and the British Petroleum (BP) Deepwater Horizon disaster (in 2010, northern Gulf of Mexico, USA). The Deepwater Horizon oil spill, occurred on April 20, 2010, is by far the worst oil spill in US history, with about 200 million gallons [82, 83] of leaked oil along the coastal areas of Louisiana, Mississippi, Alabama, and Florida. Unfortunately, oil spills occur very often in spite of their tremendous danger for marine and wildlife habitats. Table 4.1 provides a very short list of some famous oil spills occurred around the world. An important step in oil spill response is to assess the character and extent of oil spilled on the water. This information is used to prioritize the oil spill response and to direct cleanup activities. This task is addressed in

Increasing global demand for energy inexorably increases the risk of oil spills from both oil sources and transporting tankers.

TABLE 4.1. A short list of some famous oil spills.

Name	Location	Date	Leaked Oil*
Deepwater Horizon	Gulf of Mexico, USA	2010	200
Hurricane Katrina	Gulf of Mexico	2005	7.98
Prestige	Galicia, Spain	2002	20
Jessica	Galapagos, Ecuador	2001	0.18
Petrobras	Guanabara Bay, Brazil	2000	0.350
Erika	Brittany, France	1999	3.1
Sea Empress	South Wales, UK	1996	21.3
Haven	Genoa, Italy	1991	42.0
Exxon Valdez	Alaska	1989	10.8
Odyssey	Nova Scotia, Canada	1988	43.1
Ixtoc I	Gulf of Mexico, Mexico	1979	140
Amoco Cadiz	Brittany, France	1978	68.7
Othello	Tralhavet Bay, Sweden	1970	18.2

* in million US gallons (1 US gallon = 3.785 liters)

detail in Section 4.1 by analyzing the DoP in (coherent) dual-pol SAR imagery.

Wide-area identification of oil and gas platforms is also of critical importance. After hurricanes and storms, for example, it allows the reconnaissance flights to be carried out much more efficiently resulting in significant savings and increased safety. A related application is the detection of ships, boats, and cargoes, with extensive utilization in vessel traffic management, commercial fishery, public safety, and environmental protection. We concentrate on the detection of the buoys, ships, and oil-rigs using the DoP in (coherent) linear and hybrid/compact dual-pol SAR modes in Section 4.2.

4.1 OIL SPILL DETECTION AND IDENTIFICATION

Monitoring and detection of oil spills using SAR data have received a considerable attention, notably due to the wide area coverage, and day and night all-weather capabilities of SAR systems. The influence of surface oil on ocean backscatter has been extensively studied using radar data in the publications of Krishen [84], Singh et al. [85], Alpers and Hühnerfuss [86], Wismann et al. [87], Fingas and Brown [88], and others. Oil spills have a different constitution than water; they dampen the small-scale ocean surface waves, called Bragg waves [89], and cause weaker radar backscatter signatures [86]. As a result, oil

regions on the SAR images appear as dark patches within the ocean clutter (see Appendix A for more information).

Many operational oil detection methods are based on the image intensity differences between the oil spill and surroundings using a single polarization channel (see for example the publications of Brekke and Solberg [90], Mercier and Girard-Ardhuin [91], and Solberg et al. [92]). However, single polarization methods do not make the best of oil/water scattering properties, and thus, oil-sea contrast is not optimum if only one pair of transmitting-receiving antenna polarization is used. There exists a limited number of studies on the use of subtle polarimetric discriminators for enhancing oil spill detection. A preliminary study on the use of the anisotropy parameter, related to the Cloude-Pottier decomposition [93], to improve oil spill detection has been reported by Fortuny-Guasch [94]. The utility of entropy, anisotropy, and average alpha of the Cloude-Pottier decomposition, for the detection of ocean and slick features, have been further investigated in the recent publications of Schuler et al. [95] and Migliaccio et al. [96]. Following the same line of study, NASA/JPL researchers have newly proposed the Shannon entropy decomposition [97], for the characterization of the oil spills in the Deepwater Horizon oil spill campaign [27]. However, such parameters can only be calculated using full polarimetric SAR data. In the framework of dual-pol SAR, recent publications have demonstrated the potential of the Co-Polarized Phase Difference (CPD), i. e., $\varphi_{HH} - \varphi_{VV}$, to improve the detection performance of oil spills [98, 99]. However, the CPD is not a versatile discriminator among all dual-pol SAR modes, i. e., it is not accessible in other dual-pol modes such as HH-HV and VH-VV. In the latter modes, the accessible Cross-Polarized Phase Difference (XPD) is also not of use since it is uniformly distributed, independent of the incidence angle, frequency, and roughness, for natural targets [100, 101].

In this section, we demonstrate the potential of the DoP/DoD to enhance the contrast of oil spills against the surroundings in different (coherent) dual-pol SAR modes. In particular, the depolarization signatures of oil spills are studied for different incidence angles and polarizations using Deepwater Horizon polarimetric data, acquired on June 23, 2010, by NASA/JPL UAVSAR system. Figure 2.7 shows a visible image of the spill area acquired by MODIS sensor on board the NASA Terra satellite. In this figure, the black cross shows the location of the Deepwater Horizon oil-rig, the oil spill appears in gray color, and the UAVSAR acquisition flight paths are shown as blue and red boxes. The green (dashed) box shows the study areas (marked as A and B) used throughout this study. The UAVSAR data sets are acquired in L-band quad-pol mode with incidence angle ranging from 25 to 65 degrees (near- to far-range). The wind speed was also measured by a directional buoy as $\sim$ 2.5–5.0 ms^{-1}; such wind speeds produce

The incidence angle is the angle between the radar beam and the vertical to the ground surface; it increases moving across the swath from near to far range.

good sea states for SAR oil-spill detection.[1] The Pauli RGB images of the oil spill study regions A and B are shown in Fig. 2.8. These Pauli images are derived from quad-pol data and can be considered as a reference in comparing different dual-pol results. We note that, around an incidence angle of 25°, strong specular scattering is dominant, and thus, not much information characterizing oil and water is provided at this angle. Figures 4.1 and 4.2 show the maps of the degree of depolarization $\overline{\mathcal{P}}$ (dB) in linear and hybrid/compact dual-pol SAR modes for study areas A and B, respectively. These depolarization maps suggest that all dual-pol modes discriminate water and oil for most of the incidence angle range. However, the contrast between oil and water is better seen in HH-VV and hybrid/compact dual-pol modes compared to the other modes. We note that HH-HV mode demonstrates an exclusive behavior; the oil-water depolarization contrast in HH-HV mode decreases with the incidence angle whereas it increases in other dual-pol modes. Therefore, the oil-water depolarization contrast in HH-HV mode is higher for steep incidence angles whereas in other dual-pol modes, it is higher for shallow incidence angles.

In the near range, the viewing geometry is referred to as being steep, relative to the far range, where the viewing geometry is shallow.

To further study this matter, we plot the depolarization profiles of the homogeneous regions of oil (oil 1–6) and ocean (ocean 1–2), covering all the incidence angle range, as shown in Figs 4.3 and 4.4. These depolarization profiles clearly show that the oil depolarization increases with incidence angle in all dual-pol modes. However, except in HH-HV mode, the depolarization of the water in shallow incidence angles becomes less sensitive to the change of the incidence angle, and almost constant. These results suggest that, in steep incidence angles, water depolarizes the incident wave more than oil whereas oil has a greater degree of depolarization than water in shallow incidence angles. The transition incidence angle is around 40–45 degrees.

The oil-ocean depolarization ratio, defined as $10\log \overline{\mathcal{P}}_{\text{Oil}} / \overline{\mathcal{P}}_{\text{Ocean}}$ (dB), can provide us with more information for evaluating the performance of different dual-pol modes in distinguishing oil from water. Figure 4.5 shows the depolarization ratio (dB) versus the incidence angle (deg.), in different hybrid/compact and linear dual-pol modes, calculated using oil 1–6 and ocean 1–2 regions of study areas A and B. In these graphs, the further the depolarization ratio (dB) from zero, the better is the oil-water depolarization contrast. The same behavior is observed for both study areas A and B; HH-VV mode outperforms other modes in distinguishing oil from water in shallower incidence angles whereas in steeper incident angles HH-HV outperforms other modes. The detection results from hybrid/compact dual-pol modes (RH-RV and 45°H-45°V) are close to HH-VV. As noticed before, the clear water depolarizes the incident wave more than oil (oil-water depolarization ratio < 0) for steep incidence angles, and less than oil (oil-water depolarization ratio > 0) for shallow incidence angles (greater than

[1] See Appendix A.

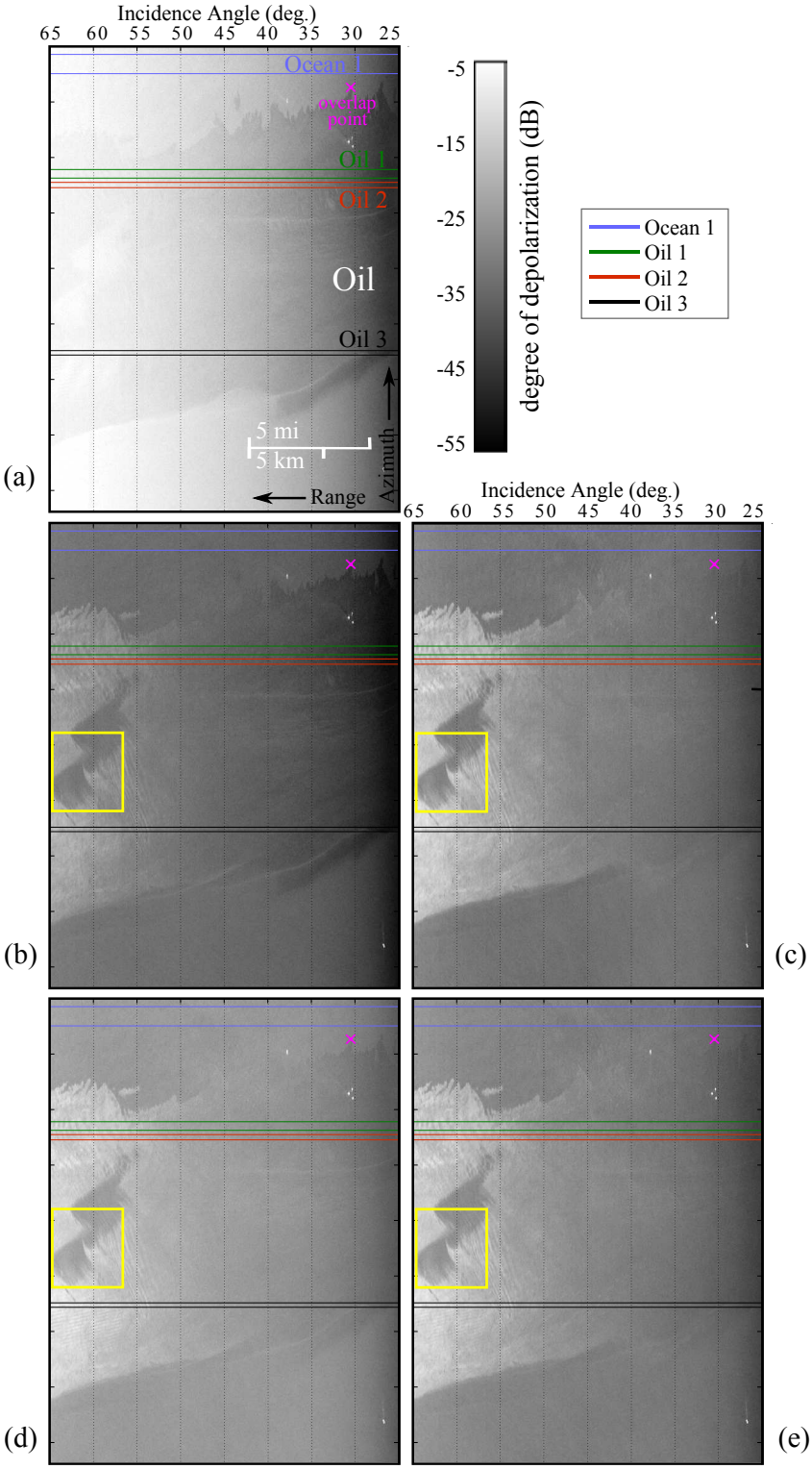

FIG. 4.1. Maps of the degree of depolarization $\overline{\mathcal{P}}$ (dB). (a) HH-HV. (b) VH-VV. (c) HH-VV. (d) RH-RV. (e) 45°H-45°V. The outlined regions of oil (oil 1–3) and ocean 1 are used in the study of the oil spill detection (Fig. 4.3). The region in the yellow box is further studied in Fig. 4.6. The pink cross marks an overlap point with Fig. 4.2. The image is 3155 pixels in range by 4371 in azimuth. A sliding window covering 7×7 pixels is used.

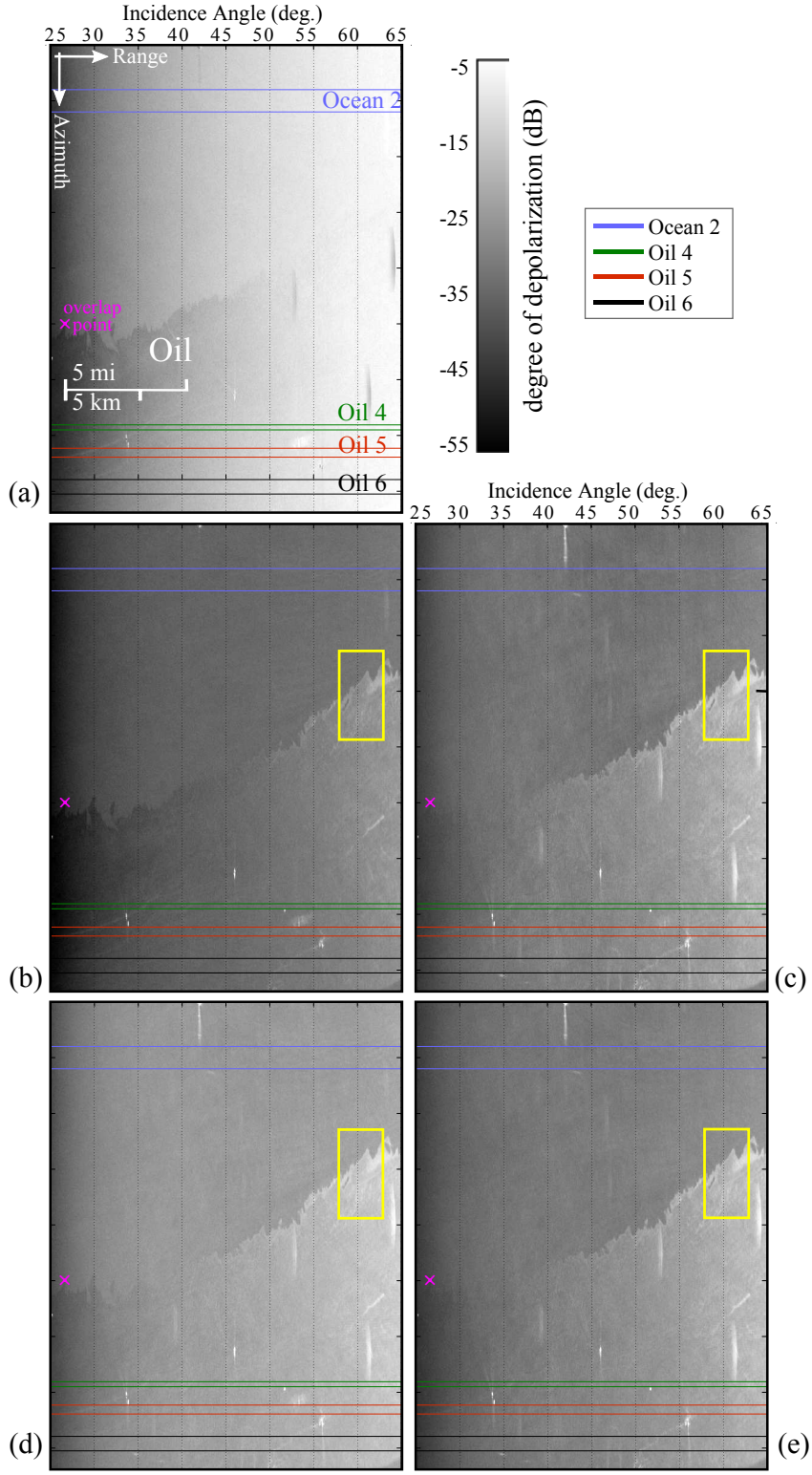

FIG. 4.2. Maps of the degree of depolarization $\overline{\mathcal{P}}$ (dB). (a) HH-HV. (b) VH-VV. (c) HH-VV. (d) RH-RV. (e) 45°H-45°V. The outlined regions of oil (oil 4–6) and ocean 2 are used in the study of the oil spill detection (Fig. 4.4). The region in the yellow box is further studied in Fig. 4.7. The pink cross marks an overlap point with Fig. 4.1. The image is 3151 pixels in range by 4201 in azimuth. A sliding window covering 7×7 pixels is used.

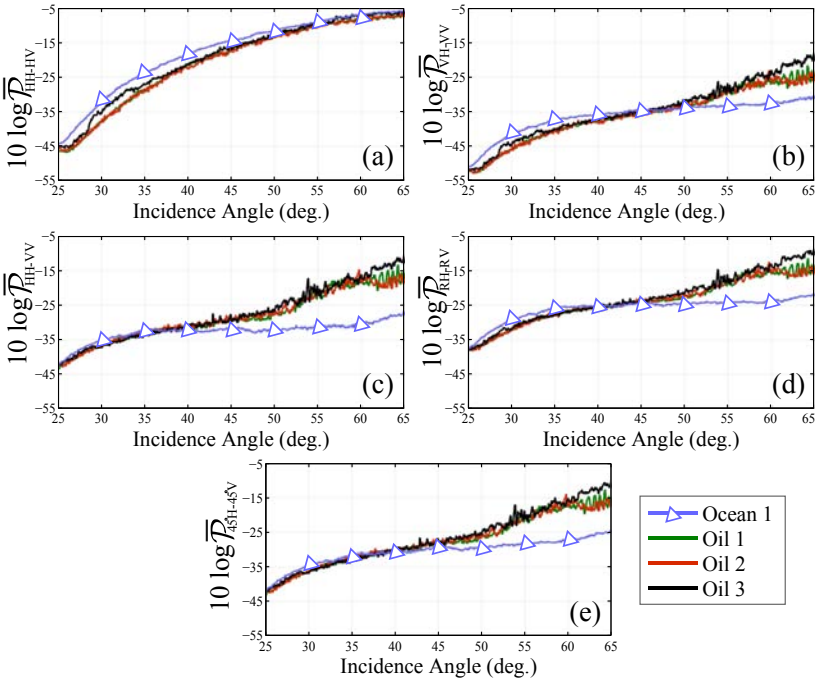

FIG. 4.3. Depolarization $\overline{\mathcal{P}}$ (dB) versus incidence angle (deg.) for ocean and oil regions (data set A) in different hybrid/compact and linear dual-pol modes. (a) HH-HV. (b) VH-VV. (c) HH-VV. (d) RH-RV. (e) 45°H-45°V. Regions are shown in Fig. 4.1.

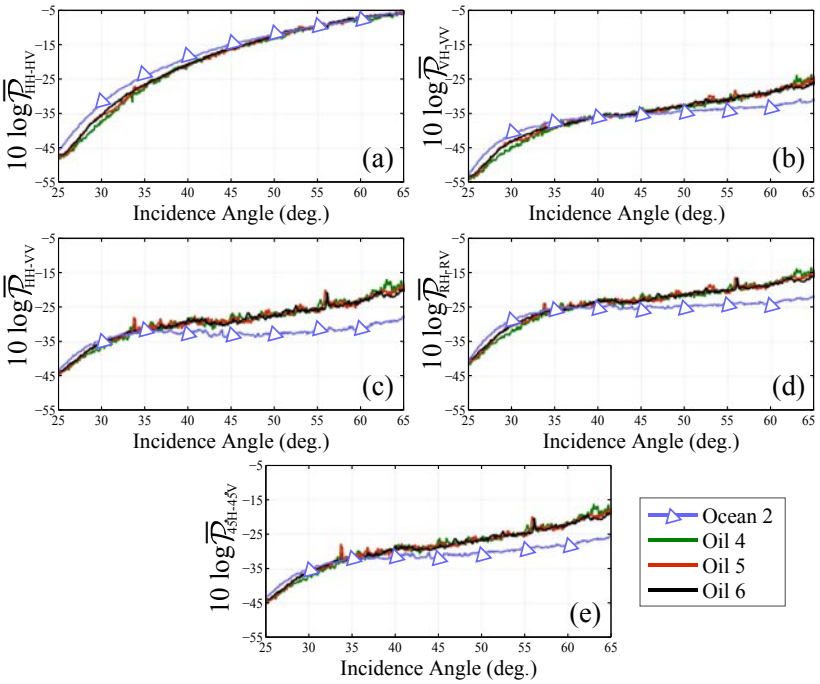

FIG. 4.4. Depolarization $\overline{\mathcal{P}}$ (dB) versus incidence angle (deg.) for ocean and oil regions (data set B) in different hybrid/compact and linear dual-pol modes. (a) HH-HV. (b) VH-VV. (c) HH-VV. (d) RH-RV. (e) 45°H-45°V. Regions are shown in Fig. 4.2.

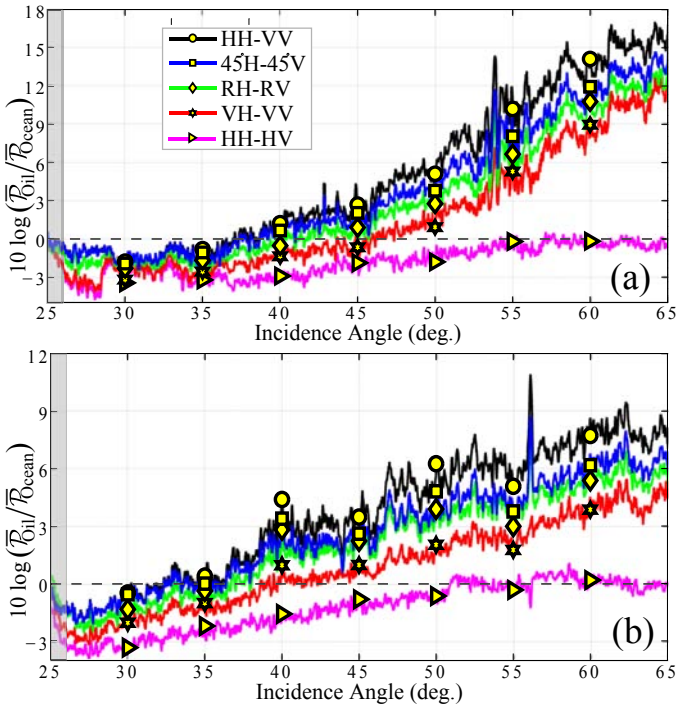

FIG. 4.5. Oil-ocean depolarization ratio (dB) versus incidence angle (deg.) for different hybrid/compact and linear dual-pol modes. (a) UAVSAR data set A. (b) UAVSAR data set B. The further the depolarization ratio is from zero, the better the oil-water depolarization contrast. Regions are shown in Fig. 4.1 and 4.2. The gray shaded area indicates the presence of strong specular scattering.

40–45°). We note that, around an incidence angle of 25°, since strong specular scattering is dominant, not much information is available for characterizing oil and water; hence, an oil-water depolarization ratio close to zero (dB) is observed around 25°(gray shaded area in Fig. 4.5).

Identifying the color, structure, and consistency of oil on water can help to determine the oil type, the amount of time it has been on the water, and other information, critical to improve the oil recovery process. Moreover, the low noise floor of UAVSAR provides a unique capability to assess backscatter information at levels not available with other radars (see Appendix B). A useful job aid has been recently published by NOAA for open water oil spill identification based on aerial (optical) observations [102]. According to NOAA publications, the thinnest possible oil layer is called *sheen* which dampens out the surface waves and gives the water a reflective appearance. Thicker oil layers are respectively called *rainbow*, *metallic*, *transitional*, and *dark oil*. Figures 4.6 and 4.7 show the depolarization maps of two test areas from the Deepwater Horizon oil spill where different interesting oil structures are present. As expected, the maximum depolarization contrast between dark oil and clear water is seen in HH-VV mode. In each figure, three regions of interest (R1, R2 and R3) are outlined. Using these depolarization maps, we can clearly recognize the oil

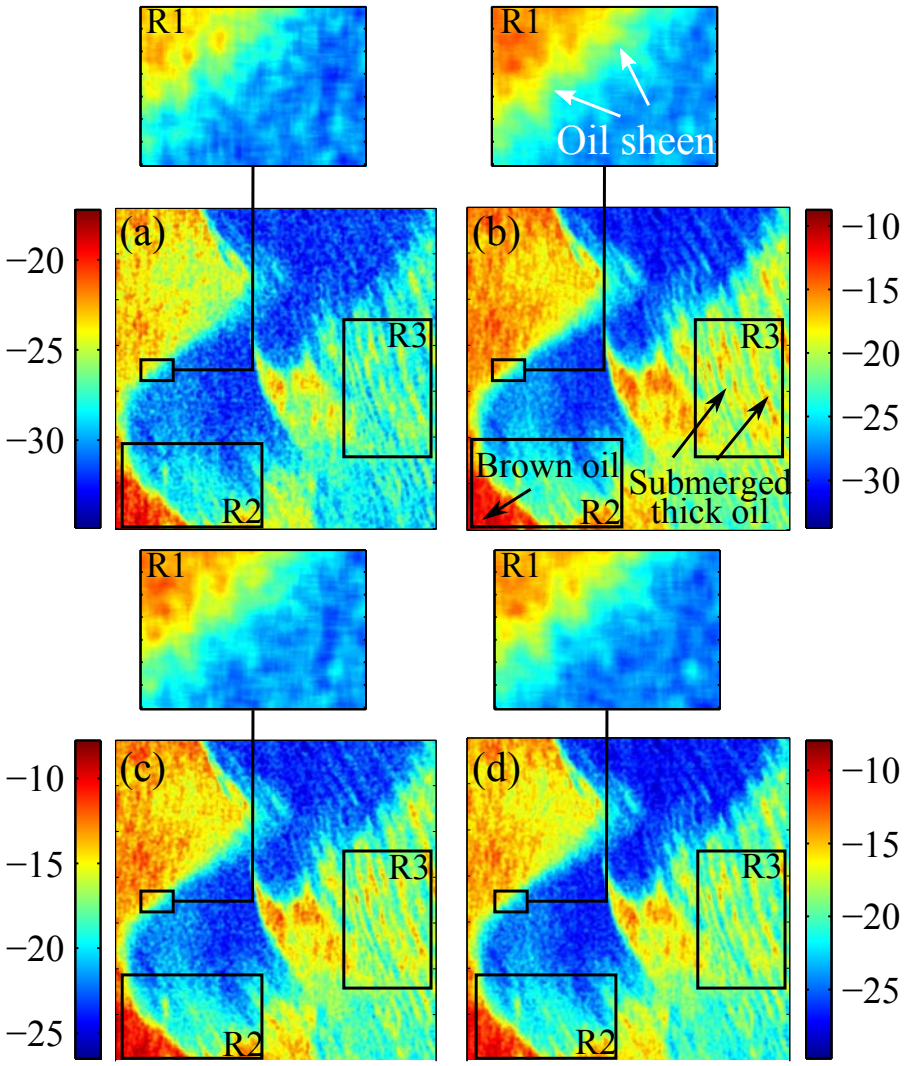

FIG. 4.6. Oil slick property/type recognition using the degree of depolarization $\overline{\mathcal{P}}$ (dB) in dual-pol SAR. (a) VH-VV. (b) HH-VV. (c) RH-RV. (d) 45°H-45°V. The region is a subset of UAVSAR data set A outlined in Fig. 4.1; windward side of the main slick ∼26 km SW of the rig site.

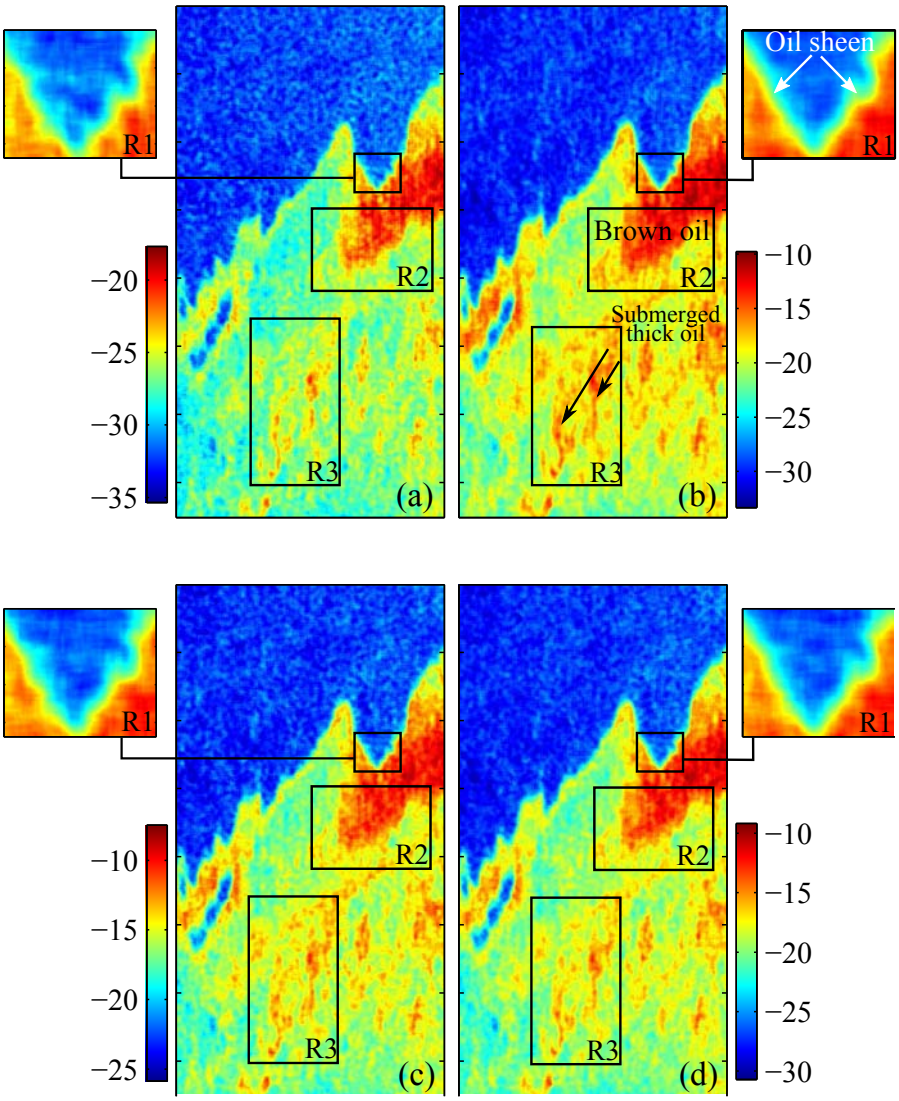

FIG. 4.7. Oil slick property/type recognition using the degree of depolarization $\overline{\mathcal{P}}$ (dB) in dual-pol SAR. (a) VH-VV. (b) HH-VV. (c) RH-RV. (d) 45°H-45°V. The region is a subset of UAVSAR data set B outlined in Fig. 4.2; leeward side of the main slick ∼31 km NNW of the rig site.

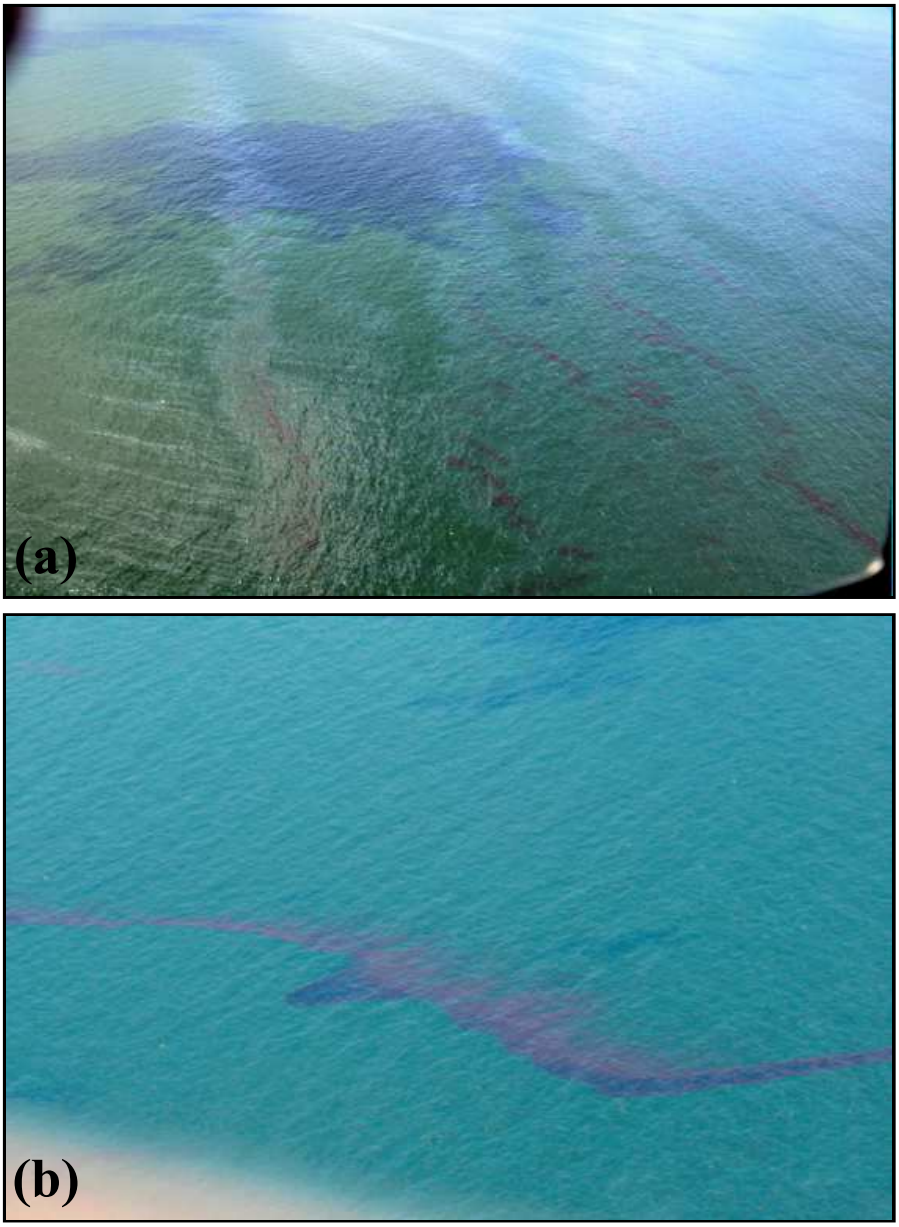

FIG. 4.8. Aerial photographs of Deepwater Horizon oil-spill, Gulf of Mexico. (a) NOAA RAT-Helo photograph showing oil features in R3 region of Fig. 4.6 (b) NOAA EPA/ASPECT photograph showing oil features in R3 region of Fig. 4.7. Photographs are taken on June 23, 2010.

*Interested readers are invited to see [103–105] for more details on such wind-aligned oil features formed by Langmuir circulations [106].

sheens along the edges (in R1 region), the dark oil patches (in R2 region), and also the narrow bands of oil* (in R3 region) revealing the wind direction. Figure 4.8 shows aerial photographs of oil-spill features present in R3 regions. Good agreement between aerial photographs and depolarization maps are seen. These results demonstrate that our approach can be used not only to discriminate oil from clean water but also to classify oil within a slick.

4.1.1 *Comparison of Dual-Pol DoP with Co-Pol Phase Difference*

The CPD has been widely acknowledged as an important quantity providing useful information in a variety of applications, notably employed in terrain and land-use classification [78, 101, 107–110]. Recent publications have also demonstrated the potential of the CPD to improve the detection of oil spills [98, 99]. The co-pol and cross-pol phase differences (CPD, XPD) are respectively defined as $\varphi_c = \varphi_{VV} - \varphi_{HH}$, and $\varphi_x = \varphi_{HV} - \varphi_{HH} = \varphi_{VH} - \varphi_{HH}$. It is well understood that the

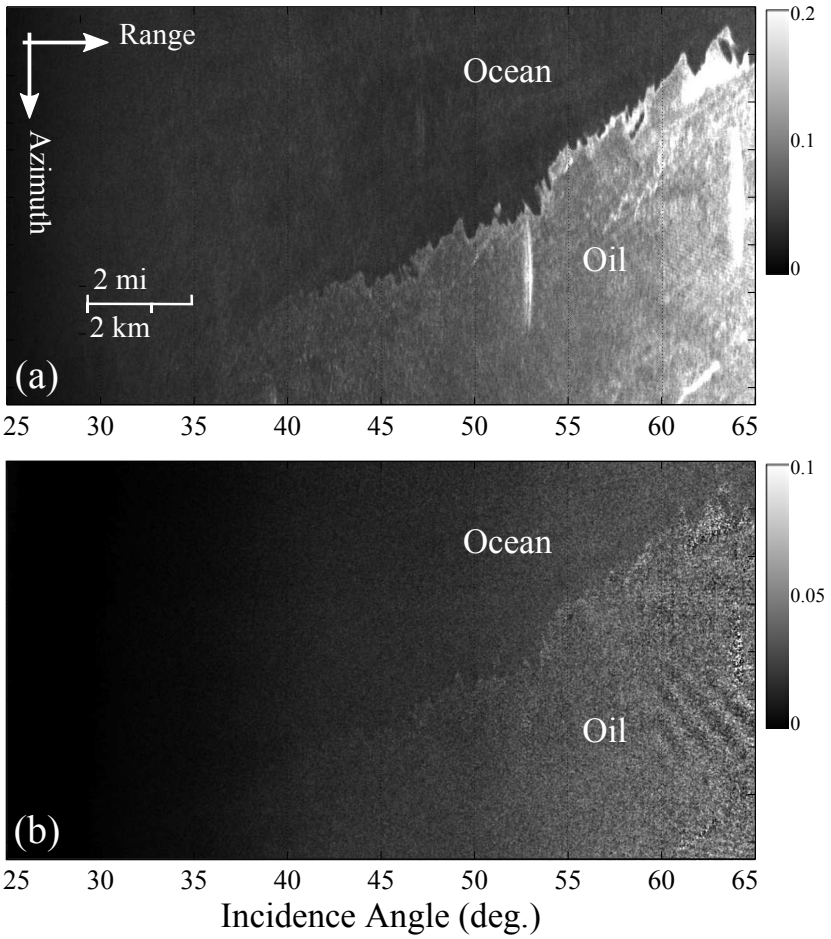

FIG. 4.9. Comparison of co-pol phase difference, and DoD in HH-VV dual-pol SAR. (a) $\overline{\mathcal{P}}_{\text{HH-VV}}$. (b) $\overline{B}_{\varphi_{\text{HH-VV}}}$. The region is is a subset of UAVSAR data set B. A sliding window covering 7×7 pixels is used.

XPD is uniformly distributed over $[-\pi, \pi]$ for any distributed target whereas the CPD is strongly dependent upon the target characteristics [100, 101]. In the Back Scattering Alignment (BSA) convention, an ideal single-bounce (or odd-bounce) scatterer has a CPD of 0°, while an ideal double-bounce (or even-bounce) scatterer has a CPD of 180°. In what follows , we compare the CPD and the DoD from the Deepwater Horizon oil spill under different incidence angles. For this purpose, we define the following simple transformation which maps the phase difference from $[-\pi, \pi]$ to the range of $[0, 1]$

$$\overline{B}_{\varphi_{\text{HH-VV}}} = \frac{1 - \cos(\varphi_{\text{HH-VV}})}{2}. \tag{4.1}$$

Therefore, analogous to the DoD, $\overline{B}_{\varphi_{\text{HH-VV}}}$ is zero for an ideal odd-bounce scatterer, and increases for other scattering mechanisms. Figure 4.9 shows the maps of $\overline{\mathcal{P}}_{\text{HH-VV}}$ and $\overline{B}_{\varphi_{\text{HH-VV}}}$ for a region of interest from the UAVSAR data set B. These results suggest that the oil-ocean contrast is much greater when using the depolarization map compared to the CPD under all incidence angles. To fully appreciate the performance of the DoP/DoD maps, we next compare our dual-pol results with an efficient *full polarimetric* oil spill detection method, newly proposed by NASA/JPL researchers [27].

4.1.2 *Comparison of Dual-Pol DoP with Barakat Quad-pol DoP*

NASA/JPL researchers have newly promoted the Shannon entropy decomposition [97, 111], for the characterization of the oil spills in the Deepwater Horizon oil spill campaign [27]. It has been shown that, the Shannon entropy decomposition is both computationally simpler, and also more effective than Cloude-Pottier decomposition, in the context of oil spill detection [27]. Réfrégier et al. [112] have recently shown that, for Gaussian fields, Shannon entropy is a simple function of the intensity and of the Barakat DoP [113]. The Barakat DoP, given in (1.27), is a well-known and efficient generalization of the DoP for full-polarimetric imaging SAR mode. Figures 4.10 and 4.11 respectively show the Barakat depolarization map and the oil-ocean depolarization ratio calculated using the UAVSAR Deepwater Horizon full polarimetric data set B. The oil-ocean depolarization contrast is obviously best achieved using full polarimetric data along with the Barakat definitions. These figures suggest that the compact/hybrid and HH-VV dual-pol results are closely comparable to the full polarimetric Barakat results across most of the incidence angle range. This analysis is of particular interest, further demonstrating the effectiveness of the DoP in hybrid/compact dual-pol SAR modes for operational oil spill detection over large coastal and ocean areas.

As mentioned earlier, the detection of man-made structures is also of major importance in the maritime surveillance context. Therefore, in

what follows, we study the efficiency of DoP/DoD in different dual-pol SAR modes for the detection of buoys, ships, and offshore oil and gas platforms.

4.2 MAN-MADE MARITIME OBJECT DETECTION: SHIPS, BUOYS, AND OIL RIGS

Estimated savings from using satellite detection and monitoring in mid-ocean in place of expensive aircraft reconnaissance are about $1,800,000 annually [114].

On of the major research axes in maritime monitoring and surveillance is the detection of man-made structures in the ocean (e. g., ships, buoys, oil and gas platforms). Effective, close to real time, detection of such structures is of great interest in a variety of applications. For instance, wide-area identification of ships, cargoes, and offshore oil/-gas platforms after hurricanes and storms can lead to more effective reconnaissance flights, and thus, significant savings and increased safety. Other substantial applications include vessel traffic management, illegal ship discharge control, commercial fishery, and public security.

There exists a rich literature on man-made maritime object detection, notably the detection of ships, using SAR imagery. Most of early publications were based on single channel SAR data acquired by RADARSAT-1 and ERS-1/2. However, in recent years, ship detection studies have been further extended thanks to dual- and quad-pol SAR systems such as ENVISAT ASAR, RADARSAT-2, ALOS-PALSAR, and TerraSAR-X. The publications of Vachon et al. [115], Yeremy et al. [116], Hawkins et al. [117], Ringrose and Harris [118], Sciotti et al. [119], Touzi et al. [120], Liu et al. [121], Marino et al. [29], and Angelliaume et al. [122] provide a good overview of different ship detection methods developed using single- and multi-channel SAR data. In what follows, we concentrate on the polarization signatures of different maritime man-made structures (notably, buoys, ships, and oil-rigs) and demonstrate the effectiveness of the DoP in a variety of scenarios.

4.2.1 *Buoy Detection*

Buoys are distinctively shaped floating devices with many meteorological and navigational purposes. There exist precise nautical charts, usually used as an aid in navigation, which report the exact position of the buoys via different systems. In this study, we use such nautical charts from NOAA as reference, in order to thoroughly evaluate the performance of different polarization combinations. The recent RADARSAT-2 C-band polarimetric data collected over San Francisco Bay, CA, USA, provides a valuable test case for this analysis. This data set is acquired in fine quad-pol FQ9 mode with an incident angle of about 29 degrees. Figure 2.3 shows the NOAA nautical chart and the Pauli RGB image of a test area covering 12 buoys of interest marked with red boxes. We note that some of the buoys are bright enough to be

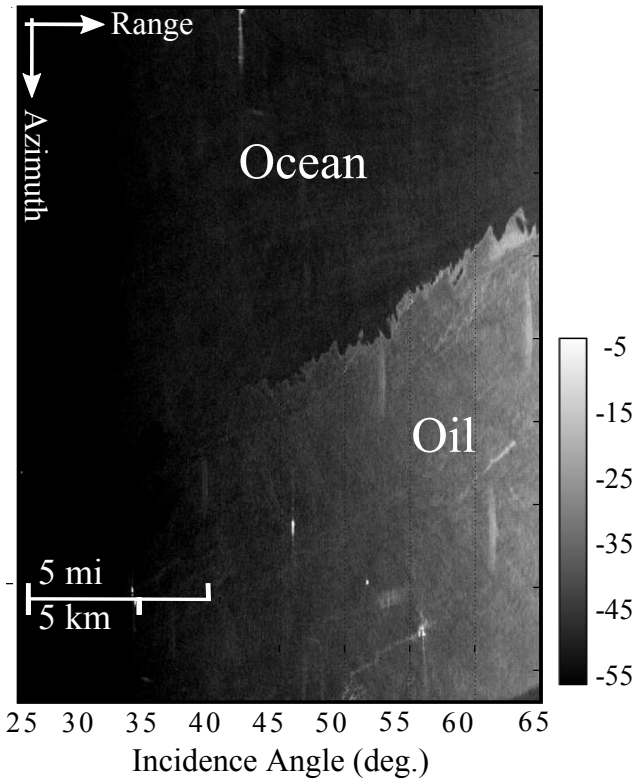

FIG. 4.10. Map of the Barakat quad-pol degree of depolarization (dB) from UAVSAR data set B. The original image has a size of 3151 × 4201 pixels. A sliding window covering 7 × 7 pixels is used.

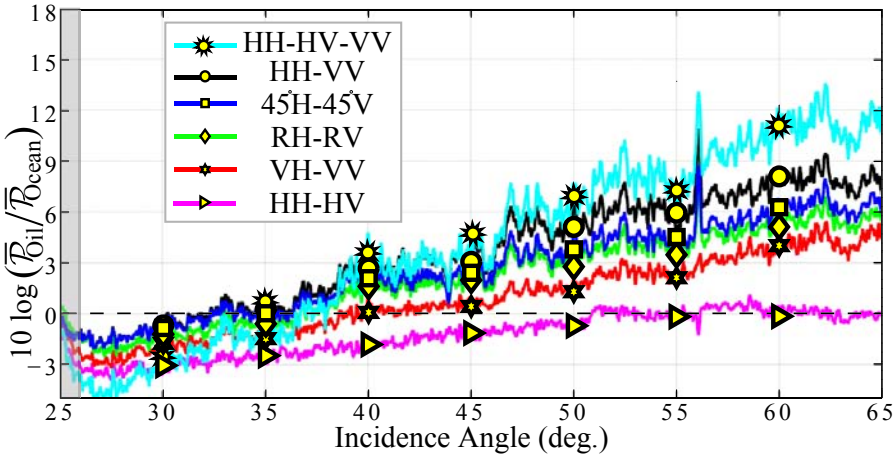

FIG. 4.11. Comparison of the Barakat quad-pol results with dual-pol results (UAVSAR data set B). The further the depolarization ratio is from zero, the better the oil-water depolarization contrast. The gray shaded area indicates the presence of strong specular scattering.

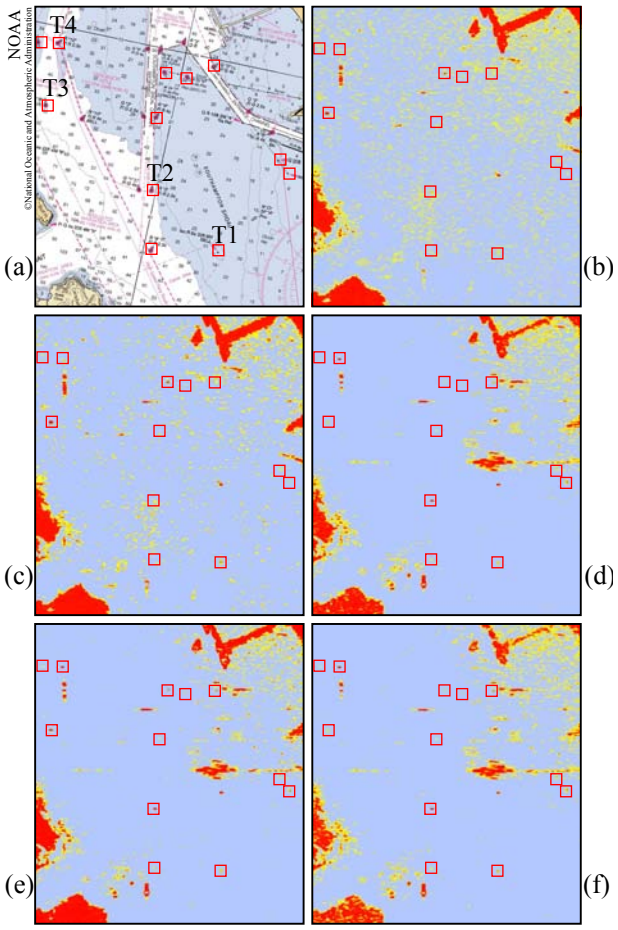

FIG. 4.12. (a) NOAA nautical chart showing the position of the buoys in San Francisco Bay test area (outlined in Fig. 2.2). (b–f) Maps of the degree of polarization in different hybrid/compact and linear dual-pol modes (RADARSAT-2 data); (b) HH-HV. (c) VH-VV. (d) HH-VV. (e) RH-RV. (f) 45°H-45°V. Four buoys of interest, T1–T4, are further studied in Figs. 4.13–4.16.

readily visible on the Pauli RGB image whereas others are hidden in the ocean background. The maps of the DoP obtained over this region for linear and hybrid/compact dual-pol modes are shown in Fig. 4.12. Thresholds were manually chosen so that a maximum number of targets may be visible. These results suggest that, most of the buoys which can hardly be seen in HH-HV and VH-VV modes [Figs. 4.12(b) and 4.12(c)], are easily distinguished in HH-VV and hybrid/compact modes [Fig. 4.12(d–f)]. To further study this issue we now concentrate on polarization signatures of 4 principal buoys marked as T1–T4. The first buoy is the Southampton Shoal day mark (T1) with a height of 32 ft (9.75 m), used to mark the Southampton Shoal in San Francisco Bay. Figure 4.13 shows the DoD surfaces for this buoy in different dual-pol SAR modes. Other buoys of interest are the Southampton Shoal Channel Entrance buoy (T2), the RW "B" North Channel buoy (T3), and the North Channel LTD buoy (T4), for which the DoD surfaces are shown in Figs 4.14–4.16, respectively.

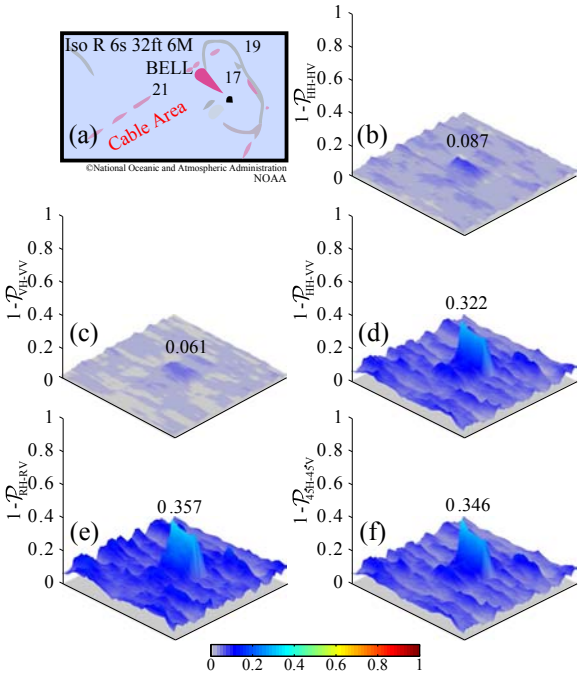

FIG. 4.13. San Francisco Bay, CA, USA. (a) NOAA nautical chart showing the position of Southampton Shoal day mark (T1). (b)–(f) Depolarization signatures in different hybrid/compact and linear dual-pol modes (RADARSAT-2 data); (b) HH-HV. (c) VH-VV. (d) HH-VV. (e) RH-RV. (f) 45°H-45°V.

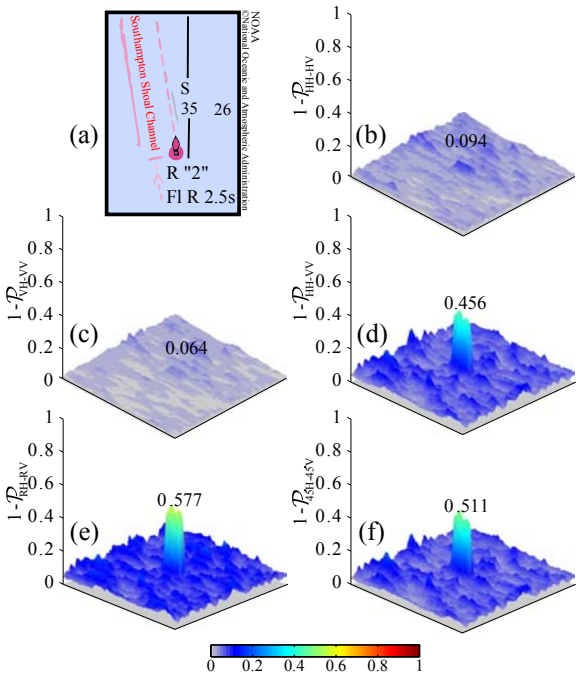

FIG. 4.14. San Francisco Bay, CA, USA. (a) NOAA nautical chart showing the position of Southampton Shoal Channel Entrance buoy (T2). (b)–(f) Depolarization signatures in different hybrid/compact and linear dual-pol modes (RADARSAT-2 data); (b) HH-HV. (c) VH-VV. (d) HH-VV. (e) RH-RV. (f) 45°H-45°V.

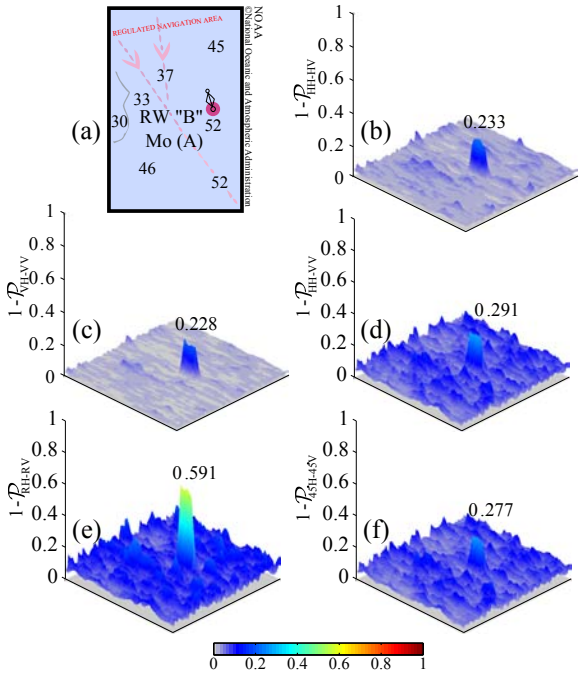

FIG. 4.15. San Francisco Bay, CA, USA. (a) NOAA nautical chart showing the position of RW "B" North Channel buoy (T3). (b)–(f) Depolarization signatures in different hybrid/compact and linear dual-pol modes (RADARSAT-2 data); (b) HH-HV. (c) VH-VV. (d) HH-VV. (e) RH-RV. (f) 45°H-45°V.

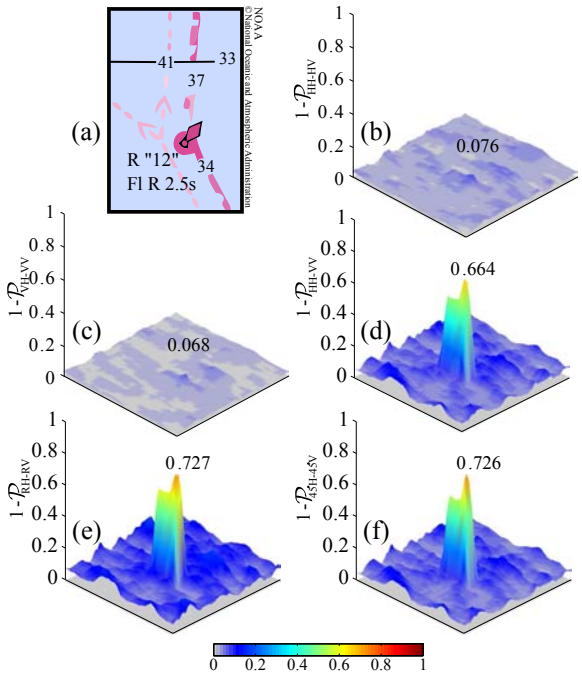

FIG. 4.16. San Francisco Bay, CA, USA. (a) NOAA nautical chart showing the position of North Channel LTD buoy (T4). (b)–(f) Depolarization signatures in different hybrid/compact and linear dual-pol modes (RADARSAT-2 data); (b) HH-HV. (c) VH-VV. (d) HH-VV. (e) RH-RV. (f) 45°H-45°V.

Based on these depolarization surfaces, we can clearly see the gain of performance for buoy detection when using hybrid/compact dual-pol modes compared to linear HH-HV and VH-VV modes. We note that the results from HH-VV mode are also closely comparable to hybrid/compact modes. Similar depolarization signatures are obtained for other buoys present in our test data. Following the same line of study, we consider the detection of oil and gas platforms in what follows.

4.2.2 *Oil rig Detection*

In the context of offshore oil/gas platform detection, Gulf of Mexico is an interesting study case with nearly 4,000 active oil and gas platforms. We use L-band polarimetric data collected by UAVSAR over Mississippi River Delta, LA, USA, for this analysis. The nautical chart and Pauli RGB image of this data set are shown in Fig. 2.10. The polarization maps along with the NOAA ground truth of a region of interest, covering 16 oil and gas platforms, are shown in Fig. 4.17. Moreover, the DoD surfaces of two oil platforms from this region are further studied in Fig. 4.18. These figures confirm the results obtained in the buoy detection case, that is, oil/gas platforms are much better detected in HH-VV and compact/hybrid SAR modes compared with the HH-HV and VH-VV modes.

We highlight that oil/gas platforms have a completely different structure than buoys; they are massive metal structures, usually in the form of a square supported by vertical cylinders at the corners, with a water (or a relatively flat) area present in the center (see Fig. 2.9 for

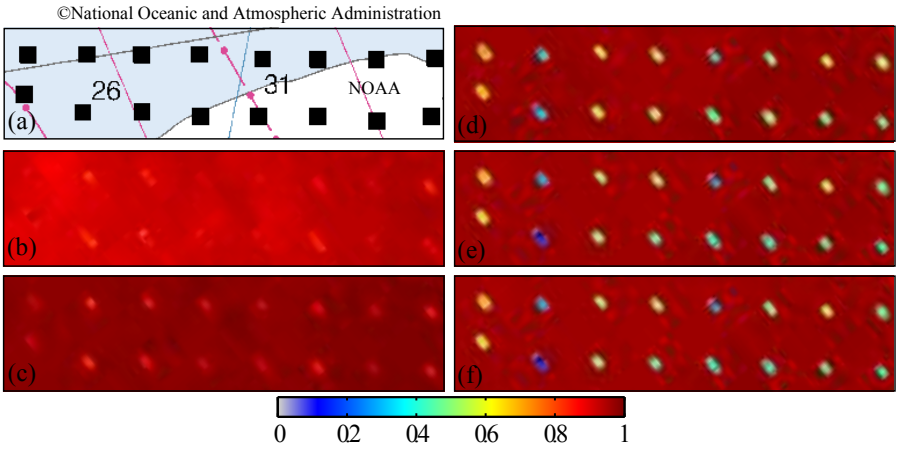

FIG. 4.17. (a) NOAA nautical chart showing the position of 16 oil/gas platforms in a test area around Mississippi River Delta (outlined in Fig. 2.10). (b–f) Maps of the degree of polarization in different hybrid/compact and linear dual-pol modes (UAVSAR data); (b) HH-HV. (c) VH-VV. (d) HH-VV. (e) RH-RV. (f) 45°H-45°V. Two rigs of interest (in the left) are further studied in Fig. 4.18.

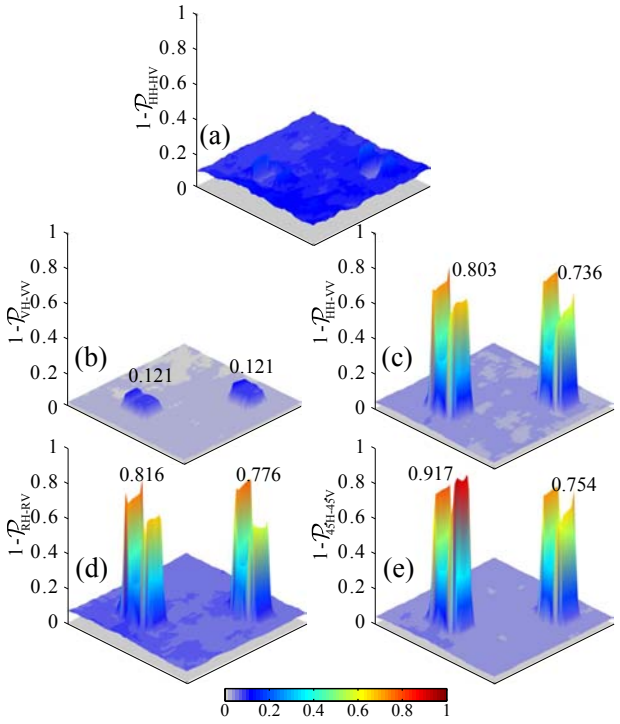

FIG. 4.18. Depolarization signatures of two oil platforms in different hybrid/-compact and linear dual-pol modes (UAVSAR data); (b) HH-HV. (c) VH-VV. (d) HH-VV. (e) RH-RV. (f) 45°H-45°V.

two examples). The structure of these platforms directly influences the depolarization signatures. We observe in Fig. 4.18(c)–(e), that the oil platforms produce very high depolarization values around the border whereas they have very low depolarization values in the center, due to the presence of water (or flat) areas. Similar depolarization signatures are obtained for other oil/gas platforms present in our test data set. These depolarization surfaces are of particular interest, demonstrating the potential of the DoP/DoD for target identification and recognition by revealing important information that lies behind the complex structure of man-made objects. In order to fully appreciate the usefulness and accuracy of the DoP/DoD maps, we study a ship detection scenario in which we compare our dual-pol results with an efficient *full polarimetric* method, recently proposed by Marino et al. [28, 29].

4.2.3 *Ship Detection: Comparison of Dual-Pol DoP with Full-Pol Notch Filter*

In this section we study the performance of the DoP in a ship detection context. For this purpose, we compare the DoP maps with an effective ship detection method, newly proposed by Marino et al. [28, 29], which is based on full polarimetric data and sophisticated notch filters. Figure 4.19(a) shows the Pauli RGB image of a region of interest from RADARSAT-2 San Francisco Bay data set. Figures 4.19(b)–(f)

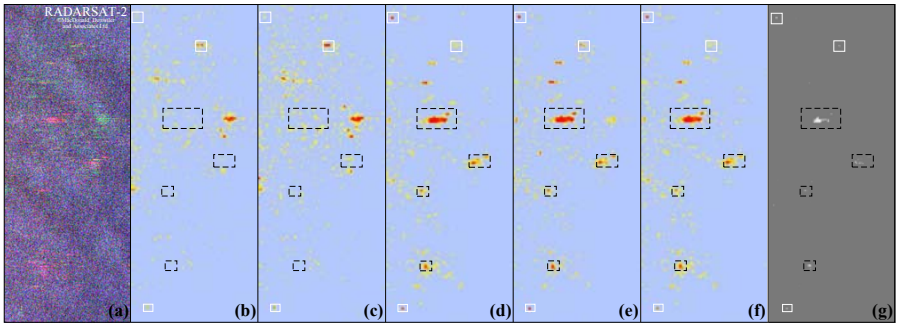

FIG. 4.19. Ship detection in San Francisco Bay, CA, USA. (a) Pauli RGB image of the test area from RADARSAT-2 full polarimetric data. (b)–(f) Maps of the degree of polarization in different dual-pol SAR modes; (b) HH-HV. (c) VH-VV. (d) HH-VV. (e) RH-RV. (f) 45°H-45°V. (g) Ship detection results, based on quad-pol data, reported by Marino et al. [28, 29]. Boxes indicate potential ships; solid (white) boxes indicate targets that are visible in all modes whereas dashed (black) boxes indicate less- or non-visible targets in traditional (linear) dual-pol modes.

show the maps of the DoP obtained in linear and hybrid/compact dual-pol modes over this test region. In these figures, thresholds were manually chosen so that a maximum number of targets may be visible. Figure 4.19(g) shows the ship detection results reported by Marino et al. [28, 29] obtained using a notch filter based on full-pol SAR data. In these figures, boxes indicate potential ships; solid (white) boxes indicate targets that are visible in all modes whereas dashed (black) boxes indicate less- or non-visible targets in linear dual-pol modes. We see that most of the ships detected using the full-pol method are not visible in the HH-HV and VH-VV dual-pol modes (black, dashed boxes) whereas they are clearly seen in HH-VV and hybrid/compact dual-pol modes. Moreover, the ship detection results based on the estimation of the DoP in hybrid and compact dual-pol modes are closely comparable to the notch filter results which are obtained based on the full polarimetric information of the scene. These results are in agreement with those obtained in previous sections. However, we highlight that the ship detection problem is distinct in that ships can introduce a preferred orientation because of their structure. Therefore, some ships may be more visible in some linear dual-pol modes than the others depending on their alignment. This is not of concern in dual-pol modes with a circular transmit polarization.

4.3 CONCLUSION

The DoP was used to detect the features, such as ships, oil-rigs and oil spills, with different polarimetric signatures compared with the sea clutter. The detection performance of the DoP was studied in different hybrid/compact and linear dual-pol SAR modes. It was shown that the DoP provides valuable information for ship detection and oil spill recognition under different polarizations and incidence angles. Experiments were performed on RADARSAT-2 C-band polarimetric data sets, over San Francisco Bay, and L-band NASA/JPL UAVSAR data, covering the Deepwater Horizon oil spill in the Gulf of Mexico.

Important conclusions were reached; hybrid/compact and (HH, VV) dual-pol modes deliver better ship and oil-spill detection results compared to classical linear dual-pol modes, i. e., (HH, HV) and (VH,VV). More importantly, the detection results based on the estimation of the DoP in hybrid and compact dual-pol modes are closely comparable to the results achieved using newly promoted full polarimetric methods.

5

INCOHERENT DUAL-POL DOP: PERFORMANCE ASSESSMENT

Past performance speaks a tremendous amount about one s ability and likelihood for success.

— Mark Spitz

Some remote sensing applications involve high resolution mapping of large areas with frequent visites. The futur Sentinel-1, for example, aims at providing incoherent multi-look dual-pol SAR imagery[1] with a high temporal resolution. Also, a valuable portion of satellite SAR archives (e. g., ENVISAT ASAR and AirSAR CYCLOPS) contain only incoherent imagery datasets. Besides, the actual systems continue to deliver incoherent data amongst other product types.

Incoherent dual-pol SAR systems capture only two multi-look intensity images from a scene. As a consequence, none of the PolSAR discriminators which depend on the complex cross product between channels can be calculated. The DoP, on the other hand, can still be estimated using only two intensity images as demonstrated in § 3.3.2. In this chapter, we concentrate on the performance assessment of the DoP estimators, based on incoherent dual-pol data, over various terrain types such as urban, vegetation, and ocean. This analysis is not only useful for incoherent SAR data, but also of great interest in understanding and quantifying the information captured from a scene by the amplitude part of the coherent[2] dual-pol data.

[1] Labelled as Ground Range Multi-Look Detected (GRD) products.

[2] Coherent dual-pol systems measure complex signals, based on which covariance matrix and Stokes vector (four intensity images) can be derived. The amplitude part of the captured data is only sufficient to calculate two of the four Stokes parameters (i. e., two intensity images).

TABLE 5.1. DoP and the corresponding covariance matrices of synthetic polarimetric images.

	$\mathbf{\Gamma}_0$	$\mathbf{\Gamma}_1$	$\mathbf{\Gamma}_2$	$\mathbf{\Gamma}_3$	$\mathbf{\Gamma}_4$	$\mathbf{\Gamma}_5$	$\mathbf{\Gamma}_6$	$\mathbf{\Gamma}_7$	$\mathbf{\Gamma}_8$	$\mathbf{\Gamma}_9$
a_1	2	5	15	1	16	82	18	30	2	1.25
a_2	2	5	6	1	3.6	17	11	14	2	26
a_3	0	1	0.2	0.4	0	0	7	16	0.6	0
a_4	0	0	0.5	$\sqrt{0.14}$	0	13	8	8	1.8	5.5
$\mathcal{P}$	**0**	**0.20**	**0.45**	**0.55**	**0.63**	**0.70**	**0.77**	**0.90**	**0.95**	**0.99**

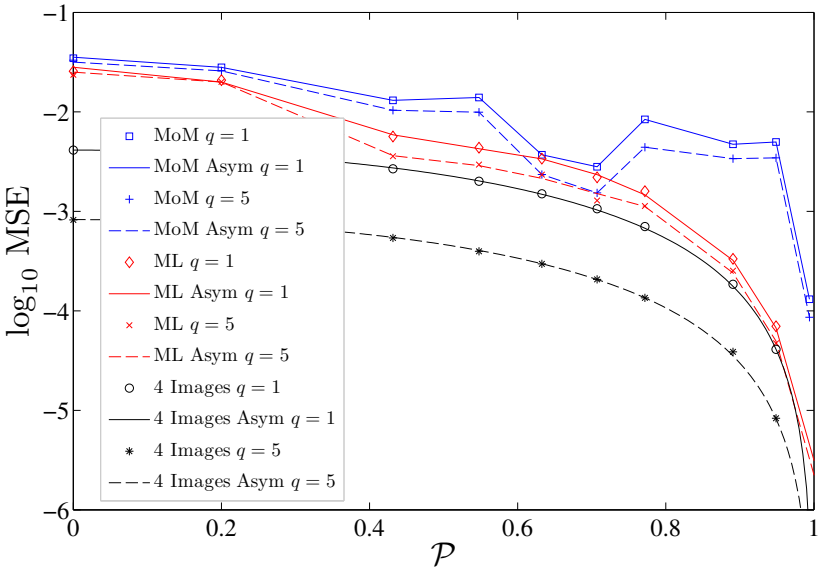

FIG. 5.1. log MSE of $\widehat{\mathcal{P}}$ as a function of $\mathcal{P}$ for polarization matrices $\mathbf{\Gamma}_i$ and $n = 11 \times 11$. Number of Monte Carlo realizations is 10^3, and $q =$ number of looks.

5.1 PERFORMANCE ANALYSIS WITH SYNTHETIC DATA

To evaluate the performance of the incoherent ML and MoM DoP estimators, derived in § 3.3.2, we first consider a set of synthetic polarimetric images [79]. Synthetic polarimetric images can be generated from the polarimetric covariance matrix $\mathbf{\Gamma}$. For this purpose, we consider ten different values of $\mathbf{\Gamma}$ denoted as $\mathbf{\Gamma}_0, \mathbf{\Gamma}_1, \ldots, \mathbf{\Gamma}_9$, as shown in Table 5.1.

Figure 5.1 provides us with a simple approach to quantize the unavoidable loss of information caused by measurement of intensities (instead of complex signals) in incoherent dual-pol systems. It shows the log Mean Square Error (logMSE) of the DoP estimates obtained with two intensity images (incoherent dual-pol) using ML estimator (red diamond markers) and MoM estimator (blue square markers) for different numbers of looks. Comparing these MSEs with those corre-

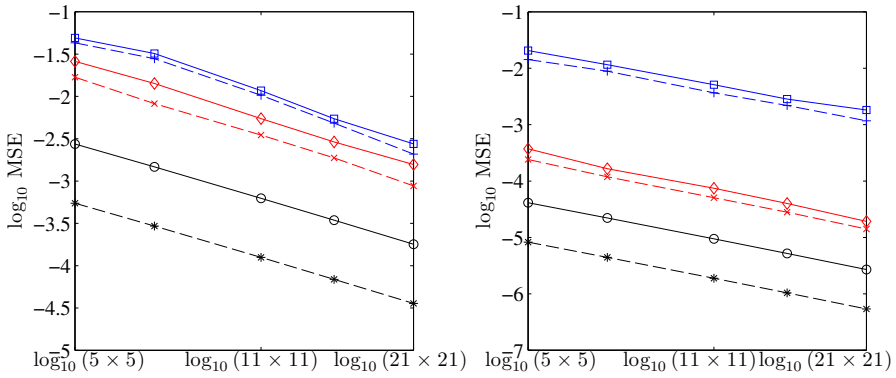

FIG. 5.2. (left) log MSE of $\widehat{\mathcal{P}}$ versus the logarithm of the sample size for the matrix $\mathbf{\Gamma}_2$. (right) for the matrix $\mathbf{\Gamma}_8$. Number of Monte Carlo realizations is 10^3, and q = number of looks. Labels are the same as Fig. 5.1

sponding to (coherent dual-pol) four images (black circle markers), the performance loss that occurs when using only two intensity images, instead of four, can be clearly observed. Also, the ML estimators of the DoP deliver better estimations than the MoM estimators, which confirms a classical result. The theoretical asymptotic logMSEs associated with the ML estimators and the asymptotic lower bound for MoM estimators [corresponding to (3.21), (3.31), and (3.44)] are also shown in Fig. 5.1. We see that ML and MoM estimators deliver good estimations when $\mathcal{P}$ is close to one, whereas they tend to estimate the DoP less accurately when $\mathcal{P}$ is close to zero. This confirms that the incoherent estimation of the DoP is more precise for highly polarized regions than moderately polarized areas.

Figure 5.2 shows the performance of the different estimators as a function of the sample size n for different numbers of looks and two matrices $\mathbf{\Gamma}_2$ and $\mathbf{\Gamma}_8$ (given in Table 5.1). The usual linear relation between $\log_{10}$ MSE and $\log_{10}(n)$ is observed in both single- and multi-look cases. These figures also show the gain of performance obtained with the ML method compared to the MoM. We note that ML is significantly better than MoM for $\mathbf{\Gamma}_8$ ($\mathcal{P}$ close to one). In other words, the DoP estimation using ML method is more precise than MoM, especially in highly polarized regions (thanks to the weighted second-order moment of $\widehat{r}_{\text{ML}}$). As aforementioned, the speckle noise is better reduced with a larger number of looks; the larger the number of looks q, the better the estimation performance is for both ML and MoM estimators.

5.2 PERFORMANCE ANALYSIS IN LINEAR DUAL-POL SAR IMAGERY

In this section, we analyze the performance of the ML and MoM estimators using PolSAR data presented in Chapter 2.3. Maps of the DoP in (HH, HV) and (HV,VV) dual-pol modes for RADARSAT-2 San Francisco

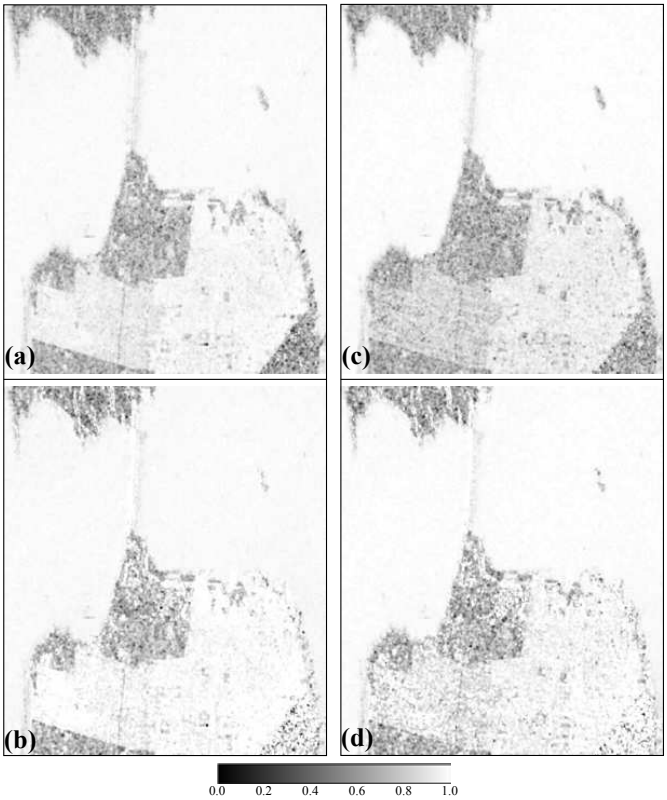

FIG. 5.3. Comparison of the DoP ML and MoM estimators in dual-pol modes. RADARSAT-2 image of San Francisco Bay, CA. (a) $\widehat{\mathcal{P}}_{\mathrm{ML}}$ in (HH, HV) mode. (b) $\widehat{\mathcal{P}}_{\mathrm{MoM}}$ in (HH, HV) mode. (c) $\widehat{\mathcal{P}}_{\mathrm{ML}}$ in (VH, VV) mode. (d) $\widehat{\mathcal{P}}_{\mathrm{MoM}}$ in (VH, VV) mode. A sliding window covering $n = 9 \times 9$ pixels is used.

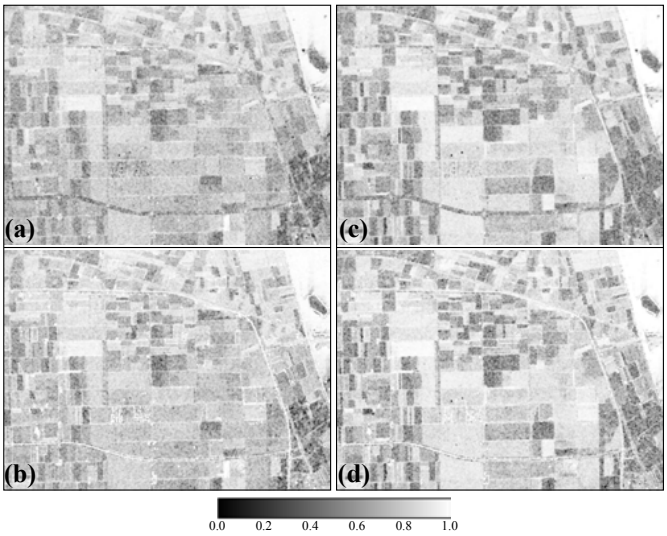

FIG. 5.4. Comparison of the DoP ML and MoM estimators in dual-pol modes. NASA/JPL AirSAR image of Flevoland, The Netherlands. (a) $\widehat{\mathcal{P}}_{\mathrm{ML}}$ in (HH, HV) mode. (b) $\widehat{\mathcal{P}}_{\mathrm{MoM}}$ in (HH, HV) mode. (c) $\widehat{\mathcal{P}}_{\mathrm{ML}}$ in (VH, VV) mode. (d) $\widehat{\mathcal{P}}_{\mathrm{MoM}}$ in (VH, VV) mode. A sliding window covering $n = 5 \times 5$ pixels is used.

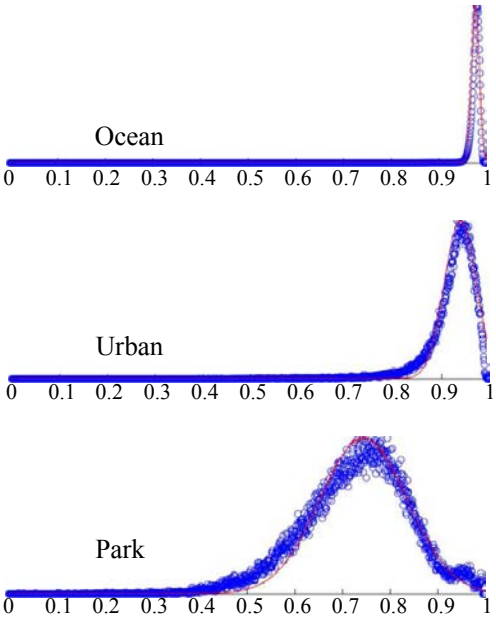

FIG. 5.5. Experimental histograms and asymptotic PDFs of the DoP ML estimator in (HH, HV) dual-pol mode, over different regions of the San Francisco Bay image (RADARSAT-2 data set). (Top) Ocean. (Middle) Urban 1. (Bottom) Park. Regions are shown in Fig. 2.2(d). A sliding window covering 9×9 pixels is used for the DoP estimation.

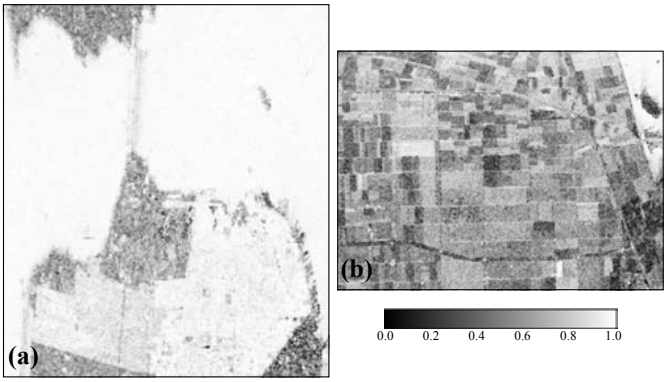

FIG. 5.6. Maps of the degree of polarization based on four intensity images. (a) San Francisco Bay, CA, USA, $n = 9 \times 9$. (b) Flevoland, The Netherlands, $n = 5 \times 5$.

Bay and AirSAR Flevoland data sets are presented in Figs. 5.3 and 5.4, respectively. A visual inspection of the results suggests that all the estimators have a similar global behavior with the water areas having the maximum DoP and the vegetation areas having the minimum DoP. For the ML estimator, the asymptotic PDF is available from (3.35). Figure 5.5 shows the experimental DoP histograms (blue, circle markers) and the corresponding asymptotic PDFs (red, solid line) for ML estimator in ocean, park, and urban areas. There is a good agreement between the experimental histograms and the theoretical PDFs. For the urban and park areas, mismatches are observed due to the inevitable

inhomogeneity in the selected regions. As expected, the DoP is directly related to the terrain types.

Since the DoP estimation based on four images is the benchmark (classical) estimation, we consider it as reference. The DoP reference maps are shown in Fig. 5.6. We use scatter plots in order to examine how well the DoP estimations based on two intensity images fit the DoP estimations based on four images. Figure 5.7 shows the scatter plots of the DoP ML and MoM estimations over different regions of the San Francisco Bay area in (HH, HV) dual-pol mode. The scatter plots have been normalized in the range of $[0, 1]$. The closer the estimated values are to the diagonal line, the better the estimation, compared to the given reference (note that the scatter plots of the ocean region are shown in a different scale). There are several phenomena to note in Fig. 5.7. The ML estimators of the DoP deliver better estimations over all the different terrain types, present in our data set, compared to MoM estimators. Both ML and MoM estimators tend to overestimate the DoP for urban areas (values over the diagonal line). These estimators deliver good estimations for values of $\widehat{\mathcal{P}}$ close to 1 (ML over the ocean being the best). However, they tend to estimate the DoP less accurately in the vegetation areas with $\widehat{\mathcal{P}}$ values close to 0.70 (MoM estimator over the park area being the worst). This is in agreement with the results from synthetic data presented in Fig. 5.1. Scatter plots derived from other presented data sets suggest the same results. Figure 5.8 shows the scatter plots of the ML and MoM estimators for different sizes of the sliding window, over the park region. It confirms that a bigger sliding window leads to better estimation results for both ML and MoM estimators. We also notice that for each sliding window, the ML method gives estimators with smaller variances (i. e., better performance) compared to the corresponding MoM estimators.

5.3 Comparison of DoP estimations in hybrid/compact and linear dual-pol modes

In this section we study and compare the ML estimators of the DoP, based on two intensity images, in hybrid/compact and linear dual-pol modes. Figs. 5.9 and 5.10 show the maps of the DoP obtained using two intensity images delivered in each hybrid/compact and linear dual-pol mode, for RADARSAT-2 San Francisco Bay and AirSAR Flevoland data sets, respectively.

A visual inspection of the results suggests that the DoP estimates in traditional linear dual-pol modes, i. e., Fig. 5.9(a–b), are better suited for the segmentation of the image, compared to other hybrid/compact dual-pol modes. The mean μ and variance σ^2 of these DoP ML estimates are given in Table 5.2, over different regions of interest (ocean, park and urban). We note that, the proposed ML estimators are asymptotically unbiased, and thus the variance can demonstrate the

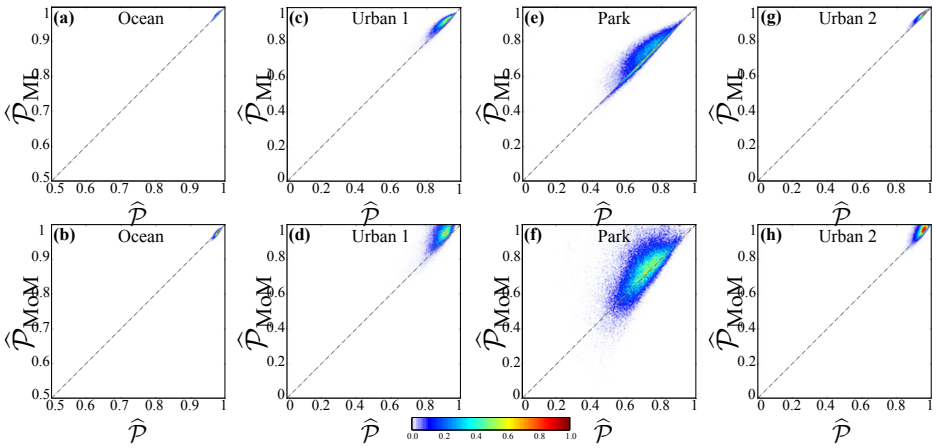

FIG. 5.7. Scatter plots of the DoP ML and MoM estimates in (HH, HV) dual-pol mode versus the DoP estimates based on four intensity images over different regions of the San Francisco Bay image (RADARSAT-2 data set). On the abscissa are $\widehat{\mathcal{P}}$ based on four intensity images, and on the ordinate are the estimated values in the dual-pol mode. Perfectly estimated values lie along the diagonal line. (a) $\widehat{\mathcal{P}}_{\mathrm{ML}}$ over ocean. (b) $\widehat{\mathcal{P}}_{\mathrm{MoM}}$ over ocean. (c) $\widehat{\mathcal{P}}_{\mathrm{ML}}$ over urban 1. (d) $\widehat{\mathcal{P}}_{\mathrm{MoM}}$ over urban 1. (e) $\widehat{\mathcal{P}}_{\mathrm{ML}}$ over park. (f) $\widehat{\mathcal{P}}_{\mathrm{MoM}}$ over park. (g) $\widehat{\mathcal{P}}_{\mathrm{ML}}$ over urban 2. (h) $\widehat{\mathcal{P}}_{\mathrm{MoM}}$ over urban 2. Regions are shown in Fig. 2.2(d). A sliding window covering 9×9 pixels is used.

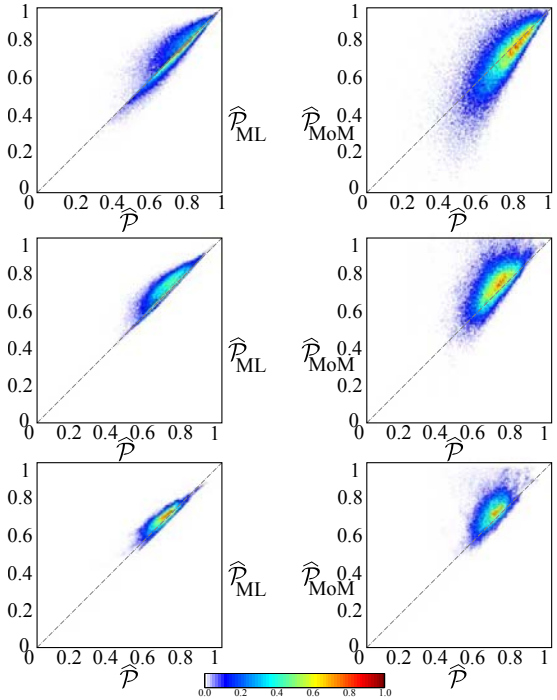

FIG. 5.8. Comparison of the scatter plots of the DoP ML and MoM estimates for different sliding windows over the park region. On the abscissa are $\widehat{\mathcal{P}}$ based on four intensity images, and on the ordinate are the estimated values in the (HH, HV) dual-pol mode. Perfectly estimated values lie along the diagonal line. (Left column) $\widehat{\mathcal{P}}_{\mathrm{ML}}$. (Right column) $\widehat{\mathcal{P}}_{\mathrm{MoM}}$. (First row) $n = 5 \times 5$. (Second row) $n = 11 \times 11$. (Third row) $n = 19 \times 19$.

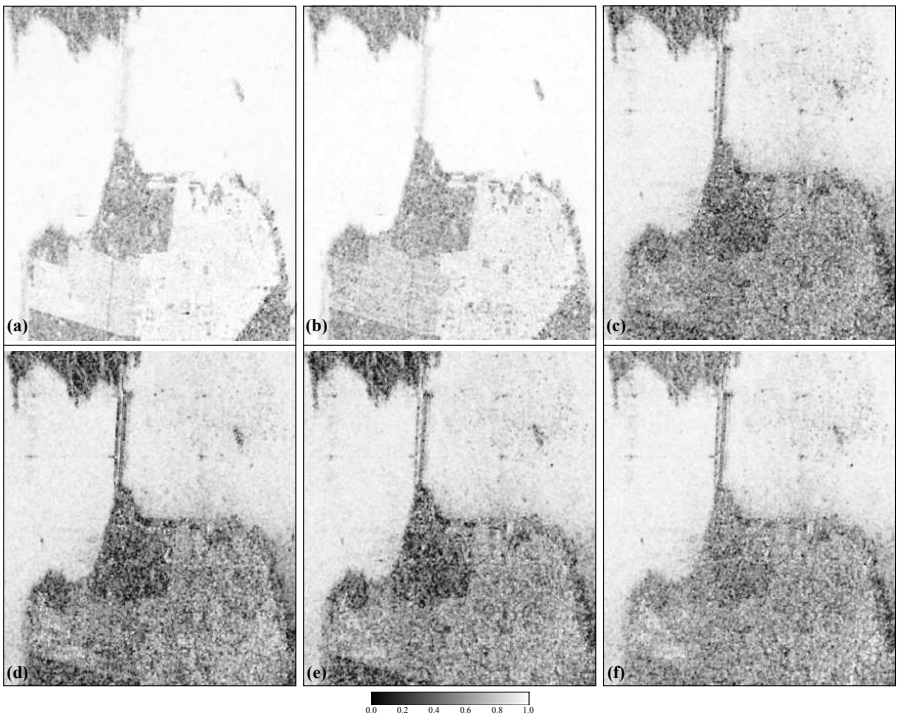

FIG. 5.9. Maps of the degree of polarization (ML estimates) in different hybrid/compact and linear dual-pol modes, over San Francisco Bay area (RADARSAT-2 data set). (a) HH-HV. (b) VH-VV. (c) HH-VV (d) DCP. (e) CL-pol. (f) $\pi/4$. A sliding window covering 9×9 pixels is used.

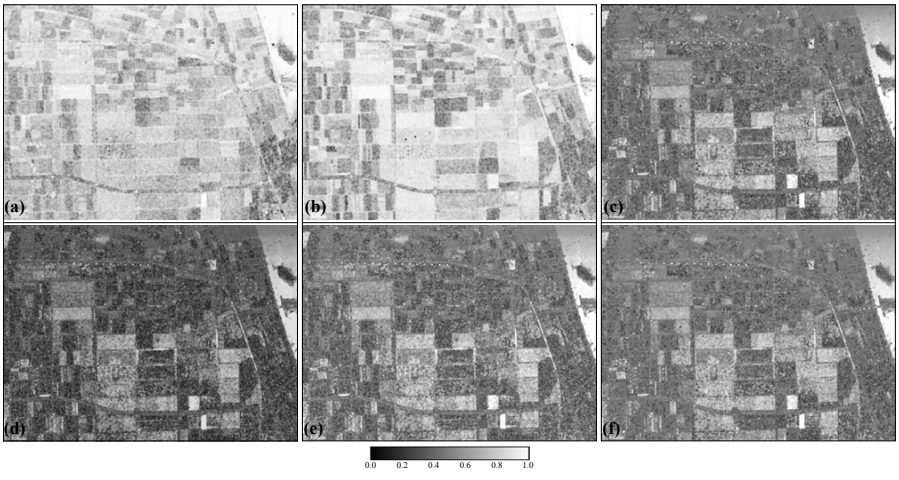

FIG. 5.10. Maps of the degree of polarization (ML estimates) in different hybrid/compact and linear dual-pol modes, over Flevoland, The Netherlands (AirSAR data set). (a) HH-HV. (b) VH-VV. (c) HH-VV (d) DCP. (e) CL-pol. (f) $\pi/4$. A sliding window covering 5×5 pixels is used.

performance of the estimators. Since the ocean region is a homogeneous region, the estimates with small variances demonstrate better estimation performance. Interestingly, the traditional linear dual-pol modes, i. e., (HH, HV) and (VH, VV), give estimators with smaller variances (i. e., better performance) compared to hybrid/compact dual-pol modes. These results lead us to draw the conclusion that, although for coherent dual-pol systems, the hybrid/compact dual-pol modes perform better than classical linear modes, for incoherent dual-pol SARs, this role is inverted.

The statistics of the DoP ML estimators in different hybrid/compact and linear dual-pol modes are further studied for water, urban, and vegetation areas in Figs. 5.11, 5.12, and 5.13, respectively. For each of such areas, three test regions are chosen from the RADARSAT-2 Vancouver, the RADARSAT-2 San Francisco Bay, and the AirSAR San Francisco Bay data sets. The test regions are outlined in Figs. 2.2(d), 2.4(b), and 2.5(b). We note that the selected water regions are homogeneous regions with odd-bounce scattering mechanism. On the other hand, the urban areas include buildings, streets, grass, trees, and other structures. Therefore, the urban regions represent combinations of different scattering mechanisms, although even-bounce scattering is dominant. The vegetation regions exhibit volume scattering mechanism. In these figures, the variance of the DoP shows that urban and vegetation areas are more random than ocean areas (which is well known). Moreover, we notice that the mean value of the DoP is contrasting among test regions. Hence, DoP mean values can provide useful information for distinguishing different regions. These results are of interest for the classification and segmentation of polarimetric SAR images, in particular, the distinction of urban and vegetation areas from water areas (compare Figs. 5.12, and 5.13 to Fig. 5.11). We highlight that, due to the high level of detail involved in the urban environment, the full benefit of the DoP for urban applications is achieved by performing the DoP estimation on high resolution SAR images. This is an interesting subject for future work, notably with the advent of new emerging high-resolution SAR systems such as RADARSAT-2 ultra-fine mode (3m), and TerraSAR-X high-resolution Spotlight mode (up to 1m).

The results presented in this chapter strongly suggest that the classical linear dual-pol modes perform far better than the emerging hybrid and compact modes when we only have access to the amplitude of dual-pol SAR data (or incoherent data). A similar conclusion can be drawn based on the approach presented by Lee et al. [110], notably considering the total correct classification rates given in [110, Table III]. For intensity dual-pol data, the total correct classification rates are greater for ($|\mathrm{HH}|^2$, $|\mathrm{HV}|^2$) and ($|\mathrm{VH}|^2$, $|\mathrm{VV}|^2$) compared to ($|\mathrm{HH}|^2$, $|\mathrm{VV}|^2$). Thus, we see that in this context (HH, HV) and (VH, VV) outperform (HH, VV) for image classification. However, such a conclusion does not necessary hold when considering the complex dual-pol data

TABLE 5.2. Mean μ and variance σ^2 of the DoP ML estimates in different polarimetric modes, over ocean, park, urban 1, and urban 2 regions of RADARSAT-2 San Francisco Bay data set [regions are shown in Fig. 2.2(d)].

	HH-HV		VH-VV		HH-VV		DCP		CL-pol		$\pi/4$	
	μ	σ^2	μ	σ^2	μ	σ^2	μ	σ^2	μ	σ^2	μ	σ^2
Ocean	0.975	1e-4	0.982	1e-4	0.929	12e-4	0.910	16e-4	0.910	17e-4	0.928	12e-4
Park	0.721	111e-4	0.692	111e-4	0.466	316e-4	0.398	336e-4	0.405	344e-4	0.537	255e-4
Urban 1	0.920	20e-4	0.827	50e-4	0.603	198e-4	0.562	285e-4	0.604	213e-4	0.647	177e-4
Urban 2	0.949	16e-4	0.913	30e-4	0.602	221e-4	0.584	280e-4	0.603	223e-4	0.618	212e-4

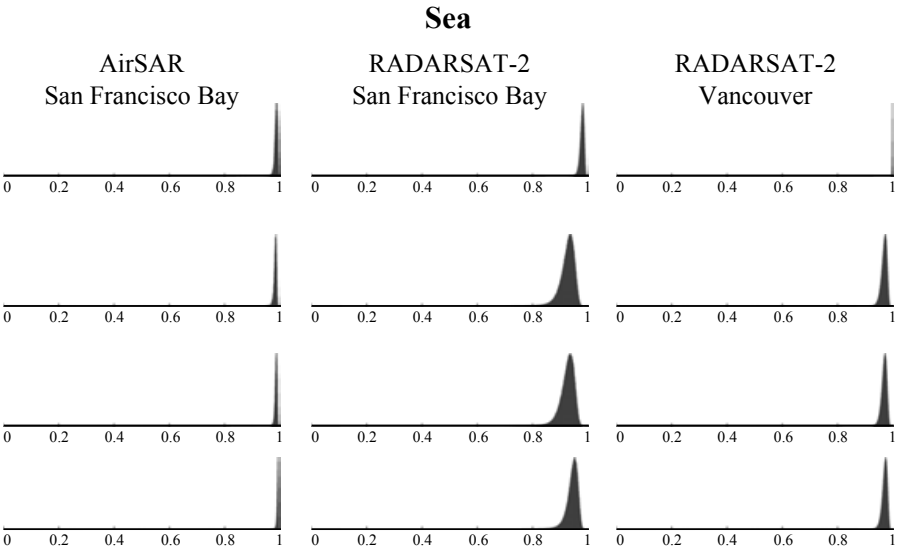

FIG. 5.11. Histograms of the DoP ML estimates in different polarimetric modes over three different water areas. (First row) HH-HV. (Second row) DCP. (Third row) CL-pol. (Forth row) $\pi/4$. (Left column) Water area from the AirSAR San Francisco Bay data. (Middle column) Water area from the RADARSAT-2 San Francisco Bay data. (Right column) Water area from the RADARSAT-2 Vancouver data. Regions are shown in Figs. 2.2(d), 2.4(b), and 2.5(b). A sliding window covering 9×9 pixels is used.

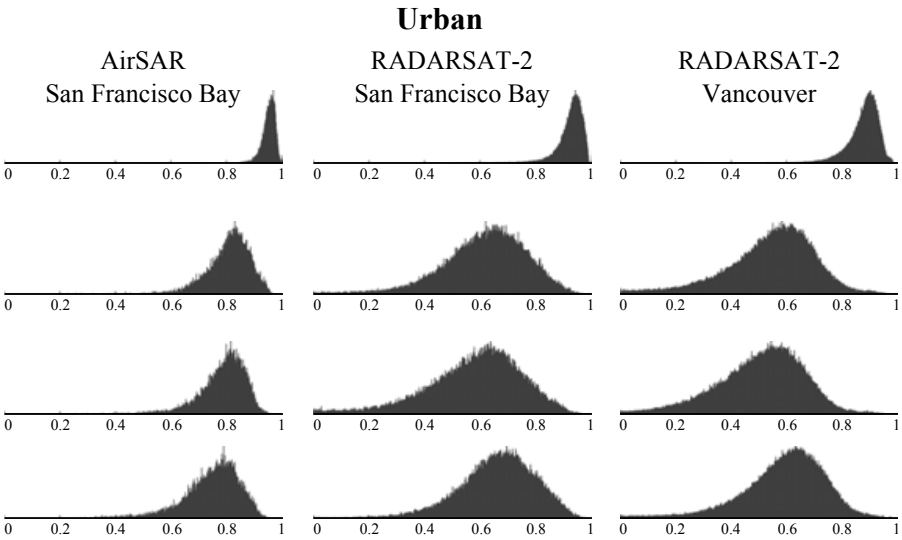

FIG. 5.12. Histograms of the DoP ML estimates in different polarimetric modes over three different urban areas. (First row) HH-HV. (Second row) DCP. (Third row) CL-pol. (Forth row) $\pi/4$. (Left column) Urban area from the AirSAR San Francisco Bay data. (Middle column) Urban area from the RADARSAT-2 San Francisco Bay data. (Right column) Urban area from the RADARSAT-2 Vancouver data. Regions are shown in Figs. 2.2(d), 2.4(b), and 2.5(b). A sliding window covering 9×9 pixels is used.

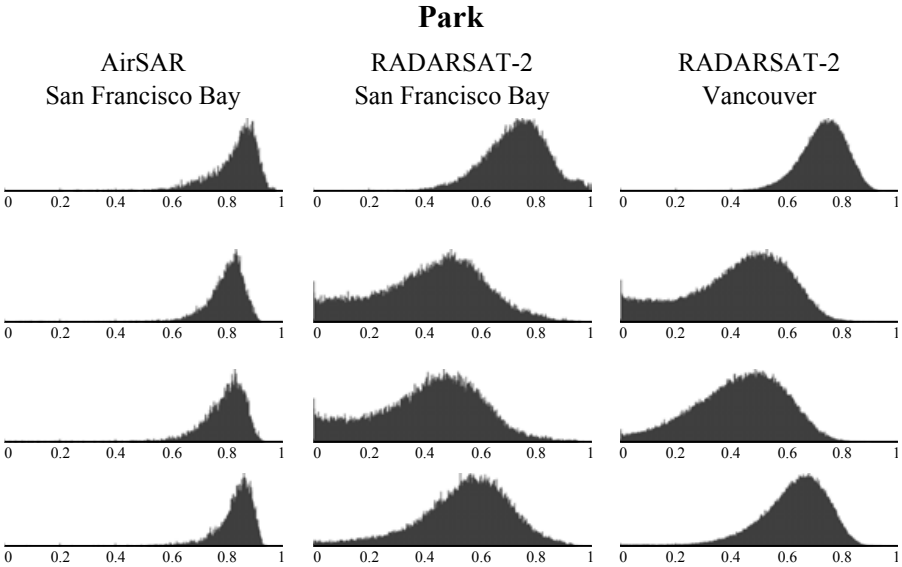

FIG. 5.13. Histograms of the DoP ML estimates in different polarimetric modes over three different vegetation areas. (First row) HH-HV. (Second row) DCP. (Third row) CL-pol. (Forth row) $\pi/4$. (Left column) Vegetation area from the AirSAR San Francisco Bay data. (Middle column) Vegetation area from the RADARSAT-2 San Francisco Bay data. (Right column) Vegetation area from the RADARSAT-2 Vancouver data. Regions are shown in Figs. 2.2(d), 2.4(b), and 2.5(b). A sliding window covering 9×9 pixels is used.

(with the coherent phase information) as detailed in Chapter 4. In what follows, we present a brief analysis to illustrate the information content of the coherent phase in different dual-pol SAR modes.

5.4 PHASE DIFFERENCE AND COHERENCE IN LINEAR, HYBRID/-COMPACT, AND CIRCULAR DUAL-POL SAR

The coherence and the phase difference have long been considered as two valuable discriminators for terrain classification and parameter estimation. There exists a rich literature on the behavior of the phase difference in classical linear dual-pol SAR modes (see [52] and references therein). It is now well understood that the phase differences between co-pol terms and cross-pol terms are not as important as that between HH and VV. In fact, co-pol and cross-pol terms are generally uncorrelated in distributed targets. Hence, the cross-pol phase (between HH and HV, or VH and VV) is uniformly distributed over $(-\pi, \pi)$ for any distributed target. On the other hand, the co-pol phase (between HH and VV) is strongly dependent upon the target characteristics [101]. In this section, following the same line of thought as in [78], we extend the analysis of the coherence and the phase difference to hybrid/compact, and circular dual-pol modes.

The complex correlation coefficient (or coherence) is a cardinal parameter in describing the phase difference statistics. The multilook phase difference, denoted as $\varphi_{s_i s_j}$, and the complex correlation coefficient, denoted as $\rho_{s_i s_j}$, are classically defined as

$$\varphi_{s_i s_j} = \operatorname{Arg}\left(\frac{1}{q}\sum_{m=1}^{q} S_i[m] S_j^*[m]\right), \; -\pi < \varphi_{s_i s_j} < \pi. \tag{5.1}$$

$$\rho_{s_i s_j} = \frac{\mathsf{E}\left[S_i S_j^*\right]}{\sqrt{\mathsf{E}\left[|S_i|^2\right]\mathsf{E}\left[|S_j|^2\right]}} = \left|\rho_{s_i s_j}\right| e^{i\theta_{s_i s_j}} \tag{5.2}$$

where q is the number of looks, and S_i & S_j are any two components of the scattering vector $\boldsymbol{k}_{\mathrm{FP}}^{\mathrm{sr}} = (S_{\mathrm{HH}}, \sqrt{2}S_{\mathrm{HV}}, S_{\mathrm{VV}})^T$. In fact, the multilook phase difference $\varphi_{s_i s_j}$ is the argument of an off-diagonal term from the polarimetric covariance matrix. Under the usual assumption that $\boldsymbol{k}_{\mathrm{FP}}^{\mathrm{sr}}$ has a complex Gaussian distribution, the PDF of the multilook phase difference is derived as [78]

$$\begin{aligned} p(\varphi_{s_i s_j}) = & \frac{\Gamma(q+1/2)\left(1-\left|\rho_{s_i s_j}\right|^2\right)^q \beta}{2\sqrt{\pi}\Gamma(q)\left(1-\beta^2\right)} \\ & + \frac{\left(1-\left|\rho_{s_i s_j}\right|^2\right)^q}{2\pi} F\left(q, 1; 1/2; \beta^2\right) \end{aligned} \tag{5.3}$$

where $\beta = \left|\rho_{s_i s_j}\right| \cos\left(\varphi_{s_i s_j} - \theta_{s_i s_j}\right)$, and $F\left(q, 1; 1/2; \beta^2\right)$ is a Gauss hypergeometric function. The above PDF depends only on the number of looks and the complex correlation coefficient. It is uniformly distributed over $(-\pi, \pi)$, when $\left|\rho_{s_i s_j}\right| = 0$, and it becomes a Dirac delta function when $\left|\rho_{s_i s_j}\right| = 1$.

5.4.1 *Extension to Hybrid, Compact, and Circular Polarimetry*

Let us consider a dual-pol scattering vector $\underline{\boldsymbol{k}}$ as

$$\underline{\boldsymbol{k}} = \begin{pmatrix} k_1 \\ k_2 \end{pmatrix} \tag{5.4}$$

$$\underline{\boldsymbol{k}} \in \left\{\boldsymbol{k}_{\text{DP3}}, \boldsymbol{k}_{\text{CL-pol}}, \boldsymbol{k}_{\pi/4}, \boldsymbol{k}_{\text{DCP}}\right\}.$$

Following the same line of thought, the complex correlation coefficient and multilook phase difference, related to linear, hybrid, compact, and circular dual-pol scattering vectors are defined as

$$\rho_c = \frac{\mathsf{E}\left[k_1 k_2^*\right]}{\sqrt{\mathsf{E}\left[\left|k_1\right|^2\right]\mathsf{E}\left[\left|k_2\right|^2\right]}} = \left|\rho_c\right| e^{i\theta} \tag{5.5}$$

$$\varphi = \text{Arg}\left(\frac{1}{q}\sum_{m=1}^{q} k_1[m] k_2^*[m]\right). \tag{5.6}$$

The hybrid, compact, and circular dual-pol scattering vectors are linear combinations of the elements of the scattering vector $\boldsymbol{k}_{\text{FP}}^{\text{sr}}$. Therefore, under the assumption that $\boldsymbol{k}_{\text{FP}}^{\text{sr}}$ has a complex Gaussian distribution, these scattering vectors are also distributed according to a complex Gaussian distribution.[1] Hence, the distribution of the hybrid, compact, and circular phase difference is the same as (5.3), parametrized by the corresponding correlation coefficient. Naturally, the shape of the phase difference PDF differs in each mode as a result of its great dependence on the complex correlation coefficient (which accepts different values in each mode). The latter is further studied using RADARSAT-2 data set of San Francisco Bay, CA, USA, and NASA/JPL AirSAR data set of Flevoland, The Netherlands.

Figure 5.14 shows the maps of the magnitude of the correlation coefficient in different dual-pol modes, over San Francisco Bay area. Figure 5.14(a) states a classic result that the correlation coefficient in traditional linear dual-pol mode (HH, VV) is strongly dependent upon the terrain characteristics. A visual inspection of the results in Fig. 5.14 suggests that the CL-pol and $\pi/4$ modes give correlation maps closely comparable to that of (HH,VV) with values strongly dependent upon the terrain type. On the other hand, we note that the correlation in the

[1] The family of normal distributions is closed under linear transformations.

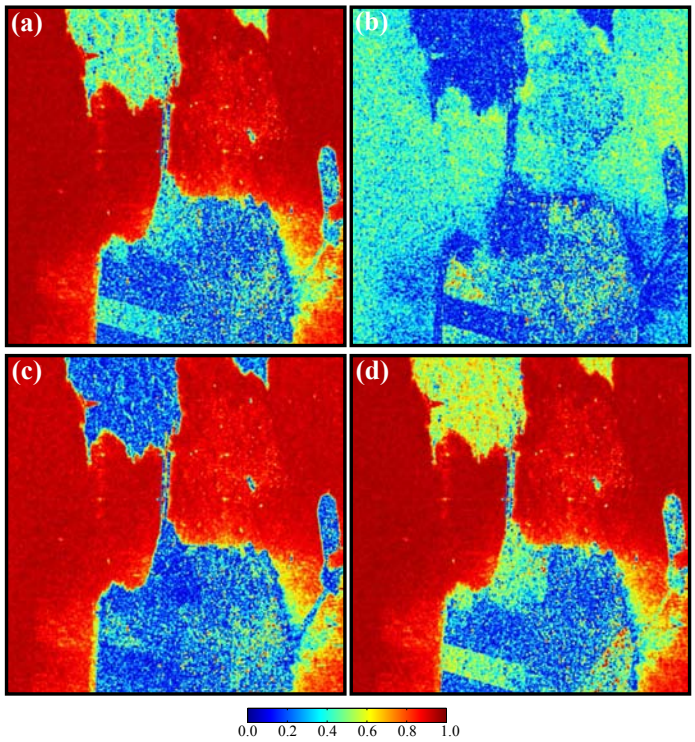

FIG. 5.14. Maps of the magnitude of the correlation coefficient in different dual-pol SAR modes, over San Francisco. (a) HH-VV (b) DCP. (c) CL-pol. (d) $\pi/4$.

DCP mode is less sensitive to the terrain characteristics. In (HH, VV), CL-pol, and $\pi/4$ modes the correlation is high in the ocean region (close to one), and low in the vegetation and urban areas. Also, the urban/vegetation contrast is greater in $\pi/4$ mode compared with CL-pol mode.

In order to study the PDFs of the phase difference, we select homogeneous regions of urban, vegetation and ocean, from San Francisco Bay data set. Figures 5.15, 5.16, and 5.17 show the experimental phase difference histograms (blue, circle markers) and their corresponding theoretical PDFs (red, solid line) in different dual-pol modes for ocean, park, and urban areas, respectively. There is a good agreement between the experimental histograms and the theoretical PDFs, notably for ocean and park areas. For the urban area, mismatches are observed due to the inevitable inhomogeneity in the selected region. As expected, the phase difference in (HH, VV) mode is directly related to the terrain type. These results suggest that the phase differences in hybrid and compact dual-pol modes are also directly related to the terrain characteristics; the $\pi/4$ mode exhibits the closest agreement with the classical (HH, VV) mode.

In a related study, Lee et al. [110] demonstrated the importance of the phase difference from (HH, VV) mode for crop classification. We conclude our analysis by studying the L-band AirSAR data of Flevoland,

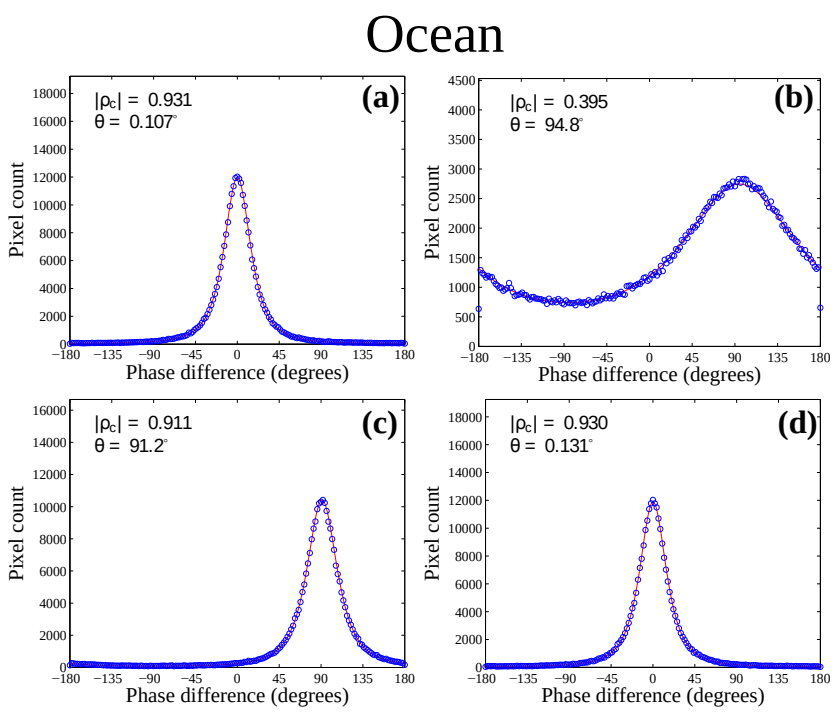

FIG. 5.15. Experimental histograms and theoretical PDFs of the phase difference in different dual-pol modes over the ocean region (San Francisco data set). (a) HH-VV (b) DCP. (c) CL-pol. (d) $\pi/4$.

The Netherlands, used for crop classification. Figure 5.18 shows the ground truth for this dataset, representing eleven classes. Figures 5.19 and 5.20 show the experimental histograms of the phase difference obtained for each class, in different dual-pol SAR modes. The results in Fig. 5.20 are obtained after applying a refined Lee filter [64] to the original data. These results suggest that the information captured in the phase difference for hybrid/compact, and circular dual-pol modes are comparable to that of the (HH, VV); with $\pi/4$ mode demonstrating the closest behavior to (HH, VV). Also DCP phase difference clearly distinguishes water from other classes; this is not the case in other modes. These results are of great interest for novel classification methods based on hybrid/compact, and circular dual-pol data.

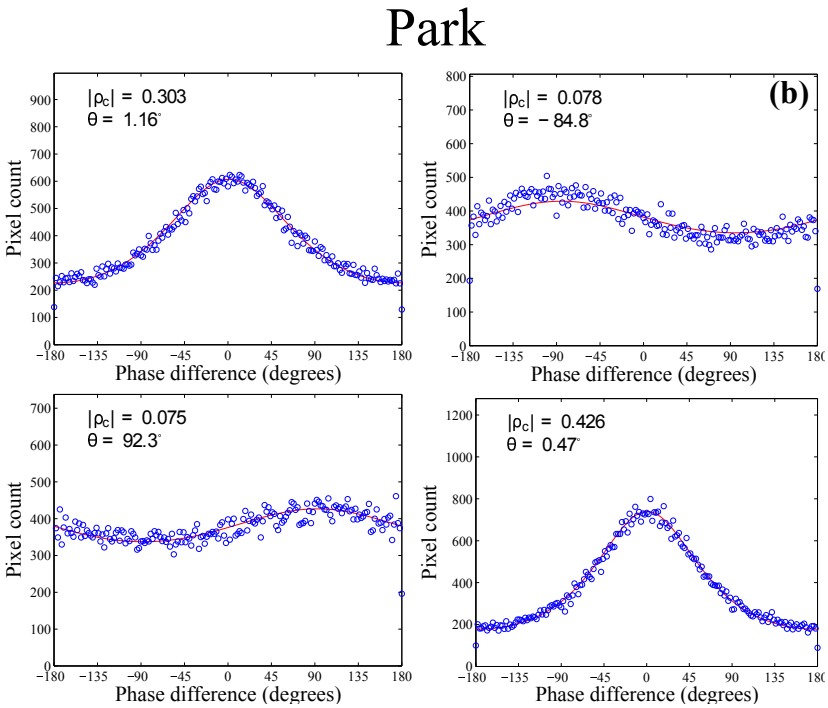

FIG. 5.16. Experimental histograms and theoretical PDFs of the phase difference in different dual-pol modes over the park region (San Francisco data set). (a) HH-VV (b) DCP. (c) CL-pol. (d) $\pi/4$.

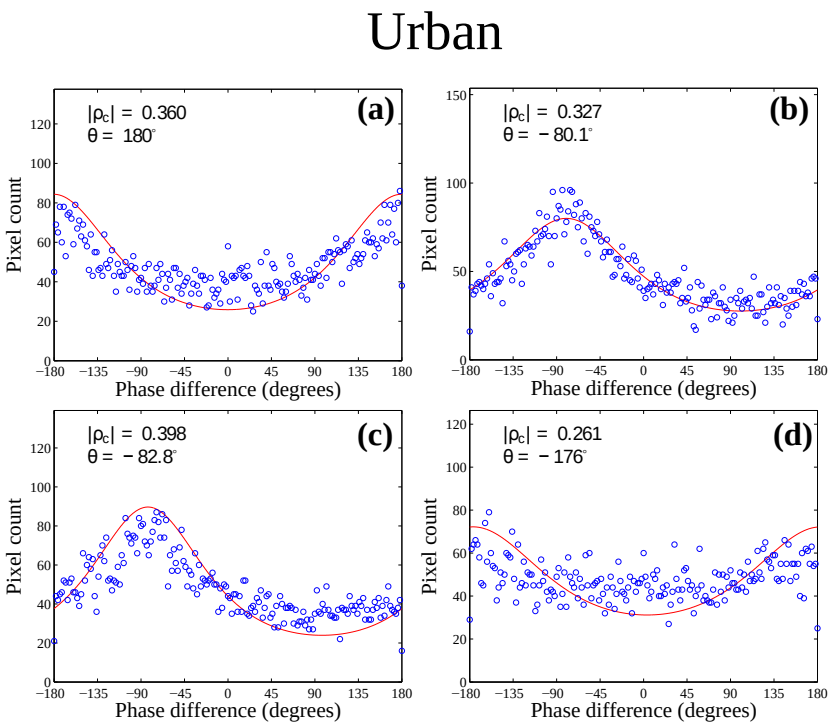

FIG. 5.17. Experimental histograms and theoretical PDFs of the phase difference in different dual-pol modes over the urban region (San Francisco data set). (a) HH-VV (b) DCP. (c) CL-pol. (d) $\pi/4$.

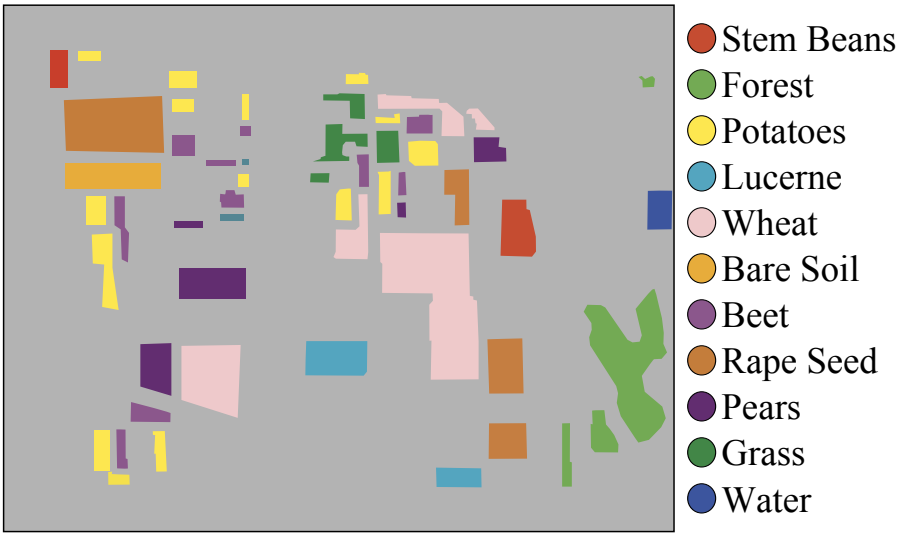

FIG. 5.18. Ground truth representing eleven classes for Flevoland data. The corresponding Google Earth and Pauli RGB images are shown in Fig. 2.6.

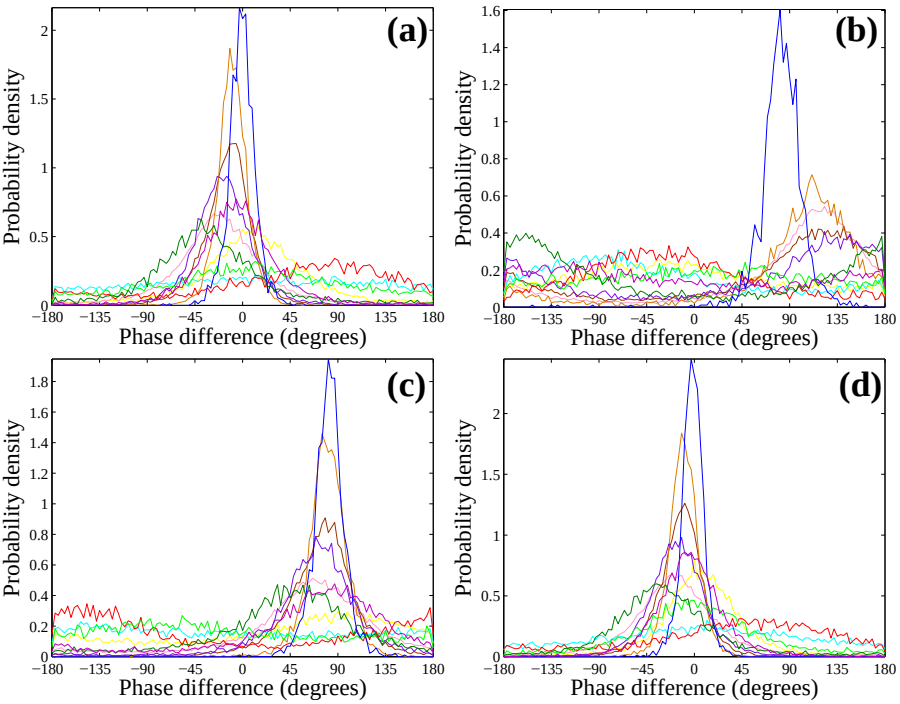

FIG. 5.19. Experimental histograms of the phase difference in different dual-pol SAR modes for eleven classes shown in Fig. 5.18. (a) HH-VV (b) DCP. (c) CL-pol. (d) $\pi/4$.

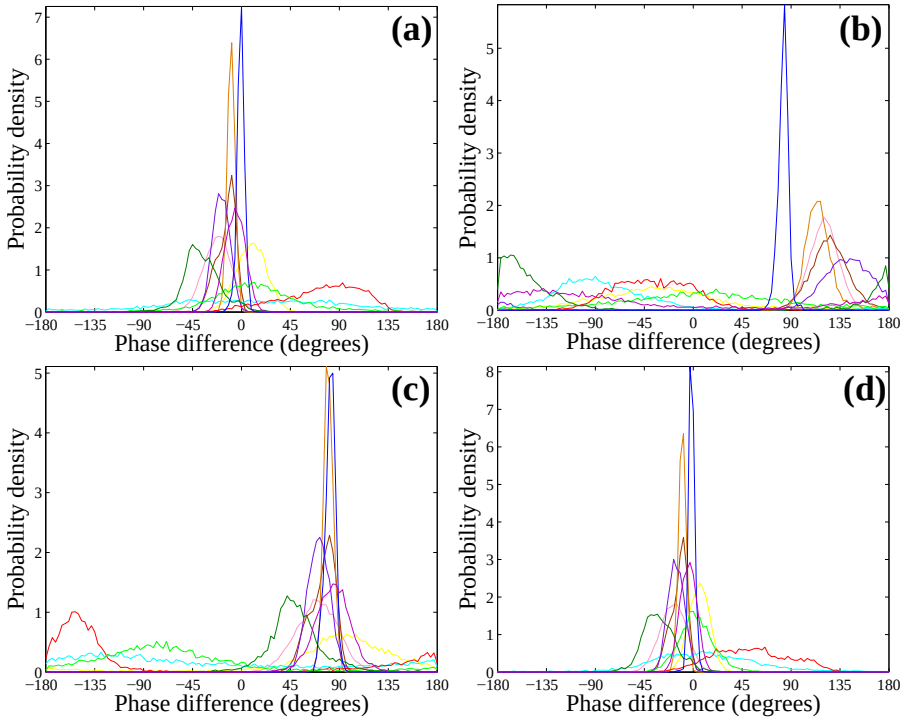

FIG. 5.20. Experimental histograms of the phase difference for eleven classes shown in Fig. 5.18, obtained after applying a refined Lee filter to the original data. (a) HH-VV (b) DCP. (c) CL-pol. (d) $\pi/4$.

5.5 POTENTIAL APPLICATIONS OUTSIDE THE GEOSCIENCE FIELD: POLARIZATION SENSITIVE OPTICAL COHERENCE TOMOGRAPHY

Tomographic techniques are widely used to generate slice images of three-dimensional objects. Tomographic techniques are of particular importance in the medical field, because these techniques can provide non-invasive diagnostic images. Optical Coherence Tomography (OCT) is a valuable imaging technology that produces high-resolution cross-sectional images of the internal microstructure of living tissue [123, 124]. OCT is of great interest for the medical community, because it provides tissue morphology imagery at much higher resolution (better than 10 μm) than other imaging systems such as Magnetic Resonance Imaging (MRI) or ultrasound. OCT may be compared with alternative techniques in terms of several different criteria: resolution, imaging depth, acquisition time, complexity, sample intrusiveness, etc. With regard to the first two, OCT occupies a niche represented in Fig. 5.21.

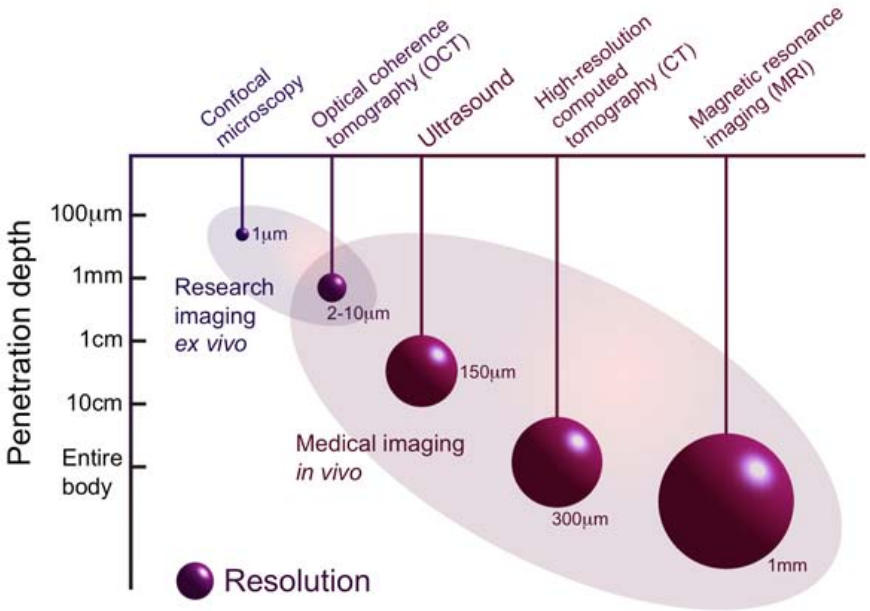

FIG. 5.21. Comparison of OCT resolution and imaging depths to those of alternative techniques [125].

Conventional OCT is based on the intensity of the backscattered light. However, intensity based images cannot directly differentiate between tissues. Polarization Sensitive Optical Coherence Tomography (PS-OCT) is a recent extension of OCT that provides information on the polarization states of the backscattered light, revealing properties of the tissue which are not available by conventional OCT. In fact, the light s polarization state can be changed by various light-tissue

interactions and thus it can be used to generate tissue-specific contrast. With PS-OCT, the sample is typically illuminated with totally polarized light states, and the backscattered light is detected in two orthogonal polarization channels. These measurements can provide the intensity elements of the Stokes vector, based on which a variety of parameters can be calculated, notably the DoP. Several studies have reported the changes in the DoP as a function of scattering property and tissue-specific parameters. Presently, the main applications of PS-OCT include retinal imaging, thermal damage, wound healing, and photo-aging assessment in skin, caries detection in dentistry, and diagnosis of cervical dysplasia [126–131].

The Stokes parameters of the light reflected from the sample can be computed in a PS-OCT system as [50, 132]

$$\mathbf{g} = \begin{pmatrix} g_0 \\ g_1 \\ g_2 \\ g_3 \end{pmatrix} = \begin{pmatrix} I_t \\ I_0 - I_{90} \\ I_{+45} - I_{-45} \\ I_{RC} - I_{LC} \end{pmatrix} \tag{5.7}$$

$$= \begin{pmatrix} \left\langle |E_{0H}|^2 + |E_{0V}|^2 \right\rangle \\ \left\langle |E_{0H}|^2 - |E_{0V}|^2 \right\rangle \\ \langle 2E_{0H}E_{0V}\cos(\varphi_{0H} - \varphi_{0V})\rangle \\ \langle 2E_{0H}E_{0V}\sin(\varphi_{0H} - \varphi_{0V})\rangle \end{pmatrix} \tag{5.8}$$

where E_{0H} and E_{0V} are the amplitudes, and φ_{0H} and φ_{0V} are the phases in the horizontal and vertical channels, respectively. Generally speaking, the elements of the Stokes vector are obtained as follows. The first two images g_0 and g_1 are obtained by analyzing the light backscattered by the scene in two orthogonal states of polarization. This is done by introducing a linear polarizer between the scene and the camera that is parallel or orthogonal to the incident light. The first element, $g_0 = I_t$, captures the total intensity of the beam. The third intensity g_2 is obtained by modifying the orientation of the polarizer and recording the backscattered light in the directions oriented at $45^\circ$and $-45^\circ$from the incident light. The last image g_3 is obtained by adding quarter-wave plates before the polarizer, which introduce a phase difference of $\lambda/4$, and generating circularly polarized light to the sample.

On major axis of the research in PS-OCT systems is the study and assessment of the information provided by the DoP, and its sister parameters,[1] for tissue-specific detection and classification applications [130, 133]. Figures 5.22 and 5.23 show two examples of intensity data and the corresponding degree of polarization uniformity (defined in § 1.2) derived from PS-OCT data. Figure 5.22 corresponds to a

[1] Such as the degree of polarization uniformity, and the degree of circular polarization (see § 1.2).

healthy human retina whereas Fig. 5.23 corresponds to a patient with a choroidal nevus (a benign tumor is outlined). This figure clearly shows a strong depolarization in the area of interest. These results have been recently reported by Götzinger et al. [133], demonstrating the valuable information provided by the DoP and its sister parameters.

However, to our knowledge, no comprehensive study has been performed addressing the effects of the choice of the emission polarization on the detection and classification results. This has led to different versions of PS-OCT with potentially suboptimal transmit and receive polarizations. We believe that our studies presented in this dissertation can be straightforwardly extended to PS-OCT systems, especially considering the strong physical and mathematical bounds between the two fields. This is an interesting topic to be addressed in depth by specialists in future work.

5.6 CONCLUSION

In this chapter, ML and MoM estimators of the DoP based on two intensity images were studied in hybrid/compact and linear dual-pol SAR modes. The performance of these estimators was evaluated using both synthetic and real PolSAR data, over various terrain types such as urban, vegetation, and ocean. An important conclusion was reached; classical dual-pol modes, i.e., (HH, HV) and (VH,VV), performed better than emerging hybrid and compact dual-pol modes in terms of the estimation of the DoP based on only two intensity images. In other words, the information captured by the amplitude part of the classical dual-pol SAR data is far richer than that captured by the amplitude of the hybrid and compact modes. Experimental results also suggest that ML estimators outperform MoM estimators over different terrain types. Moreover, these estimators deliver better performance in ocean and urban regions (higher DoP) compared to vegetation areas (lower DoP). The developed DoP estimators are of interest in different applications of linear and hybrid/compact dual-pol SAR data, such as image segmentation and object detection.

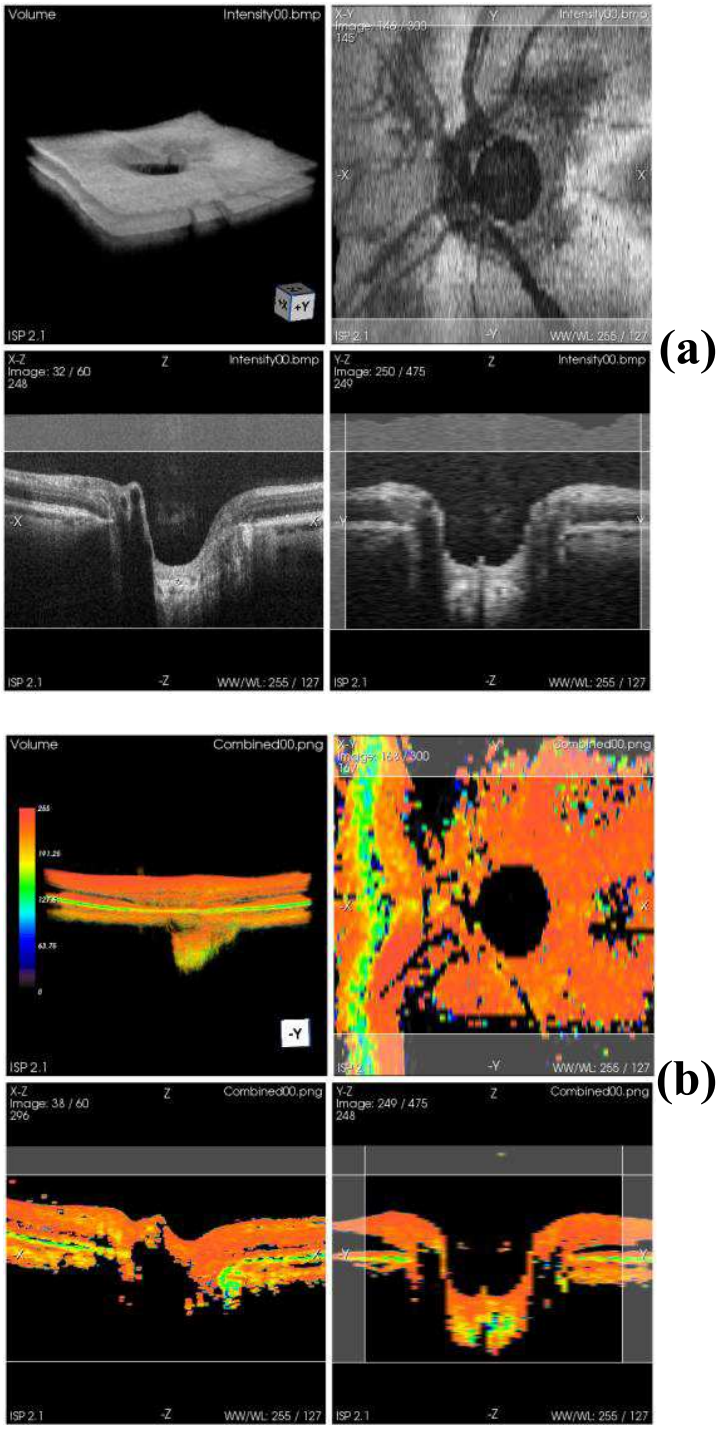

FIG. 5.22. PS-OCT dataset of healthy human retina in the nerve head area. (a) Intensity [logarithmic gray scale] (b) Degree of polarization uniformity (color bar: 0 = 0, 255 = 1). Each figure shows a snapshot consisting of 4 images arranged as follows: top left, volume rendering; top right, x-y cross section; bottom left, x-z cross section; bottom right, y-z cross section. Image size: $14.25^{\circ}(x) \times 15^{\circ}(y) \times 1.8$ mm (z, in air). Courtesy of Götzinger et al. [133]

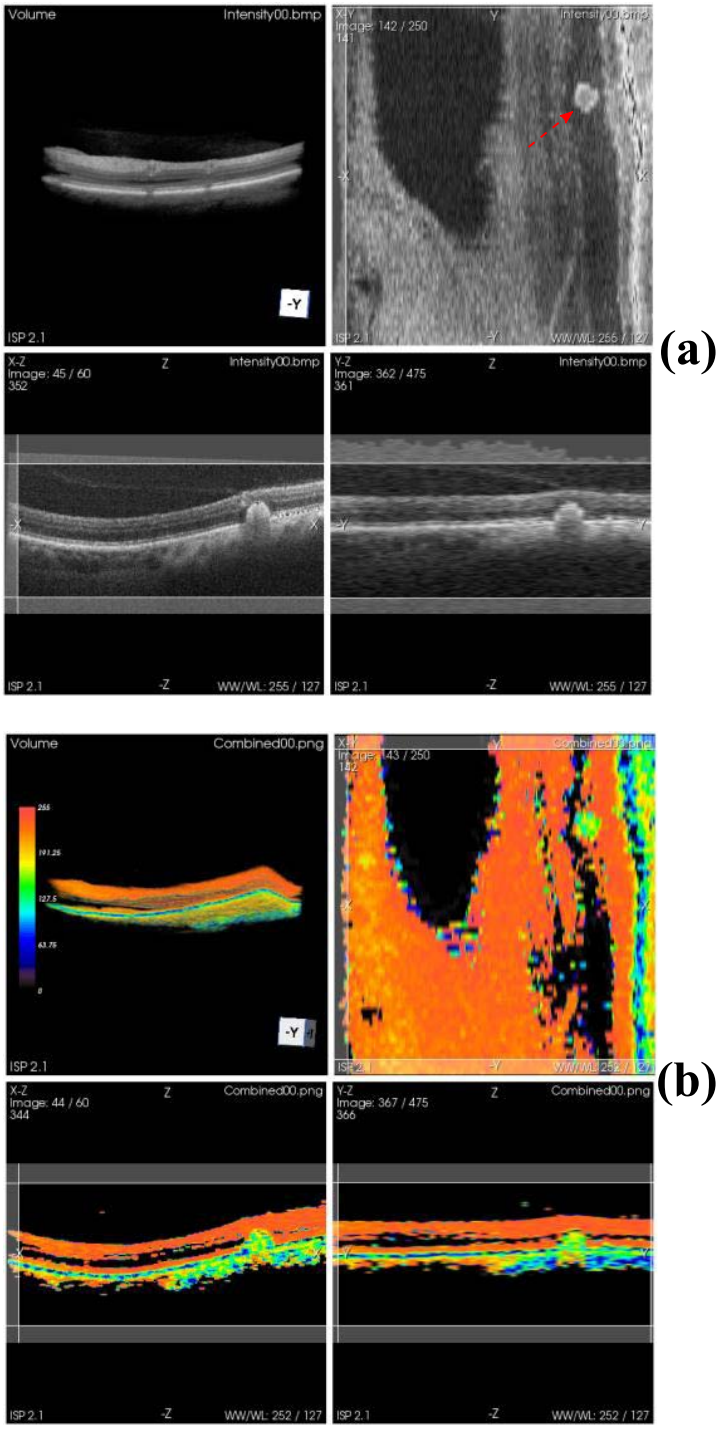

FIG. 5.23. PS-OCT dataset of a patient with a choroidal nevus. A benign tumor is outlined. (a) Intensity [logarithmic gray scale] (b) Degree of polarization uniformity (color bar: 0 = 0, 255 = 1). Each figure shows a snapshot consisting of 4 images arranged as follows: top left, volume rendering; top right, x-y cross section; bottom left, x-z cross section; bottom right, y-z cross section. Image size: 14.25°(x) × 15°(y) × 1.8 mm (z, in air). Courtesy of Götzinger et al. [133]

CONCLUSION

In this dissertation, we have studied the performance of compact, hybrid and linear dual-pol SAR modes in terms of the estimation of the DoP for a variety of geoscience applications. The initial objective of the thesis was to perform a statistical analysis of dual-pol SAR data, notably for the multi-look dual-pol intensity images. Our approach was based on novel and solid mathematical concepts which had been developed independently of PolSAR context. This goal has been fulfilled with the derivation of the joint distribution of multi-look PolSAR intensity images, proven to be MGDs. These distributions were then further studied for particular cases of interest, such as coherent and incoherent dual-pol SAR systems.

Once we gained access to the statistical properties of PolSAR data, the next challenge was to develop efficient estimators of a physically related discriminator, capable of providing insight to the information content of dual-pol SAR data. Our approach was to exploit directly the information of the dual-pol SAR data, and develop near real-time algorithms in the context of maritime monitoring and surveillance, notably vessel detection and oil-spill observation. For this purpose, we chose the DoP as our main discriminator.

When this thesis initiated in 2008, the introduction of hybrid and compact dual-pol SAR modes had just revived an active discussion in the PolSAR society with regard to classical, unquestioned canonical (H and V) polarizations as well as the trade-off between dual-pol and full-pol SAR imagery. In this framework, and based on the derived statistical characteristics, we addressed the estimation of the DoP for both classical and emerging dual-pol SAR modes. We further extended this concept to the challenging case of incoherent dual-pol SAR systems where only two intensity images are available. Two categories of DoP estimators were derived; ML and MoM estimators.

Equipped with efficient DoP estimators, we started to investigate in detail the information content of the complex and intensity data provided by different hybrid, compact and linear dual-pol SAR modes, in order to assess the relative performance of these modes in a variety of applications. The work carried out in this thesis has shown that the DoP is a very efficient discriminator for vessel detection and oil-spill recognition with a particularly low computational complexity, and high versatility. Moreover, we have shown that the complex

compact/hybrid PolSAR data perform better than the classical (linear) dual-pol modes for the detection of vessels and oil-spills over a wide range of incident angles and ocean conditions. Interestingly, the compact/hybrid results are also closely comparable to the recent full-pol methods promoted by NASA/JPL researchers in the oil-spill detection context. Similarly, in the ship detection context, the DoP in these modes performs nearly as well as recent full-pol notch filter algorithms promoted in recent publications.

In incoherent dual-pol SAR systems, on the other hand, the above conclusion is inverted; the classical linear dual-pol modes perform far better than the emerging hybrid and compact modes when we only have access to the amplitude of dual-pol SAR data. We have studied this matter in detail using both the ML and MoM estimators, over different train types, such as vegetation, urban, and ocean. We have also compared these results with other publications and suggested a consistent explanation.

Our research in this thesis confirms that compact, and hybrid polarimetry are not a substitute of full-polarimetry, but a beneficial approach compared to classical dual-pol modes in a number of applications, such as vessel and oil-spill detection. On the other hand, the classical dual-pol modes capture much more information in their amplitude (intensity) data, compared with hybrid/compact amplitude data. In other words, compared to classical dual-pol phase, hybrid/-compact relative phase carries crucial information directly responsible for the over-all performance of these modes. This is of major importance, notably with regard to system aspects, sensitivity to relative errors, and phase calibration.

The conducted research is not limited to geoscience applications. In particular, our results are of interest in medical applications involved with the Polarization Sensitive Optical Coherence Tomography (PS-OCT). On major axis of the research in PS-OCT systems is the study and assessment of the information provided by the DoP for tissue-specific detection and classification applications. However, to our knowledge, no comprehensive study has been performed addressing the effects of the choice of the emission polarization on the detection and classification results. We argue that the studies presented in this dissertation can be straightforwardly extended to PS-OCT systems. This is an interesting topic to be addressed in depth by specialists in future work.

Appendices

A

ENVIRONMENTAL CONDITIONS, BRAGG SCATTERING & OIL SLICKS

The backscatter energy detected by a SAR depends primarily on the ocean surface roughness through the capillary and small gravity waves generated by the local winds. In general, lower wind speeds generate fewer Bragg waves, and thus, a smoother ocean surface which appears in SAR images as areas with a relatively low Normalized Radar Cross Section (NRCS) [86]. Naturally, below a low wind speed threshold, the NRCS values are so low that features dependent on the Bragg waves are not visible in the SAR images.

According to the Bragg model the radar microwaves are in resonance with ocean waves of similar scale [89]. Therefore, the wavelength of the Bragg waves and the observed backscatter energy are function of the radar wavelength. In other words, depending on the scale of the process and the wind conditions, images obtained at one radar wavelength may strongly show a low-backscatter feature in a scene while images obtained at another wavelength may not [134]. For example, SAR L-band sensors are sensitive to processes that modulate surface waves at the decimeter scale while C-band SAR sensors are sensitive to centimeter-scale Bragg waves.

Slicks are particular ocean features that can be observed in SAR images. Slicks are contiguous areas in which Bragg scattering at wavelength scale of $\sim$0.01 to 0.1 m is suppressed either by layers of oil, biological surfactants, or organic surface films [105, 135, 136]. Bragg scattering theory has been widely used in different maritime applications (see [137, 138] and references therein.). The influence of surface oil on ocean backscatter has been extensively studied using radar data in the publications of Krishen [84], Singh et al. [85], Alpers and Hühnerfuss [86], Wismann et al. [87], Fingas and Brown [88]. It is widely acknowledged that SAR returns from the ocean sur-

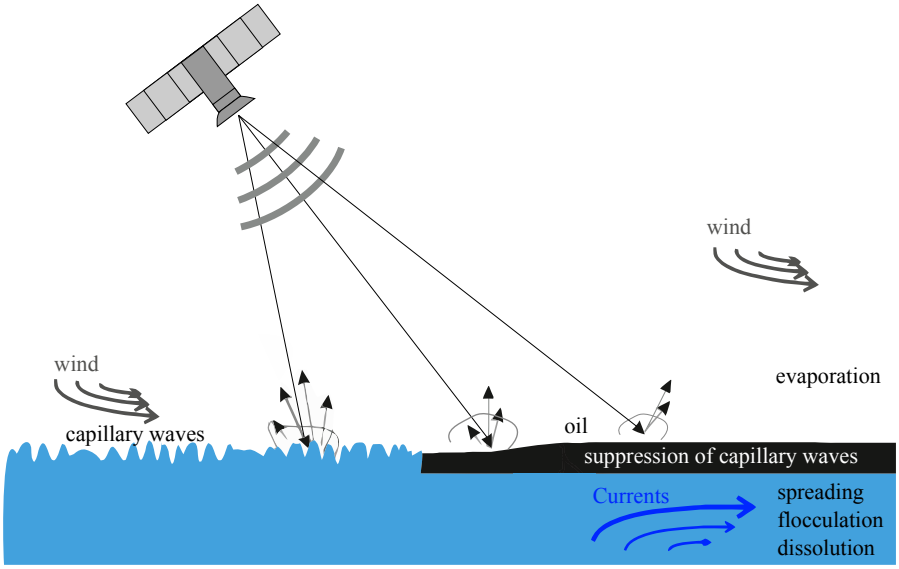

FIG. A.1. The Bragg scattering (left) and the floating oil layer (right) affecting the SAR backscatter energy (inspired by [139]).

face depend on different parameters, notably the wavelength of small surface waves (0.7 to 10 cm), the radar electromagnetic wavelength, and the incidence angle of the radar energy. As shown in Fig. A.1, when sea surface capillary waves are damped by the presence of a thin layer of oil ($\sim$0.1 μm), a larger proportion of radar energy is reflected away from the satellite. As a result, oil regions on the SAR images appear as dark patches within the ocean clutter. The persistence of surfactant layers is affected by processes like evaporation, wind, surface currents, photolysis, spreading, flocculation, and dissolution [139]. Figure A.2 shows the SAR backscatter dependency to wind speed for three distinct cases of strong, medium, and low wind speeds; medium winds (3–7 m/s) produce the ideal sea state for SAR oil-spill detection. On the other hand, low winds decrease the SAR ability to detect the oil-spills and turbulent waters (strong winds) break the oil layers and intensify the mixing process.

SAR incidence angle and look direction with respect to the wind are also of crucial importance for oil-spill detection. Sea surface backscatter decreases rapidly with increasing radar incidence angle. As a consequence, SAR images are generally brighter in the near range and darker in the far range (refer to Fig. 2.8). Success in detecting low-backscatter ocean features may therefore greatly depend on the location of the features within a scene swath. Location is of particular importance in SAR systems that cover a wide range width and incidence angles, such as UAVSAR (25°–65°). As to the wind direction, a crosswind (wind blowing perpendicular to the range direction) is known to produce lower backscatter energy than an upwind or downwind (wind blowing along the range direction) [134].

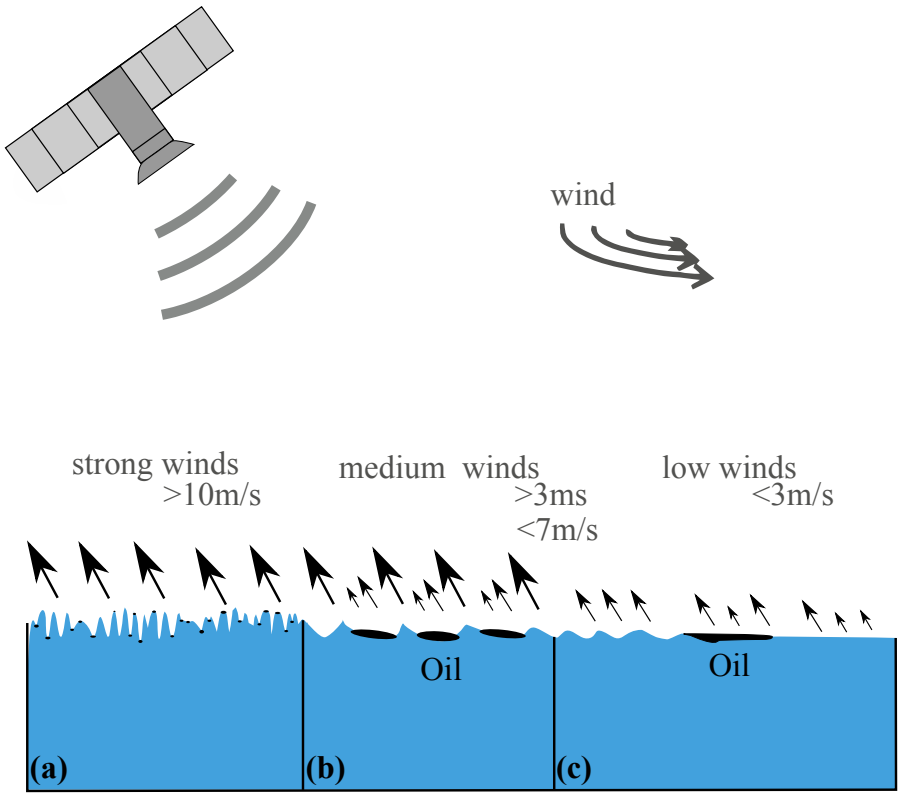

FIG. A.2. SAR backscatter dependency to wind speed and sea state. (a) Strong winds; turbulent waters break the oil layers and increase the mixing process. (b) Medium winds; ideal for oil-spill detection. (c) Low winds; low ability of SAR for oil-spill detection [139].

B

UAVSAR NOISE FLOOR

A central parameter for SAR instruments is the minimal detectable reflected signal from the surface. This is characterized by radar s Noise Equivalent Sigma Zero (NESZ). Noise in a radar resolution element has two components, additive and multiplicative; it also depends on a variety of parameters including the transmitted power, antenna gain, losses in the system, and operating temperature. NESZ is a measure of the sensitivity of the system to areas of low radar backscatter. It is given by the value of the backscatter coefficient (sigma-zero) corresponding to a signal-to-noise ratio of unity.

Figure B.1 shows the NESZ for the UAVSAR L-band sensor as a function of range [27]; it is -53 dB at the point of maximal antenna gain and degrades to -40 dB in the near and far range (-35 dB at the far swath limit). Table. B.1 provides a comparison of different SAR systems in terms of their NESZ. A typical radar-dark surface with L band backscatter value of -30 dB has a signal-to-noise ratio in excess of 10 dB over most of the swath for UAVSAR, but would be near or below the noise floor in the other related systems. Hence, the low noise floor of UAVSAR provides a unique capability to assess backscatter information at levels not available with other radars.

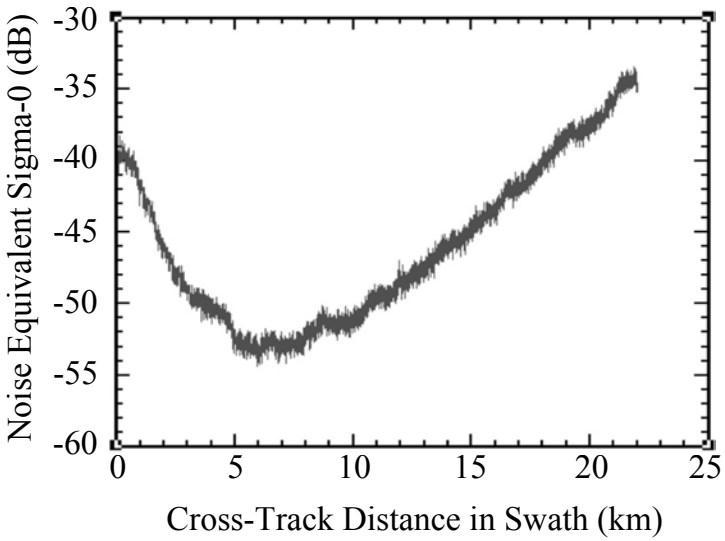

FIG. B.1. Noise equivalent sigma-zero of the UAVSAR L-band radar [27].

TABLE B.1. Comparison of noise floor in SAR instruments.

Sensor	Noise Equivalent Sigma-Zero (dB)
UAVSAR	-35 to -53 [27]
ERS1/2	-20 to -29 [37]
RADARSAT-2	-29 [75]
ENVISAT-ASAR	-20 to -29 [37]
ALOS-PALSAR	Avg. -23 (HH or VV) -26 (HV) [140]
TerraSAR-X	Avg. -23 [141]
AIRSAR	-34 to -50 (L) -40 to -48 (P) -26 to -34 (C) [30]

BIBLIOGRAPHY

[1] Wiener, N., "Generalized harmonic analysis," *Acta Math.*, vol. 55, pp. 117–258, 1930.

[2] Cohen, M. H., "Radio astronomy polarization measurements," *Proc. of the IRE*, vol. 46, no. 1, pp. 172–183, Jan. 1958.

[3] Fritz, J. P. and Chandrasekar, V., "Simultaneous observations and analysis of severe storms using polarimetric X-band SAR and ground-based weather radar," *IEEE Trans. Geosci. Remote Sens.*, vol. 48, no. 10, pp. 3622–3637, Oct. 2010.

[4] Galletti, M., Bebbington, D. H. O., Chandra, M., and Borner, T., "Measurement and characterization of entropy and degree of polarization of weather radar targets," *IEEE Trans. Geosci. Remote Sens.*, vol. 46, no. 10, pp. 3196–3207, Oct. 2008.

[5] Touzi, R., Deschamps, A., and Rother, G., "Phase of target scattering for wetland characterization using polarimetric C-band SAR," *IEEE Trans. Geosci. Remote Sens.*, vol. 47, no. 9, pp. 3241–3261, Sep. 2009.

[6] Toan, T. L., Beaudoin, A., Riom, J., and Guyon, D., "Relating forest biomass to SAR data," *IEEE Trans. Geosci. Remote Sens.*, vol. 30, no. 2, pp. 403–411, Mar. 1992.

[7] Migliaccio, M., Gambardella, A., Nunziata, F., Shimada, M., and Isoguchi, O., "The PALSAR polarimetric mode for sea oil slick observation," *IEEE Trans. Geosci. Remote Sens.*, vol. 47, no. 12, pp. 4032–4041, Dec. 2009.

[8] Wolff, L. B., "Polarization camera for computer vision with a beam splitter," *J. Opt. Soc. Am. A*, vol. 11, no. 11, Nov. 1994.

[9] Jacques, S. L., Ramella-Roman, J. C., and Lee, K., "Imaging skin pathology with polarized light," *Journal of Biomedical Optics*, vol. 7, no. 3, pp. 329–340, 2002.

[10] Souyris, J.-C., Imbo, P., Fjortoft, R., Mingot, S., and Lee, J.-S., "Compact polarimetry based on symmetry properties of geophysical media: the $\pi/4$ mode," *IEEE Trans. Geosci. Remote Sens.*, vol. 43, no. 3, pp. 634–646, Mar. 2005.

[11] Souyris, J.-C. and Mingot, S., "Polarimetry based on one transmitting and two receiving polarizations: the $\pi/4$ mode," in *Proceedings of the 2002 IEEE International Geoscience and Remote*

Sensing Symposium (IGARSS 02), vol. 1, Jun. 2002, pp. 629–631 vol.1.

[12] Stacy, N. and Preiss, M., "Compact polarimetric analysis of X-band SAR data," in *Proc. of EUSAR 06*, Germany, May 2006.

[13] Raney, R. K., "Hybrid-polarity SAR architecture," *IEEE Trans. Geosci. Remote Sens.*, vol. 45, no. 11, Nov. 2007.

[14] Nord, M. E., Ainsworth, T. L., Lee, J.-S., and Stacy, N. J. S., "Comparison of compact polarimetric synthetic aperture radar modes," *IEEE Trans. Geosci. Remote Sens.*, vol. 47, no. 1, pp. 174–188, Jan. 2009.

[15] Cloude, S. R., "Dual- versus quad-pol: a new test statistic for radar polarimetry," in *Proc. of POLinSAR 09*, Frascati, Italy, 26–30 Jan. 2009.

[16] Freeman, A., Dubois-Fernandez, P., and Truong-Loi, M.-L., "Compact polarimetry at longer wavelengths — calibration," in *Proc. of EUSAR 8*, Friedrichshafen, Germany, Jun. 2008, pp. 1–4.

[17] Dubois-Fernandez, P., Angelliaume, S., Truong-Loi, M.-L., and Souyris, J.-C., "Compact polarimetry mode for a low frequency SAR in space," in *Proc. of IGARSS 08*, vol. 5, Jul. 2008, pp. V –279 –V –282.

[18] Cloude, S. R., "The dual polarisation entropy/alpha decomposition: A PALSAR case study," in *Proc. of POLinSAR 07*, Frascati, Italy, Jan. 2007.

[19] Touzi, R., "Compact-hybrid versus linear- dual and fully polarimetric SAR," in *Proc. of POLinSAR 09*, Frascati, Italy, Jan. 2009.

[20] Pottier, E., "SAR polarimetry and its applications for remote sensing analysis," *UAF ASF Tutorial Workshop on Radar Polarimetry*, 10–12 Aug. 2010, Fairbanks, Alaska.

[21] Truong-Loï, M.-L., Dubois-Fernandez, P., and Pottier, E., "Compact polarimetry potentials," in *Proc. of IGARSS 11*, Jul. 2011, pp. 3823–3826.

[22] Chairpersons, S., "Summaries and recommendations of the POLinSAR 2009 workshop," in *Proc. of POLinSAR 09*, Frascati, Italy, Jan. 2009.

[23] [Online] URL: http://www.asc-csa.gc.ca/eng/satellites/radarsat/ (last accessed September 2012).

[24] Raney, R. K., "DESDynI adopts hybrid polarity SAR architecture," in *IEEE Radar Conference*, May 2009, pp. 1–4.

[25] [Online] URL: www.conae.gov.ar (last accessed September 2012).

[26] [Online] URL: http://www.jaxa.jp/projects/sat/alos2/index_e.html (last accessed September 2012).

[27] Jones, C., Minchew, B., and Holt, B., "Polarimetric decomposition analysis of the Deepwater Horizon oil slick using L-band UAVSAR data," in *Proc. of IGARSS 11*, Vancouver, CA, Jul. 2011, pp. 2278–2281.

[28] Marino, A., Walker, N., and Woodhouse, I., "Ship detection using SAR polarimetry. the development of a new algorithm designed to exploit new satellite SAR capabilities for maritime surveillance." in *Proc. of SeaSAR 10*, Rome, Italy, Jan. 2010.

[29] ——, "Ship detection with RADARSAT-2 quad-pol SAR data using a notch filter based on perturbation analysis," in *Proc. of IGARSS 10*, Honolulu, Hawaii, USA, Jul. 2010, pp. 3704 – 3707.

[30] [Online] URL: http://airsar.jpl.nasa.gov (last accessed September 2012).

[31] Lou, Y., "Review of the NASA/JPL airborne synthetic aperture radar system," in *Proceedings of the 2002 IEEE International Geoscience and Remote Sensing Symposium (IGARSS 02)*, vol. 3, Jun. 2002, pp. 1702–1704.

[32] Taylor, V. B., "CYCLOPS: The JPL AIRSAR synoptic processor," in *Proc. of IGARSS 92*, Houston, TX, May 1992, pp. 652 –654.

[33] [Online] URL: http://uavsar.jpl.nasa.gov (last accessed September 2012).

[34] Rosen, P. A., Hensley, S., Wheeler, K., Sadowy, G., Miller, T., Shaffer, S., Muellerschoen, R., Jones, C., Zebker, H., and Madsen, S., "UAVSAR: a new NASA airborne SAR system for science and technology research," in *IEEE Conference on Radar*, Apr. 2006, p. 8.

[35] [Online] URL: http://southport.jpl.nasa.gov/sir-c (last accessed September 2012).

[36] Stofan, E. R., Evans, D. L., Schmullius, C., Holt, B., Plaut, J. J., van Zyl, J., Wall, S. D., and Way, J., "Overview of results of spaceborne imaging radar-C, X-band synthetic aperture radar (SIR-C/X-SAR)," *IEEE Trans. Geosci. Remote Sens.*, vol. 33, no. 4, pp. 817–828, Jul. 1995.

[37] [Online] URL: http://envisat.esa.int (last accessed September 2012).

[38] [Online] URL: http://www.eorc.jaxa.jp/ALOS/en/ (last accessed September 2012).

[39] [Online] URL: http://www.asc-csa.gc.ca/eng/satellites/radarsat2/ (last accessed September 2012).

[40] [Online] URL: http://www.radarsat2.info (last accessed September 2012).

[41] [Online] URL: http://www.astrium-geo.com/terrasar-x/ (last accessed September 2012).

[42] Snoeij, P., Attema, E., Davidson, M., Duesmann, B., Floury, N., Levrini, G., Rommen, B., and Rosich, B., "Sentinel-1 radar mission: Status and performance," *IEEE Aerospace and Electronic Systems Magazine*, vol. 25, no. 8, pp. 32–39, Aug. 2010.

[43] Jones, R. C., "A new calculus for the treatment of optical systems," *J. Opt. Soc. Am.*, vol. 31, no. 7, pp. 488–493, Jul. 1941.

[44] Wolf, E., "Coherence properties of partially polarized electromagnetic radiation," *Nuovo Cim.*, vol. 13, no. 6, pp. 1165–1181, Sep. 1959.

[45] Stokes, G. G., "On the composition and resolution of streams of polarized light from different sources," *Trans. Camb. Philosoph. Soc.*, vol. 9, pp. 399–416, 1852.

[46] Green Jr, P. E., "Radar measurements of target scattering properties," in *Radar astronomy*, Evans, J. V. and Hagfors, T., Eds. New York: McGraw-Hill, 1968, pp. 1–78.

[47] Huynen, J. R., "Phenomenological theory of radar targets," Ph.D. dissertation, University of Technology, Delft, The Netherlands, Dec. 1970.

[48] Jones, R. C., "A new calculus for the treatment of optical systems: a more general formulation and description of another calculus," *J. Opt. Soc. Am.*, vol. 37, no. 2, pp. 107–110, 1947.

[49] Born, M., Wolf, E., and Bhatia, A. B., *Principles of optics: electromagnetic theory of propagation, interference and diffraction of light*. Cambridge University Press, 1999.

[50] Brosseau, C., *Fundamentals of Polarized Light: A Statistical Optics Approach*. John Wiley and Sons, 1998.

[51] Guissard, A., "Mueller and Kennaugh matrices in radar polarimetry," *IEEE Trans. Geosci. Remote Sens.*, vol. 32, no. 3, pp. 590–597, May 1994.

[52] Lee, J.-S. and Pottier, E., *Polarimetric Radar Imaging: From Basics to Applications*. CRC Press, 2009.

[53] Boerner, W. M. and et al. (Eds.), "Inverse methods in electromagnetic imaging," in *the NATO-Advanced Research Workshop*, Bad Windsheim, FR Germany, Sep. 1983, parts 1&2, NATO-ASI C-143, D. Reidel Publ. Co., Jan. 1985.

[54] Nghiem, S. V., Yueh, S. H., Kwok, R., and Li, F. K., "Symmetry properties in polarimetric remote sensing," *Radio Science*, vol. 27, pp. 693–711, Oct. 1992.

[55] Kostinski, A. B. and Boerner, W. M., "On foundations of radar polarimetry," *IEEE Transactions on Antennas and Propagation*, vol. 34, pp. 1395–1404, 1986.

[56] Goodman, J. W., *Statistical Optics*. New York: Wiley, 1985.

[57] ——, "Some fundamental properties of speckle," *J. Opt. Soc. Am.*, vol. 66, no. 11, pp. 1145–1150, 1976.

[58] Durand, J. M., Gimonet, B., and Perbos, J., "SAR data filtering for classification," *IEEE Trans. Geosci. Remote Sens.*, vol. GE-25, pp. 629–637, 1987.

[59] Raney, R. K., "Radar fundamentals: Technical perspective," in *Principles and Applications of Imaging Radar, Manual of Remote Sensing*, 3rd ed. Toronto: ASPRS, John Wiley and Sons Inc., 1998, vol. 2, ch. 2.

[60] Goodman, J. W., "Statistical properties of laser speckle patterns," in *Laser Speckle and Related Phenomena*, J. C. Dainty, Ed. Springer Berlin / Heidelberg, 1975.

[61] Wehner, D. R., *High resolution radar*. Artech House, 1987.

[62] Gagnon, L. and Jouan, A., "Speckle filtering of sar images - a comparative study between complex-wavelet-based and standard filters," *SPIE Proc.*, vol. 3169, pp. 80–91, 1997.

[63] Lee, J.-S., "Digital image enhancement and noise filtering by use of local statistics," *IEEE Trans. Pattern Anal. Mach. Intell.*, vol. PAMI-2, no. 2, pp. 165–168, Mar. 1980.

[64] ——, "Refined filtering of image noise using local statistics," *Computer Graphics and Image Processing*, vol. 15, no. 4, pp. 380–389, 1981.

[65] Kuan, D. T., Sawchuk, A. A., Strand, T. C., and Chavel, P., "Adaptive noise smoothing filter for images with signal-dependent noise," *IEEE Trans. Pattern Anal. Mach. Intell.*, vol. PAMI-7, no. 2, pp. 165–177, Mar. 1985.

[66] Frost, V. S., Stiles, J. A., Shanmugan, K. S., and Holtzman, J. C., "A model for radar images and its application to adaptive digital filtering of multiplicative noise," *IEEE Trans. Pattern Anal. Mach. Intell.*, no. 2, pp. 157–166, Mar. 1982.

[67] Tso, B. and Mather, P. M., *Classi cation Methods for Remotely Sensed Data*. CRC Press, 2009.

[68] Goodman, N. R., "Statistical analysis based on a certain multivariate complex gaussian distribution (an introduction)," *Ann. Math. Statist.*, vol. 34, no. 1, pp. 152–177, 1963.

[69] Bernardoff, P., "Which multivariate gamma distributions are infinitely divisible?" *Bernoulli*, vol. 12, no. 1, 2006.

[70] Letac, G. and Wesolowski, J., "Laplace transforms which are negative powers of quadratic polynomials," *Transactions of the American Mathematical Society*, vol. 360, no. 12, pp. 6475–6496, Dec. 2008.

[71] Chatelain, F., Tourneret, J.-Y., Inglada, J., and Ferrari, A., "Bivariate gamma distributions for image registration and change detection," *IEEE Trans. Image Process.*, vol. 16, no. 7, pp. 1796–1806, Jul. 2007.

[72] Abramowitz, M. and Stegun, I. A., *Handbook of mathematical functions*. New York: Dover, 1965.

[73] Raney, R. K. and Freeman, A., "Hybrid-polarity SAR architecture," in *Proc. of POLinSAR 09*, Frascati, Italy, Jan. 2009.

[74] Ulaby, F. T. and Elachi, C., *Radar Polarimetry for Geoscience Applications*. Artech House, 1990.

[75] MDA, *RADARSAT-2 Product Description*, MacDonald, Dettwiler Associates Ltd., Richmond, BC, Canada, issue 1/7, RN-SP-52-1238, 2009.

[76] Anfinsen, S. N., Doulgeris, A. P., and Eltoft, T., "Estimation of the equivalent number of looks in polarimetric synthetic aperture radar imagery," *IEEE Trans. Geosci. Remote Sens.*, vol. 47, no. 11, pp. 3795 –3809, Nov. 2009.

[77] Touzi, R. and Lopes, A., "Statistics of the stokes parameters and of the complex coherence parameters in one-look and multilook speckle fields," *IEEE Trans. Geosci. Remote Sens.*, vol. 34, no. 2, pp. 519–531, Mar. 1996.

[78] Lee, J.-S., Hoppel, K. W., Mango, S. A., and Miller, A. R., "Intensity and phase statistics of multilook polarimetric and interferometric SAR imagery," *IEEE Trans. Geosci. Remote Sens.*, vol. 32, no. 5, pp. 1017 –1028, Sep. 1994.

[79] Chatelain, F., Tourneret, J.-Y., Roche, M., and Alouini, M., "Estimating the polarization degree of polarimetric images in coherent illumination using maximum likelihood methods," *J. Opt. Soc. Am. A*, vol. 26, no. 6, pp. 1348–1359, 2009.

[80] Kay, S. M., *Fundamentals of Statistical Signal Processing: Estimation theory*, ser. Prentice Hall Signal Processing Series. Prentice-Hall, 1993.

[81] Roche, M., Fade, J., and Réfrégier, P., "Parametric estimation of the square degree of polarization from two intensity images degraded by fully developed speckle noise," *J. Opt. Soc. Am. A*, vol. 24, no. 9, pp. 2719–2727, 2007.

[82] Hoch, M., "New estimate puts gulf oil leak at 205 million gallons," *PBS NewsHour (MacNeil/Lehrer Productions)*, 2010, last Retrieved 2012-03-01.

[83] Crone, T. J. and Tolstoy, M., "Magnitude of the 2010 Gulf of Mexico oil leak," *Science*, vol. 330, no. 6004, p. 634, 2010.

[84] Krishen, K., "Detection of oil spills using a 13.3-GHz radar scatterometer," *J. Geophys. Res.*, vol. 78, no. 12, pp. 1952–1963, Apr. 1973.

[85] Singh, K. P., Gray, A. L., Hawkins, R. K., and O Neil, R. A., "The influence of surface oil on C-and Ku-band ocean backscatter," *IEEE Trans. Geosci. Remote Sens.*, vol. GE-24, no. 5, pp. 738–744, Sep. 1986.

[86] Alpers, W. and Hühnerfuss, H., "The damping of ocean waves by surface films: A new look at an old problem," *J. Geophys. Res.*, vol. 94, no. C5, pp. 6251–6265, 1989.

[87] Wismann, V., Gade, M., Alpers, W., and Hühnerfuss, H., "Radar signatures of mineral oil spills measured by an airborne multi-frequency multi-polarization microwave scatterometer," in *Proc. of OCEANS 93. Engineering in Harmony with Ocean.*, Victoria, BC , Canada, Oct. 1993, pp. II348–II353 vol.2.

[88] Fingas, M. F. and Brown, C. E., "Review of oil spill remote sensing," *Spill Science & Technology Bulletin*, vol. 4, no. 4, pp. 199–208, 1997.

[89] Valenzuela, G. R., "Theories for the interaction of electromagnetic and oceanic waves – a review," *Boundary-Layer Meteorology*, vol. 13, pp. 61–85, 1978, 10.1007/BF00913863.

[90] Brekke, C. and Solberg, A. H. S., "Review: Oil spill detection by satellite remote sensing," *Remote Sensing of Environment*, vol. 95, no. 1, pp. 1–13, 2005.

[91] Mercier, G. and Girard-Ardhuin, F., "Partially supervised oil-slick detection by SAR imagery using kernel expansion," *IEEE Trans. Geosci. Remote Sens.*, vol. 44, no. 10, pp. 2839–2846, Oct. 2006.

[92] Solberg, A. H. S., Brekke, C., and Husøy, P. O., "Oil spill detection in Radarsat and Envisat SAR images," *IEEE Trans. Geosci. Remote Sens.*, vol. 45, no. 3, pp. 746–755, Mar. 2007.

[93] Cloude, S. R. and Pottier, E., "A review of target decomposition theorems in radar polarimetry," *IEEE Trans. Geosci. Remote Sens.*, vol. 34, no. 2, pp. 498–518, Mar. 1996.

[94] Fortuny-Guasch, J., "Improved oil slick detection and classification with polarimetric SAR," in *Proc. of POLinSAR 03*, Frascati, Italy, 14–16 Jan. 2003, p. 27.1.

[95] Schuler, D. L., Lee, J.-S., and De Grandi, G., "Spiral eddy detection using surfactant slick patterns and polarimetric SAR image decomposition techniques," in *Proc. of IGARSS 04*, vol. 1, Sep. 2004, pp. 212–215.

[96] Migliaccio, M., Gambardella, A., and Tranfaglia, M., "SAR polarimetry to observe oil spills," *IEEE Trans. Geosci. Remote Sens.*, vol. 45, no. 2, pp. 506–511, Feb. 2007.

[97] Réfrégier, P. and Morio, J., "Shannon entropy of partially polarized and partially coherent light with Gaussian fluctuations," *J. Opt. Soc. Am. A*, vol. 23, no. 12, pp. 3036–3044, Dec. 2006.

[98] Nunziata, F., Gambardella, A., and Migliaccio, M., "On the use of dual-polarized SAR data for oil spill observation," in *Proc. of IGARSS 08*, vol. 2, Jul. 2008, pp. II–225–II–228.

[99] Migliaccio, M., Nunziata, F., and Gambardella, A., "On the co-polarized phase difference for oil spill observation," *Int. J. Remote Sens.*, vol. 30, pp. 1587–1602, Jan. 2009.

[100] Sarabandi, K., Oh, Y., and Ulaby, F. T., "Polarimetric radar measurements of bare soil surfaces at microwave frequencies," in *Proc. of IGARSS 91*, vol. 2, Jun. 1991, pp. 387–390.

[101] Ulaby, F. T., Sarabandi, K., and Nashashibi, A., "Statistical properties of the mueller matrix of distributed targets," *IEE Proceedings-F, Radar and Signal Processing*, vol. 139, no. 2, pp. 136–146, Apr. 1992.

[102] NOAA, *Open water oil identi cation job aid for aerial observation*, office of Response and Restoration, 2007.

[103] Leibovich, S., "The form and dynamics of Langmuir circulations," *Annual Review of Fluid Mechanics*, vol. 15, pp. 391–427, 1983.

[104] Pavlakis, P., Tarchi, D., and Sieber, A., "On the monitoring of illicit vessel discharges using spaceborne sar remote sensing– a reconnaissance study in the Mediterranean sea," *Annals of Telecommunications*, vol. 56, pp. 700–718, 2001, 10.1007/BF02995563.

[105] Alpers, W. and Espedal, H., *Chapter 11: Oils and surfactants, SAR Marine Users Manual*. Washington, D. C., USA: National Oceanic and Atmospheric Administration, Center for Satellite Application and Research, NOAA/NESDIS, 2004, pp. 263–275, ISBN 0-16-073214-X, 263-275.

[106] Langmuir, I., "Surface motion of water induced by wind," *Science*, vol. 87, no. 2250, pp. 119–123, 1938.

[107] Foo, B. Y., Chaudhuri, S. K., and Boerner, W.-M., "Polarization correction and extension of the Kennaugh-Cosgriff target-ramp response equation to the bistatic case and applications to electromagnetic inverse scattering," *IEEE Trans. Antennas Propag.*, vol. 38, no. 7, pp. 964–972, Jul. 1990.

[108] Boerner, W.-M., Foo, B. Y., and Eom, H. J., "Interpretation of the polarimetric co-polarization phase term in radar images obtained with the JPL airborne L-band SAR system," *IEEE Trans. Geosci. Remote Sens.*, vol. GE-25, no. 1, pp. 77–82, Jan. 1987.

[109] Ulaby, F. T., Held, D., Donson, M. C., McDonald, K. C., and Senior, T. B. A., "Relating polaization phase difference of SAR signals to scene properties," *IEEE Trans. Geosci. Remote Sens.*, vol. GE-25, no. 1, pp. 83–92, Jan. 1987.

[110] Lee, J.-S., Grunes, M. R., and Pottier, E., "Quantitative comparison of classification capability: fully polarimetric versus dual and single-polarization SAR," *IEEE Trans. Geosci. Remote Sens.*, vol. 39, no. 11, pp. 2343–2351, Nov. 2001.

[111] Shannon, C. E., "A mathematical theory of communication," *Bell Syst. Tech. J.*, vol. 27, pp. 379–423, 623–656, Jul., Oct. 1948.

[112] Réfrégier, P., Goudail, F., Chavel, P., and Friberg, A., "Entropy of partially polarized light and application to statistical processing techniques," *Journal of the Optical Society of America A*, vol. 21, no. 11, pp. 2124–2134, Nov. 2004.

[113] Barakat, R., "n-fold polarization measures and associated thermodynamic entropy of N partially coherent pencils of radiation," *Optica Acta: International Journal of Optics*, vol. 30, no. 8, pp. 1171–1182, 1983.

[114] Hussey, W. J., "The economic benefits of operational environmental satellites," *Environmental Satellite , Data, and Information*

Service: National Oceanic and Atmospheric Administration; US Department of Commerce, Washington, DC, USA, Mar. 1983.

[115] Vachon, P. W., Campbell, J. W. M., Bjerkelund, C., Dobson, F. W., and Rey, M. T., "Ship detection by the RADARSAT SAR: validation of detection model predictions," *Canadian Journal of Remote Sensing*, vol. 23, no. 1, pp. 48–59, 1997.

[116] Yeremy, M., Campbell, J. W. M., Mattar, K., and Potter, T., "Ocean surveillance with polarimetric SAR," *Canadian Journal of Remote Sensing*, vol. 27, no. 4, pp. 328–344, 2001.

[117] Hawkins, R. K., Murnaghan, K. P., Tennant, T., Yeremy, M., and Rey, M., "Ship detection using airborne polarimetric SAR," in *Proceedings of CEOS SAR Workshop*, Tokyo, Japan, Apr. 2001.

[118] Ringrose, R. and Harris, N., "Ship detection using polarimetric SAR data," in *SAR workshop: CEOS Committee on Earth Observation Satellites*, ser. ESA Special Publication, R. A. Harris & L. Ouwehand, Ed., vol. 450, Mar. 2000, p. 687.

[119] Sciotti, M., Pastina, D., and Lombardo, P., "Exploiting the polarimetric information for the detection of ship targets in non-homogeneous SAR images," in *Proc. of IGARSS 02*, vol. 3, Jun. 2002, pp. 1911–1913.

[120] Touzi, R., Charbonneau, F. J., Hawkins, R. K., and Vachon, P. W., "Ship detection and characterization using polarimetric SAR," *Canadian Journal of Remote Sensing*, vol. 30, no. 3, pp. 552–559, 2004.

[121] Liu, C., Vachon, P. W., and Geling, G. W., "Improved ship detection using polarimetric SAR data," in *Proc. of IGARSS 04*, vol. 3, Anchorage, Alaska, sept. 2004, pp. 1800 –1803 vol.3.

[122] Angelliaume, S., Durand, P., and Souyris, J. C., "Ship detection using X-band dual-pol SAR data," in *Proc. of IGARSS 11*, Jul. 2011, pp. 3827–3830.

[123] Huang, D., Swanson, E. A., Lin, C. P., Schuman, J. S., Stinson, W. G., Chang, W., Hee, M. R., Flotte, T., Gregory, K., Puliafito, C. A., and Fujimoto, J. G., "Optical coherence tomography," *Science*, vol. 254, pp. 1178–1181, 1991.

[124] Schmitt, J. M., "Optical coherence tomography (OCT): a review," *IEEE Journal of Selected Topics in Quantum Electronics*, vol. 5, no. 4, pp. 1205–1215, Jul. 1999.

[125] [Online] URL: http://obel.ee.uwa.edu.au (last accessed September 2012).

[126] de Boer, J. F., Milner, T. E., van Gemert, M. J. C., and Nelson, J. S., "Two-dimensional birefringence imaging in biological tissue by polarization-sensitive optical coherence tomography," *Opt. Lett.*, vol. 22, no. 12, pp. 934–936, 1997.

[127] de Boer, J. F., Srinivas, S., Malekafzali, A., Chen, Z.-P., and Nelson, J., "Imaging thermally damaged tissueby polarization sensitive optical coherence tomography," *Opt. Express*, vol. 3, no. 6, pp. 212–218, Sep. 1998.

[128] Ducros, M. G., de Boer, J. F., Huai-En, H., Chao, L. C., Zhongping, C., Nelson, J. S., Milner, T. E., and Rylander, I. H. G., "Polarization sensitive optical coherence tomography of the rabbit eye," *IEEE Journal of Selected Topics in Quantum Electronics*, vol. 5, no. 4, pp. 1159–1167, Jul. 1999.

[129] Srinivas, S. M., de Boer, J. F., Park, H., Keikhanzadeh, K., Huang, H. L., Zhang, J., Jung, W. Q., Chen, Z., and Nelson, J. S., "Determination of burn depth by polarization-sensitive optical coherence tomography," *Journal of Biomedical Optics*, vol. 9, no. 1, pp. 207–212, 2004.

[130] Lee, S.-W., Yoo, J.-Y., Kang, J.-H., Kang, M.-S., Jung, S.-H., Ch., Y., Cha, D.-S., Han, K.-H., and Kim, B.-M., "Optical diagnosis of cervical intraepithelial neoplasm (CIN) using polarization-sensitive optical coherence tomography," *Opt. Express*, vol. 16, no. 4, pp. 2709–2719, Feb. 2008.

[131] Oh, J.-T., Lee, S.-W., Kim, Y.-S., Suhr, K.-B., and Kim, B.-M., "Quantification of the wound healing using polarization-sensitive optical coherence tomography," *Journal of Biomedical Optics*, vol. 11, no. 4, p. 041124, 2006.

[132] de Boer, J. F. and Milner, T. E., "Review of polarization sensitive optical coherence tomography and stokes vector determination," *Journal of Biomedical Optics*, vol. 7, no. 3, pp. 359–371, 2002.

[133] Götzinger, E., Pircher, M., Baumann, B., Ahlers, C., Geitzenauer, W., Schmidt-Erfurth, U., and Hitzenberger, C. K., "Three-dimensional polarization sensitive OCT imaging and interactive display of the human retina," *Opt. Express*, vol. 17, no. 5, pp. 4151–4165, Mar. 2009.

[134] Clemente-Colón, P. and Yan, X. H., "Low-backscatter ocean features in synthetic aperture radar imagery," *Johns Hopkins APL Technical Digest*, vol. 21, no. 1, pp. 116–121, 2000.

[135] Hu, C., Li, X., Pichel, W. G., and Muller-Karger, F. E., "Detection of natural oil slicks in the NW Gulf of Mexico using MODIS imagery," *Geophys. Res. Lett.*, vol. 36, p. L01604, 2009.

[136] Huehnerfuss, H., Alpers, W., Garrett, W. D., Lange, P. A., and Stolte, S., "Attenuation of capillary and gravity waves at sea by monomolecular organic surface films," *J. Geophys. Res.*, vol. 88, pp. 9809–9816, 1983.

[137] Holt, B., *SAR imaging of the ocean surface, SAR Marine Users Manual*. Washington, D. C., USA: National Oceanic and Atmospheric Administration, Center for Satellite Application and Research, NOAA/NESDIS, 2004, pp. 25–80, ISBN 0-16-073214-X, 263-275.

[138] Thompson, D. R., *Microwave scattering from the sea, SAR Marine Users Manual*. Washington, D. C., USA: National Oceanic and Atmospheric Administration, Center for Satellite Application and Research, NOAA/NESDIS, 2004, pp. 117–138, ISBN 0-16-073214-X, 263-275.

[139] Garcia-Pineda, O., Zimmer, B., Howard, M., Pichel, W., Li, X., and MacDonald, I. R., "Using SAR images to delineate ocean oil slicks with a texture-classifying neural network algorithm (TCNNA)," *Canadian Journal of Remote Sensing*, vol. 35, no. 5, pp. 411–421, 2009.

[140] ALOS PALSAR, *Cyclic Report*, Jan. 2008, cycle 13, PALSAR-CR-13-070723-070907.

[141] DLR, *TerraSAR-X Ground Segment Basic Product Speci cation Document*, 2008, tX-GS-DD-3302.